# Supporting Information

## Effect of building block connectivity and ion solvation on electrochemical stability and ionic conductivity in novel fluoroether electrolytes

Peiyuan Ma,[1] Priyadarshini Mirmira,[1] and Chibueze V. Amanchukwu[1,2*]

[1]Pritzker School of Molecular Engineering, University of Chicago, IL 60637 USA

[2]Chemical Sciences and Engineering Division, Argonne National Laboratory, Lemont IL 60439

*Corresponding author

Email: chibueze@uchicago.edu

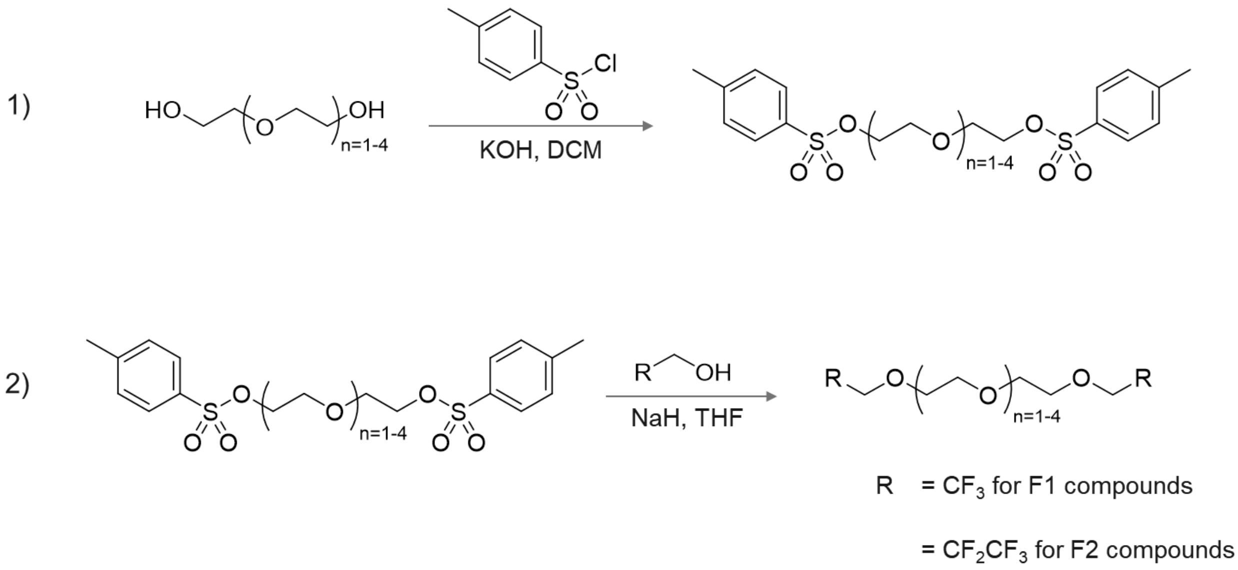

**Figure S1**. Synthetic route of F1 and F2 compounds. 1) Glycols were tosylated by tosyl chloride with the presence of excess amount of potassium hydroxide. 2) Fluorinated alcohols were deprotonated and then reacted with tosylated glycols to yield F1 and F2 compounds. Detailed synthetic procedure can be found in the Experimental Section.

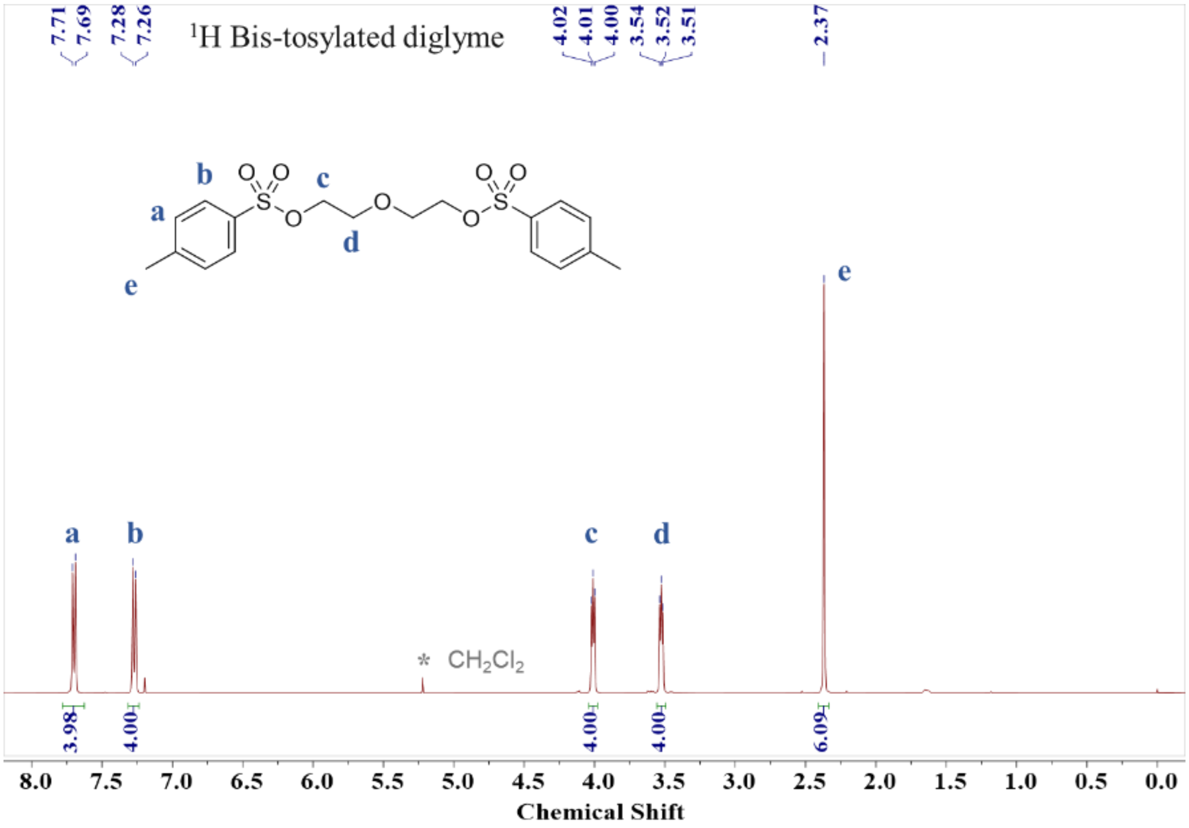
$^1$H Bis-tosylated diglyme
7.71
7.69
7.28
7.26
4.02
4.01
4.00
3.54
3.52
3.51
2.37
a
b
c
d
e
* $CH_2Cl_2$
3.98
4.00
4.00
4.00
6.09
8.0 7.5 7.0 6.5 6.0 5.5 5.0 4.5 4.0 3.5 3.0 2.5 2.0 1.5 1.0 0.5 0.0
Chemical Shift

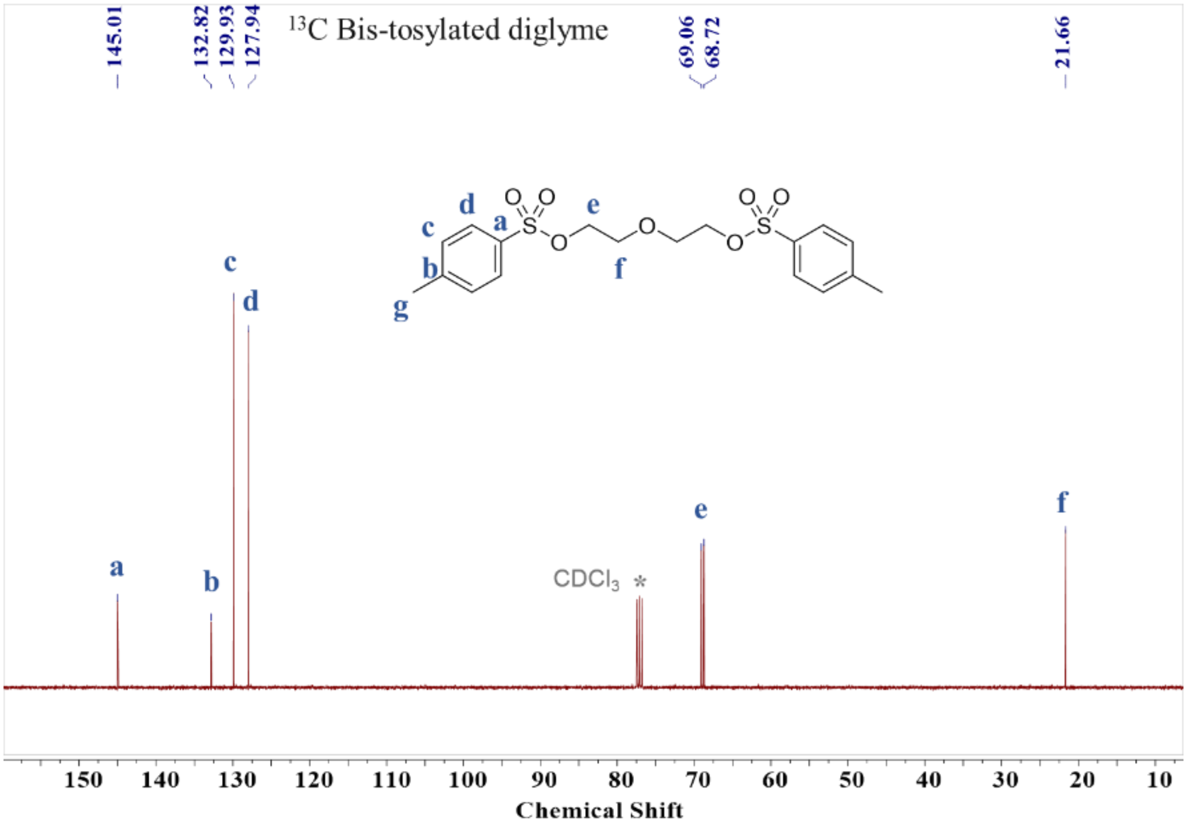
$^{13}$C Bis-tosylated diglyme
145.01
132.82
129.93
127.94
69.06
68.72
21.66
a
b
c
d
e
f
g
$CDCl_3$ *
150 140 130 120 110 100 90 80 70 60 50 40 30 20 10
Chemical Shift

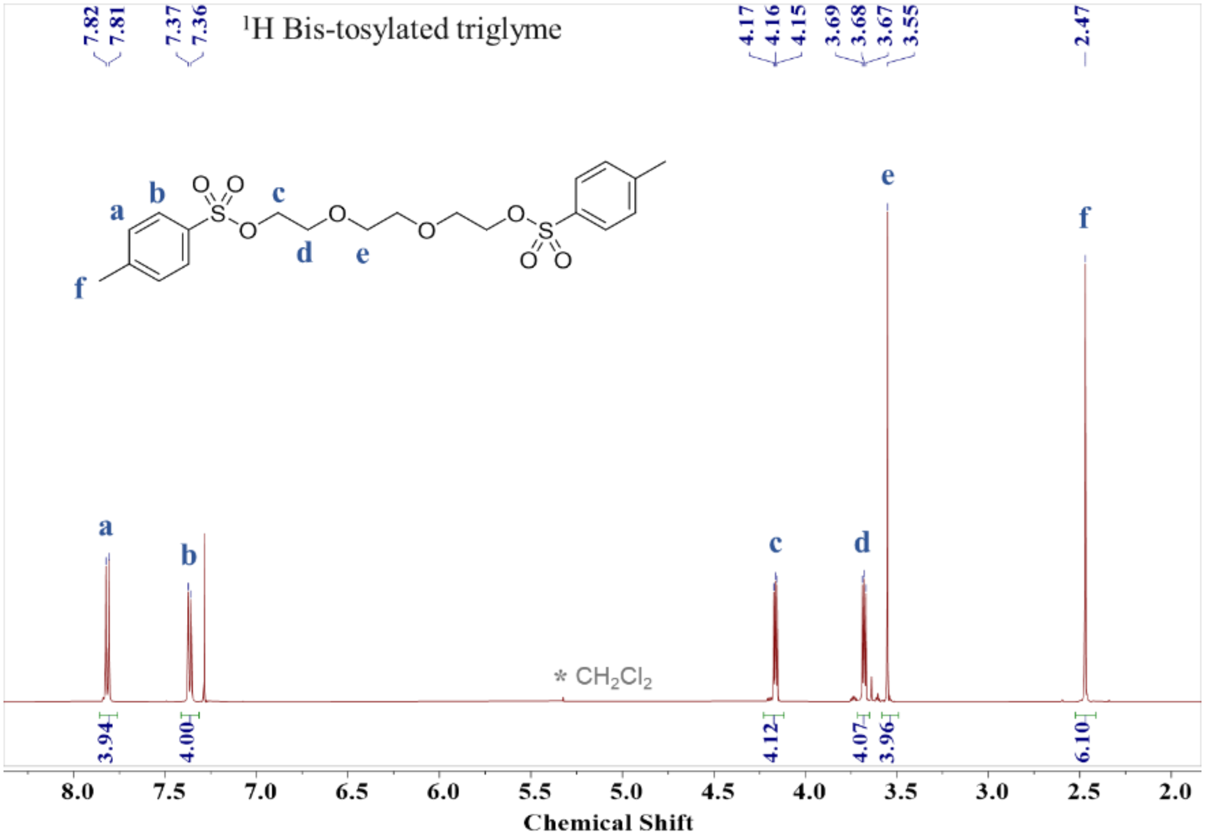

$^{1}$H Bis-tosylated triglyme
7.82
7.81
7.37
7.36
4.17
4.16
4.15
3.69
3.68
3.67
3.55
2.47
a
b
c
d
e
f
* $CH_2Cl_2$
3.94
4.00
4.12
4.07
3.96
6.10
8.0
7.5
7.0
6.5
6.0
5.5
5.0
4.5
4.0
3.5
3.0
2.5
2.0
Chemical Shift

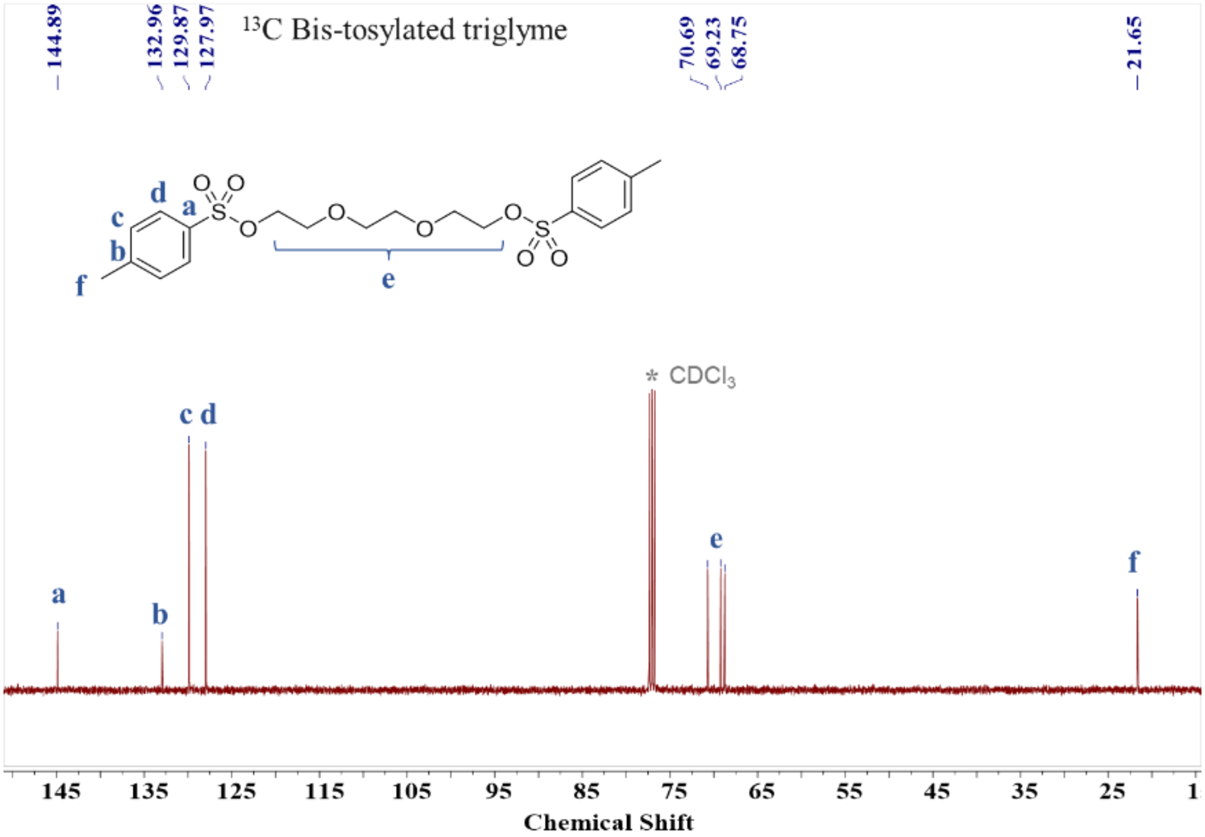

$^{13}$C Bis-tosylated triglyme
144.89
132.96
129.87
127.97
70.69
69.23
68.75
21.65
a
b
c
d
e
f
* $CDCl_3$
145
135
125
115
105
95
85
75
65
55
45
35
25
1
Chemical Shift

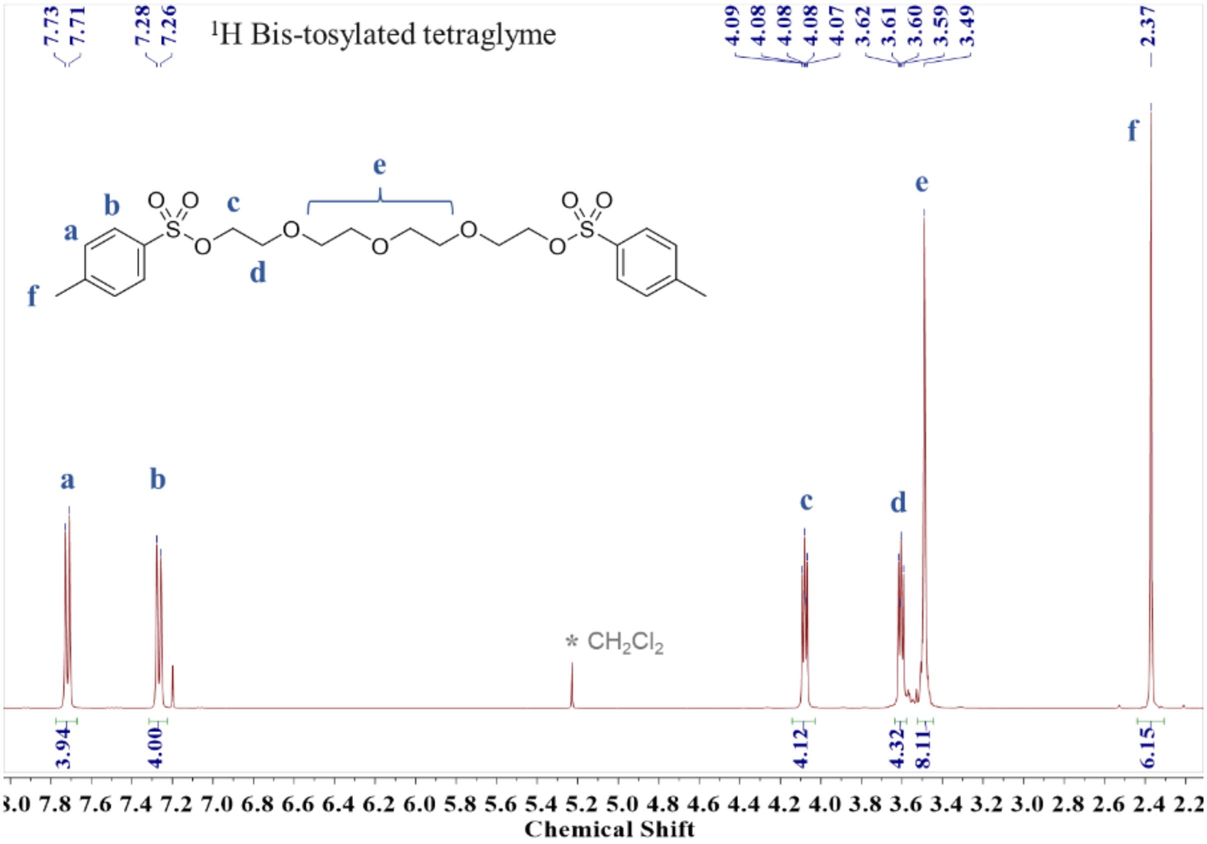

1H Bis-tosylated tetraglyme
7.73
7.71
7.28
7.26
4.09
4.08
4.08
4.08
4.07
3.62
3.61
3.60
3.59
3.49
2.37
a
b
c
d
e
f
O
S
* CH2Cl2
3.94
4.00
4.12
4.32
8.11
6.15
.0 7.8 7.6 7.4 7.2 7.0 6.8 6.6 6.4 6.2 6.0 5.8 5.6 5.4 5.2 5.0 4.8 4.6 4.4 4.2 4.0 3.8 3.6 3.4 3.2 3.0 2.8 2.6 2.4 2.2
Chemical Shift

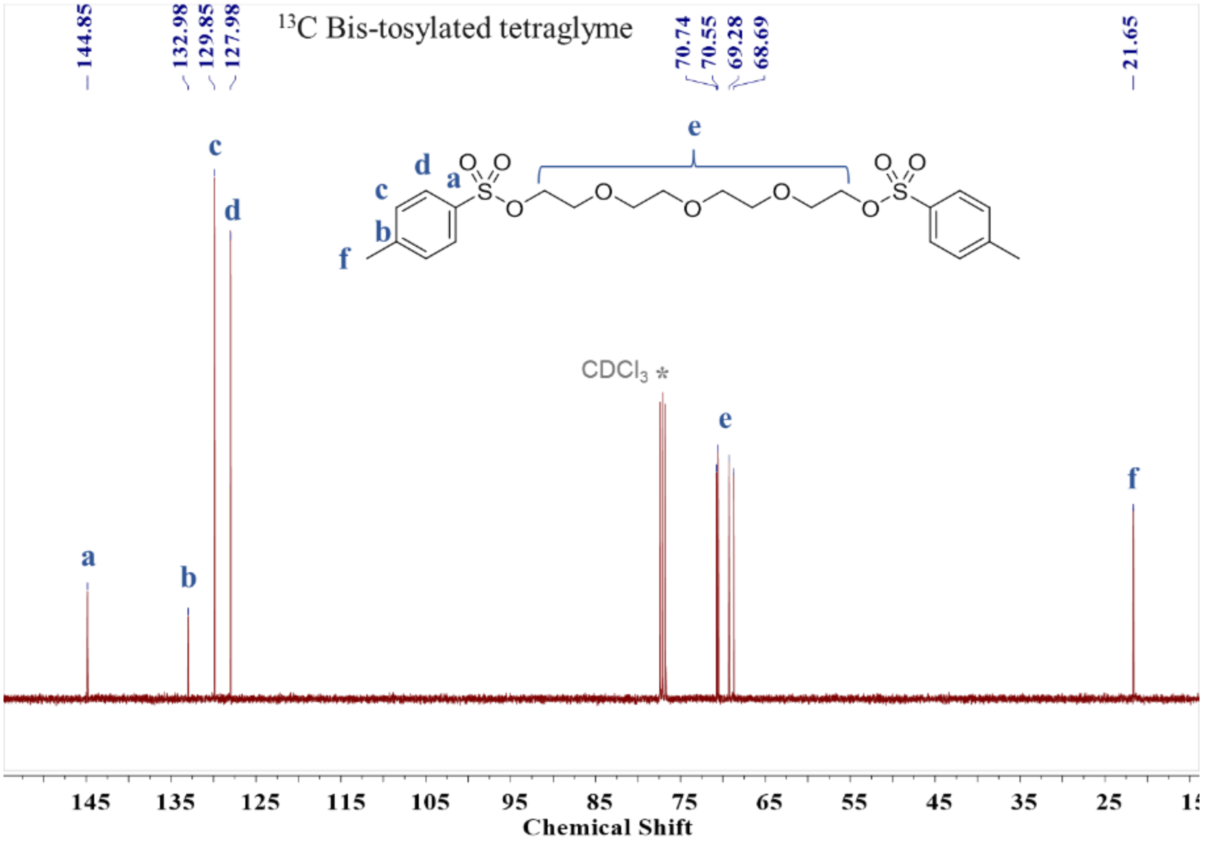

13C Bis-tosylated tetraglyme
144.85
132.98
129.85
127.98
70.74
70.55
69.28
68.69
21.65
a
b
c
d
e
f
O
S
CDCl3 *
145
135
125
115
105
95
85
75
65
55
45
35
25
1
Chemical Shift

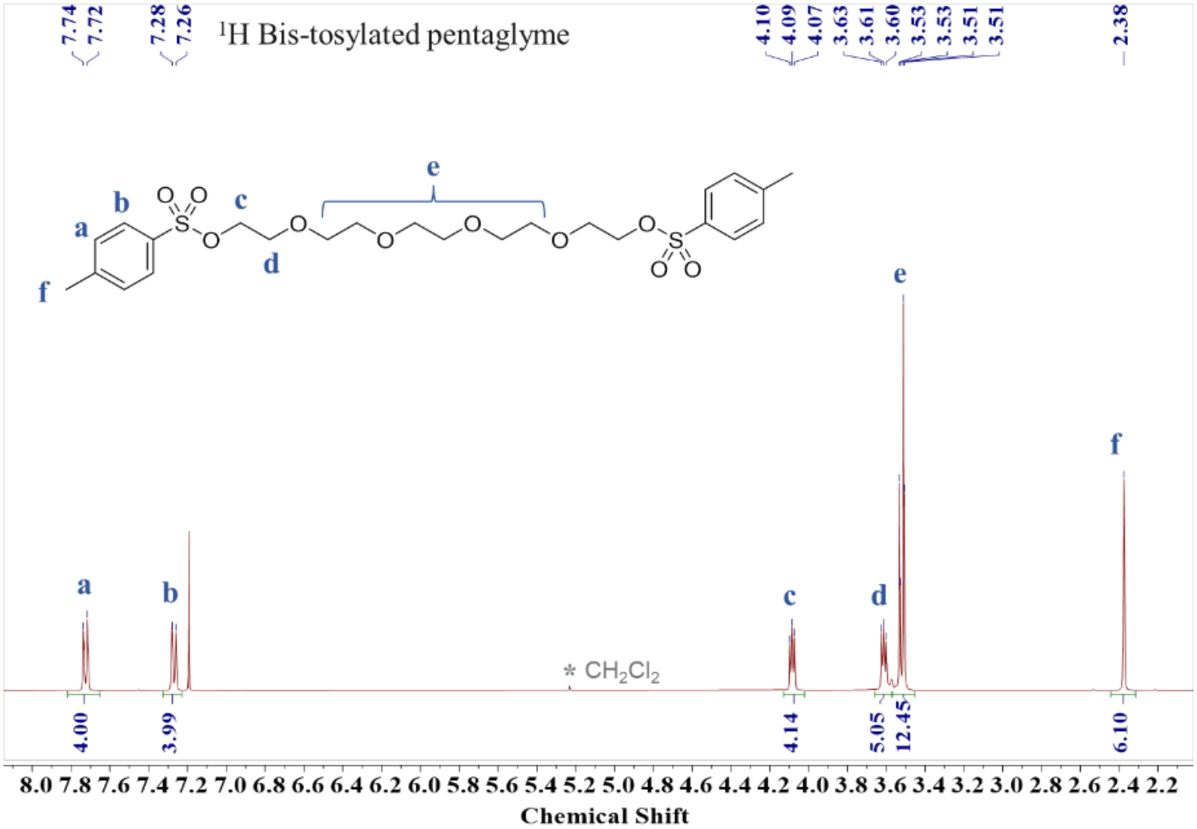

$^1$H Bis-tosylated pentaglyme
7.74
7.72
7.28
7.26
4.10
4.09
4.07
3.63
3.61
3.60
3.53
3.53
3.51
3.51
2.38
a
b
c
d
e
f
* $CH_2Cl_2$
4.00
3.99
4.14
5.05
12.45
6.10
8.0 7.8 7.6 7.4 7.2 7.0 6.8 6.6 6.4 6.2 6.0 5.8 5.6 5.4 5.2 5.0 4.8 4.6 4.4 4.2 4.0 3.8 3.6 3.4 3.2 3.0 2.8 2.6 2.4 2.2
Chemical Shift

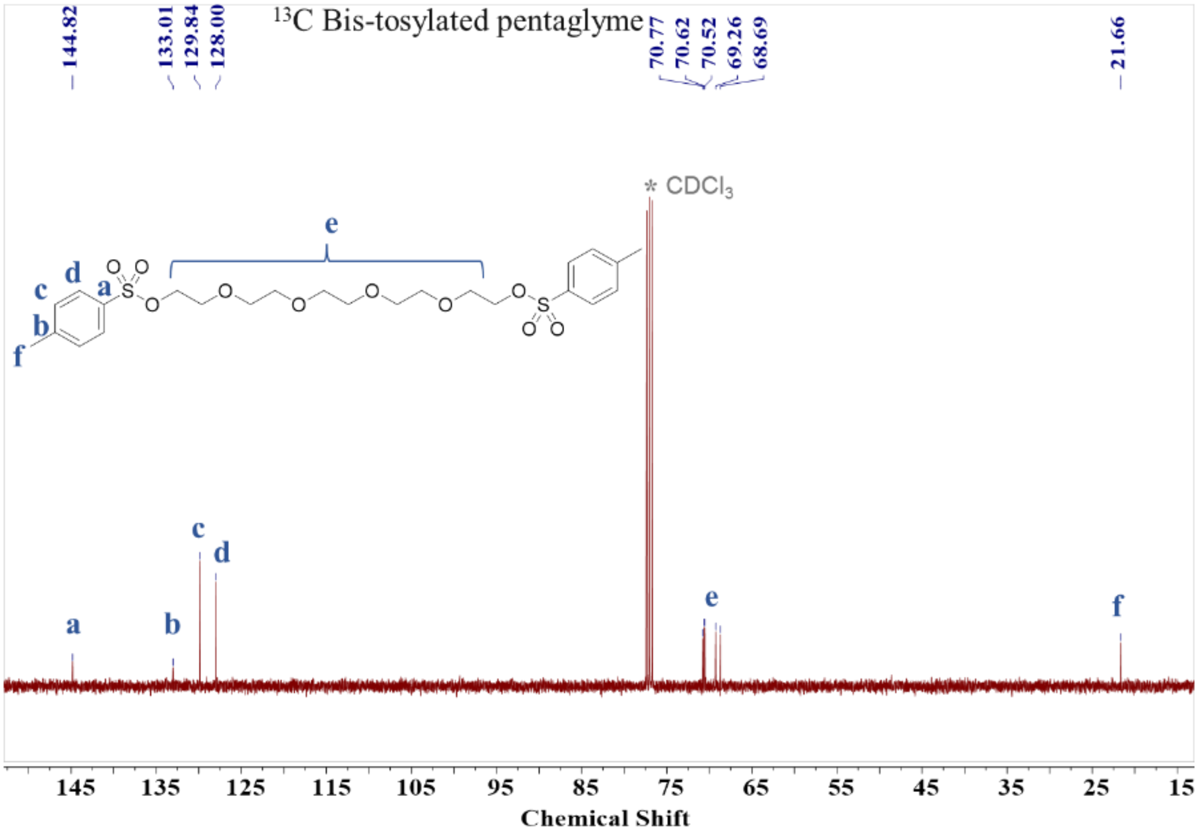

$^{13}$C Bis-tosylated pentaglyme
144.82
133.01
129.84
128.00
70.77
70.62
70.52
69.26
68.69
21.66
* $CDCl_3$
a
b
c
d
e
f
145
135
125
115
105
95
85
75
65
55
45
35
25
15
Chemical Shift

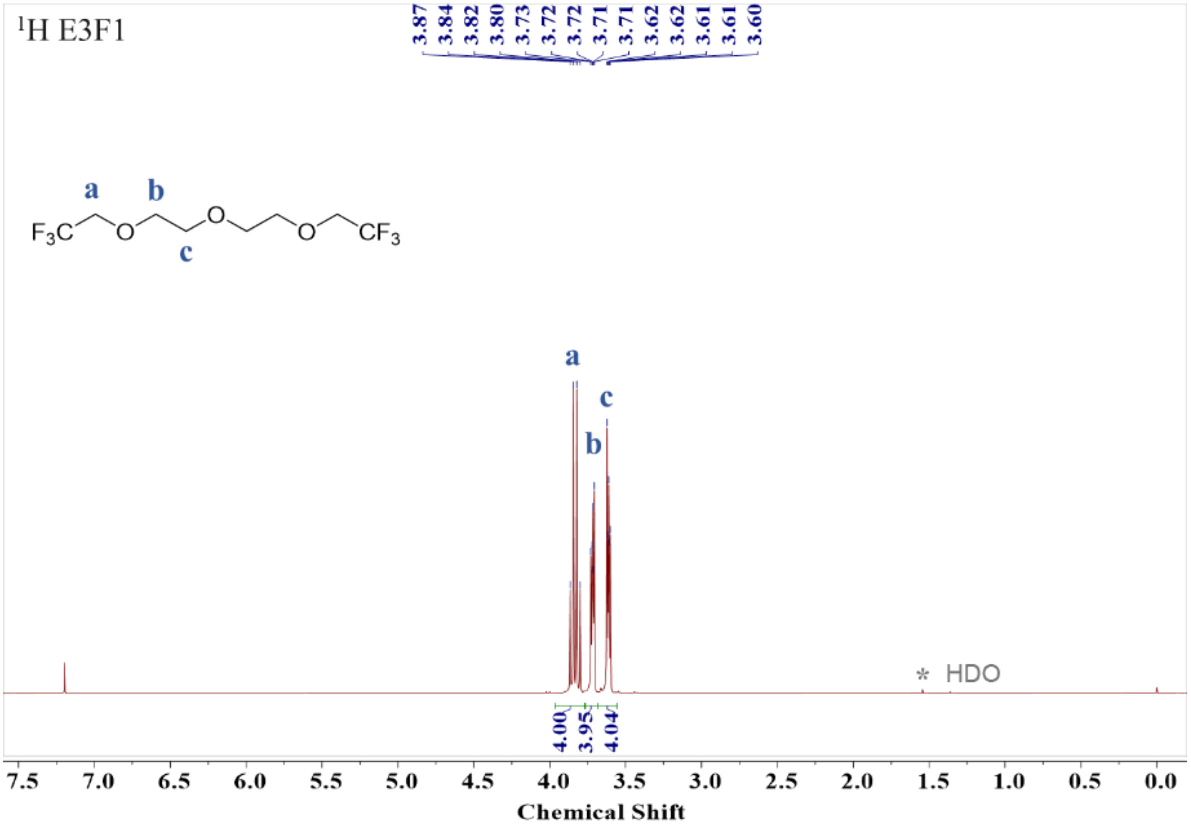

$^1$H E3F1
3.87
3.84
3.82
3.80
3.73
3.72
3.72
3.71
3.71
3.62
3.62
3.61
3.61
3.60
a
b
c
$F_3C$
O
O
O
$CF_3$
a
b
c
* HDO
4.00
3.95
4.04
7.5
7.0
6.5
6.0
5.5
5.0
4.5
4.0
3.5
3.0
2.5
2.0
1.5
1.0
0.5
0.0
Chemical Shift

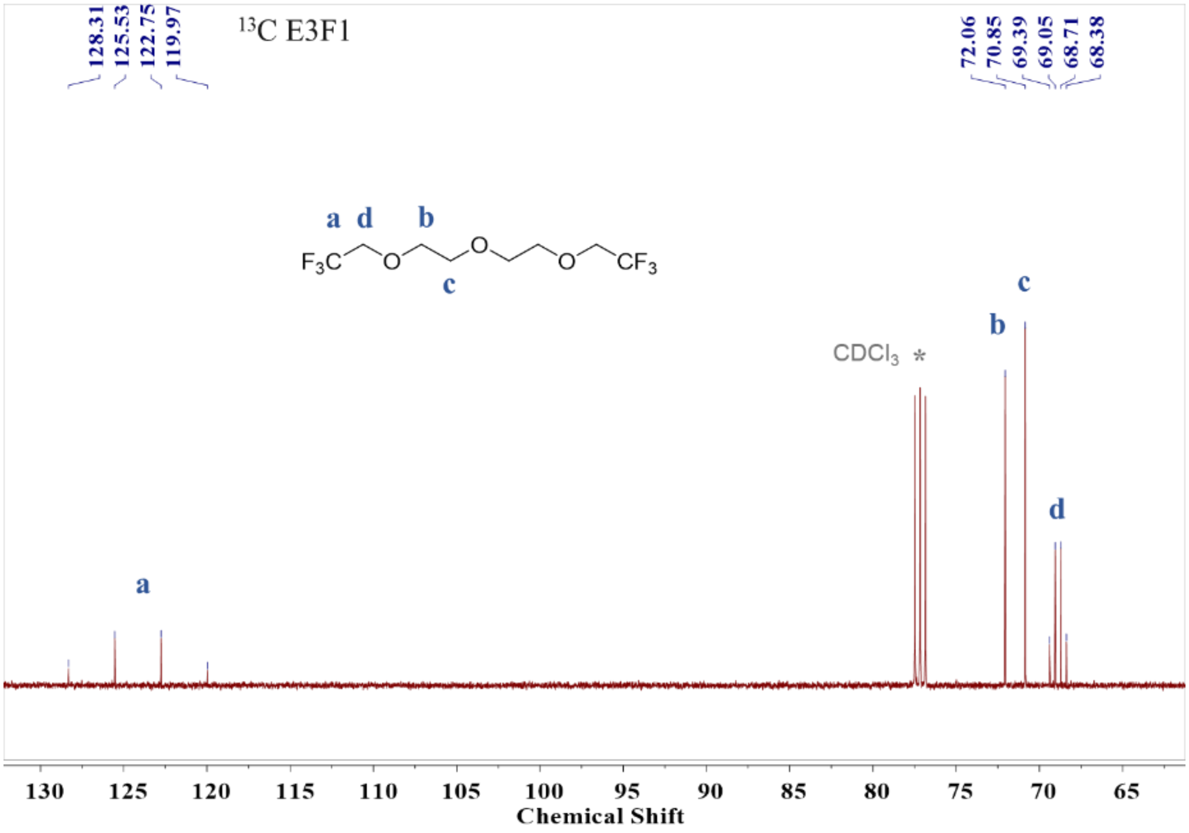

128.31
125.53
122.75
119.97
$^{13}$C E3F1
72.06
70.85
69.39
69.05
68.71
68.38
a
d
b
$F_3C$
O
O
O
$CF_3$
c
CDCl$_3$ *
b
c
d
a
130
125
120
115
110
105
100
95
90
85
80
75
70
65
Chemical Shift

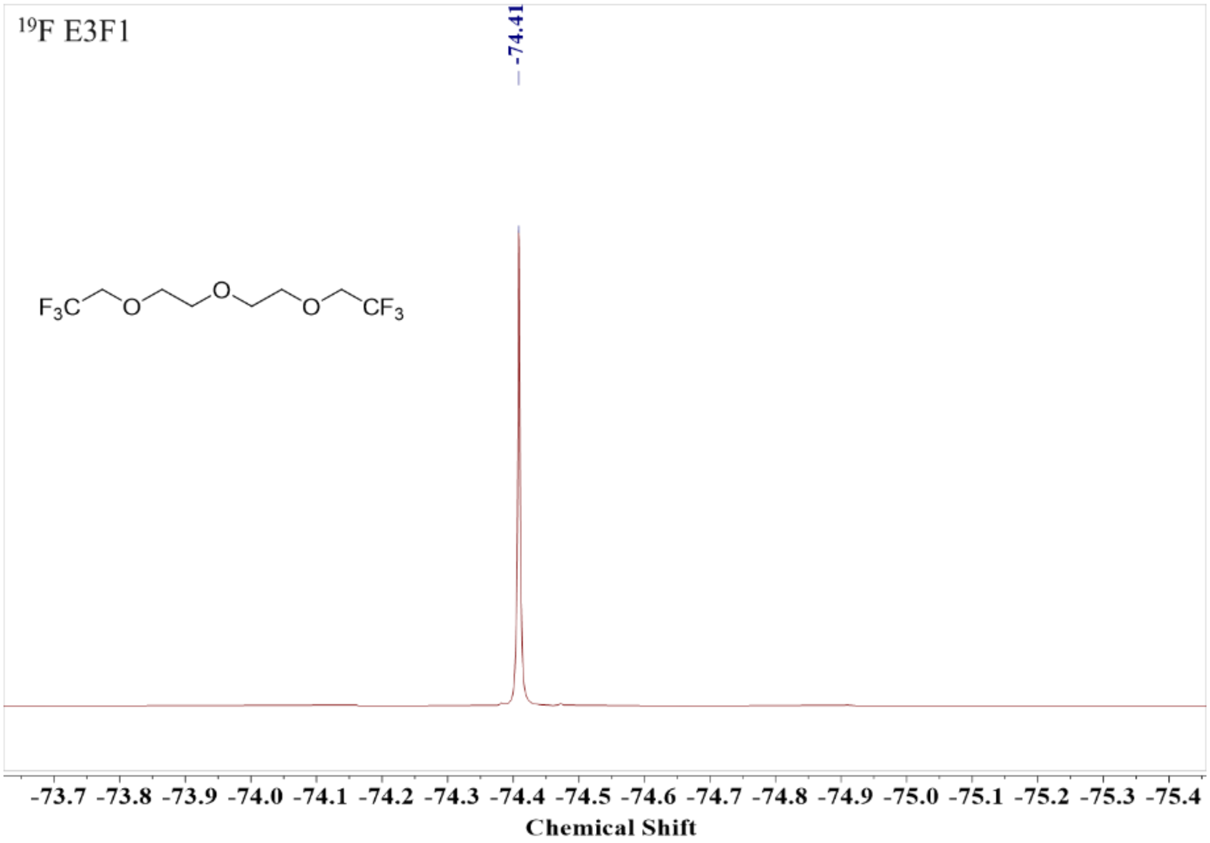

19F E3F1
-74.41
F3C O O O CF3
-73.7 -73.8 -73.9 -74.0 -74.1 -74.2 -74.3 -74.4 -74.5 -74.6 -74.7 -74.8 -74.9 -75.0 -75.1 -75.2 -75.3 -75.4
Chemical Shift

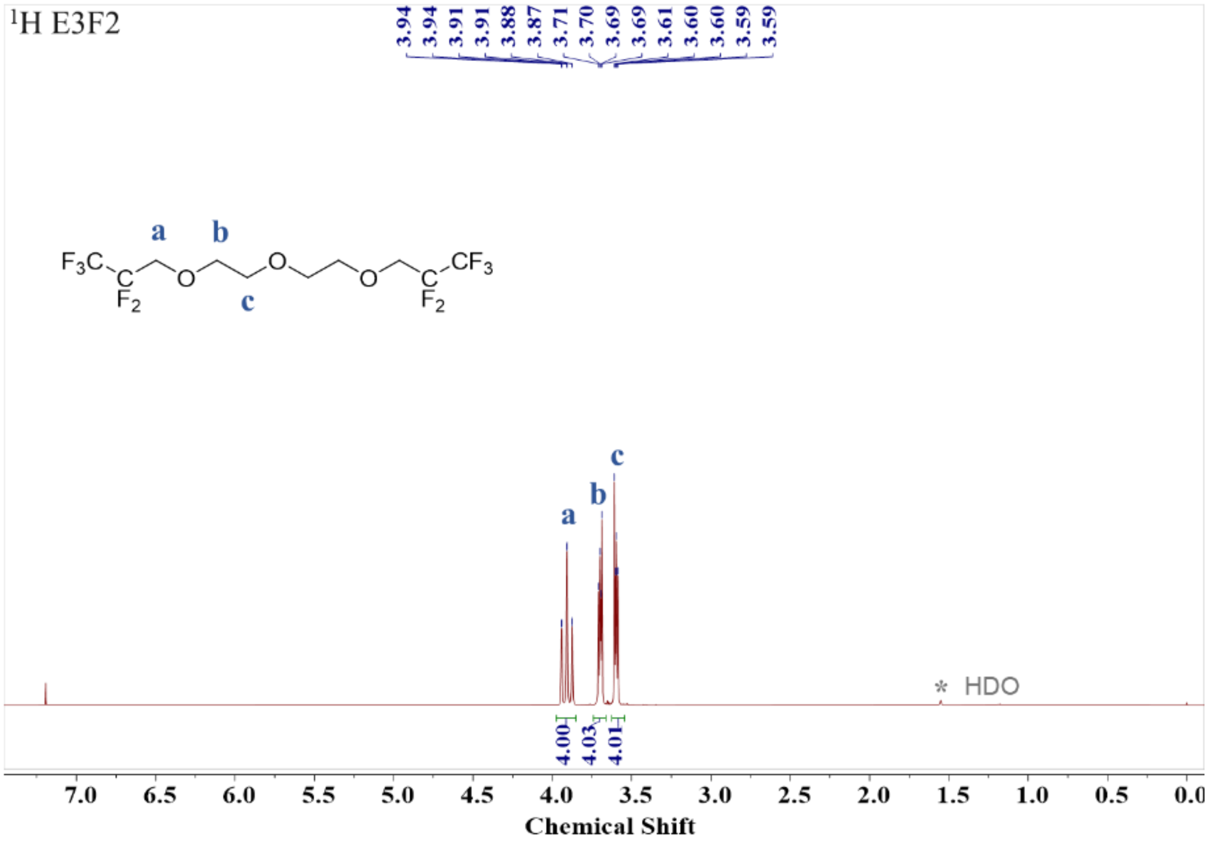

1H E3F2
3.94 3.94 3.91 3.91 3.88 3.87 3.71 3.70 3.69 3.69 3.61 3.60 3.60 3.59 3.59
a
b
c
F3C C F2 O O O C F2 CF3
a
b
c
* HDO
4.00
4.03
4.01
7.0 6.5 6.0 5.5 5.0 4.5 4.0 3.5 3.0 2.5 2.0 1.5 1.0 0.5 0.0
Chemical Shift

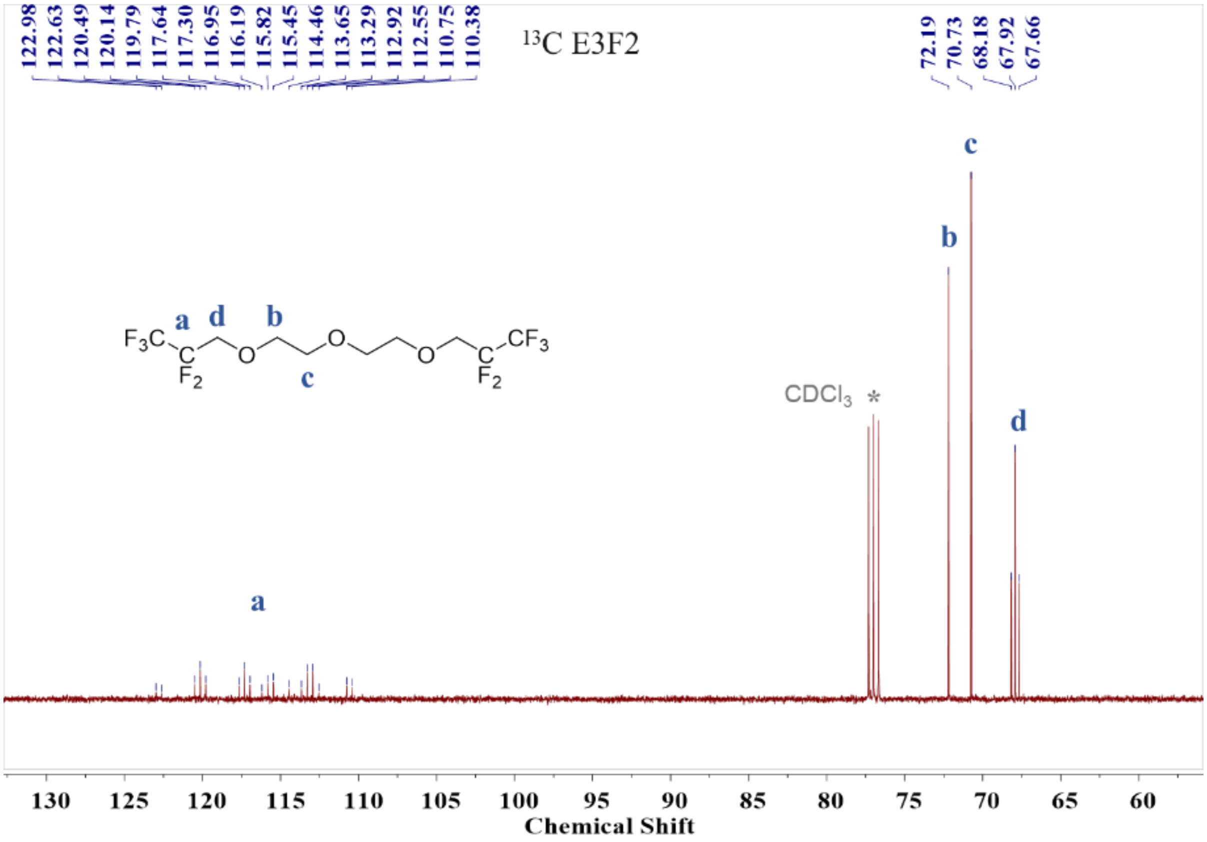
13C E3F2
122.98
122.63
120.49
120.14
119.79
117.64
117.30
116.95
116.19
115.82
115.45
114.46
113.65
113.29
112.92
112.55
110.75
110.38
72.19
70.73
68.18
67.92
67.66
c
b
a
d
b
$F_3C$
C
$F_2$
O
O
O
$CF_3$
C
$F_2$
c
$CDCl_3$
*
d
a
130
125
120
115
110
105
100
95
90
85
80
75
70
65
60
Chemical Shift

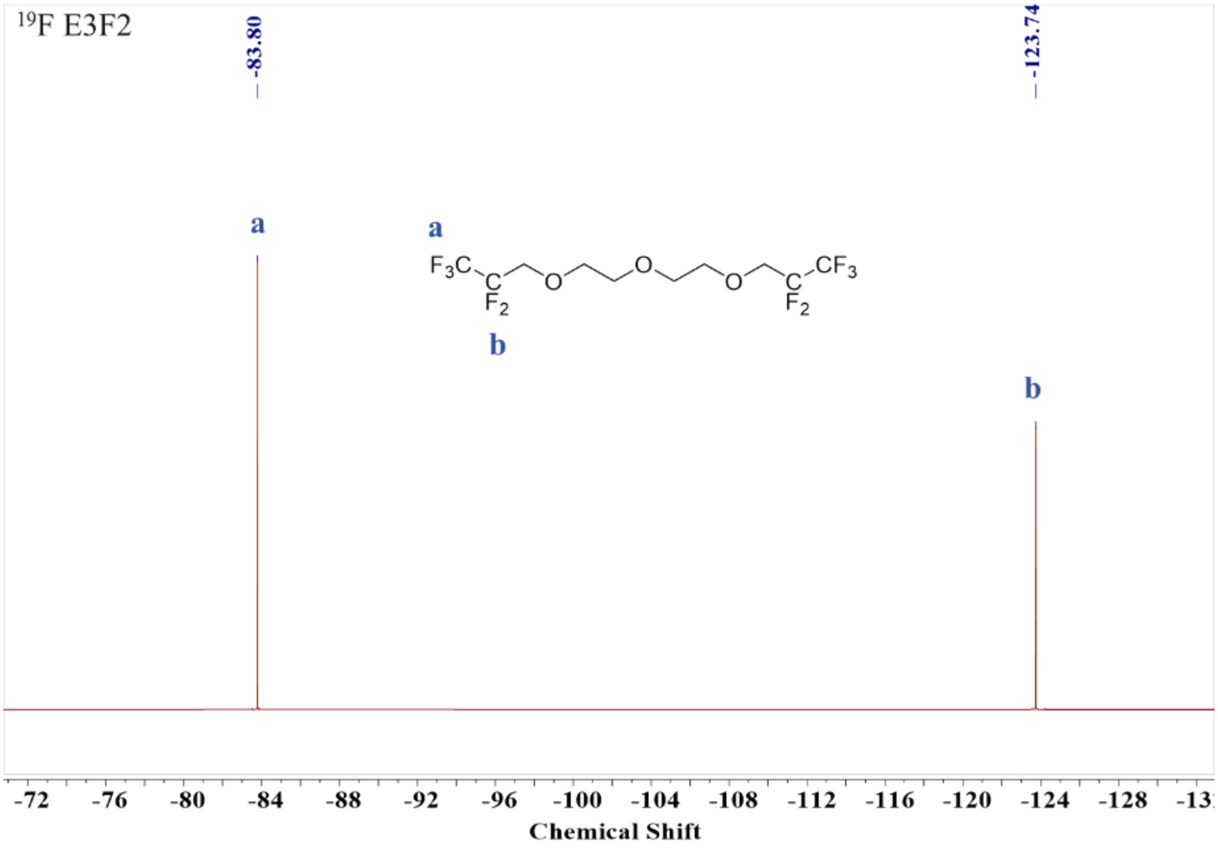
19F E3F2
-83.80
-123.74
a
a
$F_3C$
C
$F_2$
O
O
O
C
$CF_3$
$F_2$
b
b
-72
-76
-80
-84
-88
-92
-96
-100
-104
-108
-112
-116
-120
-124
-128
-13
Chemical Shift

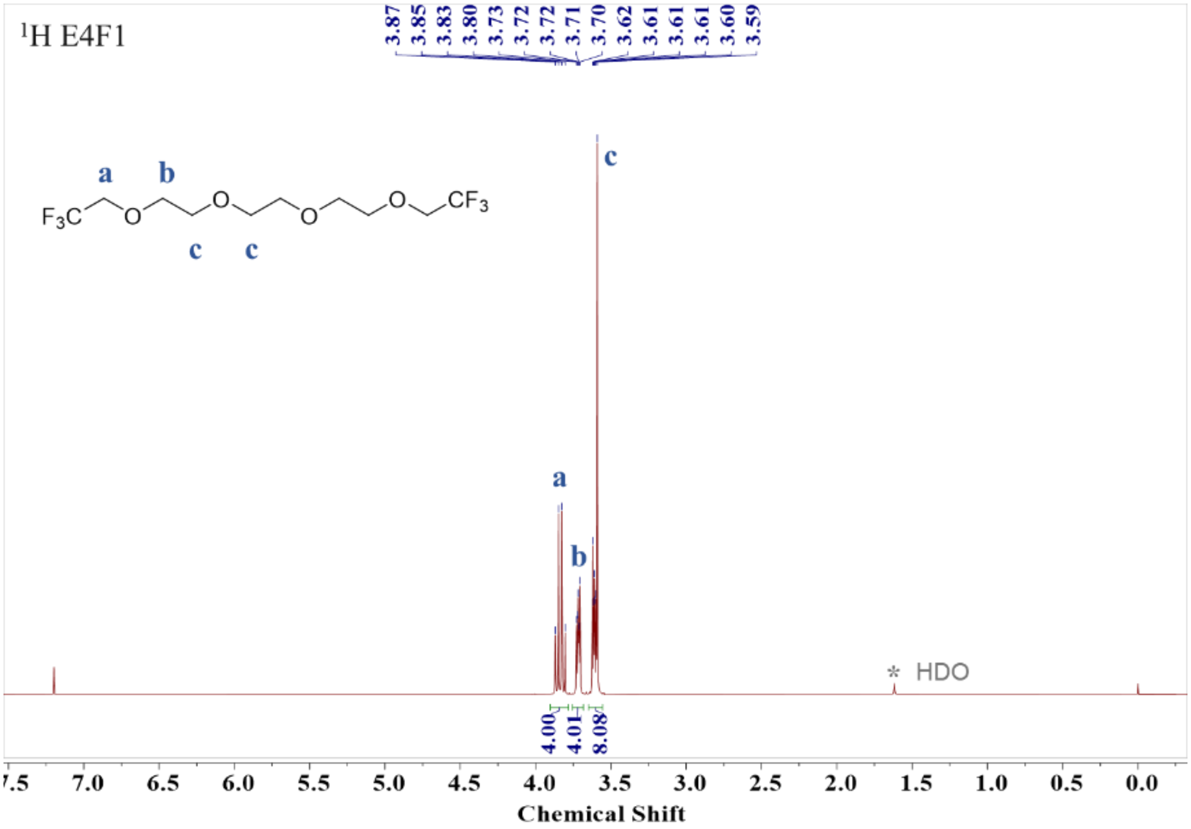
1H E4F1
3.87 3.85 3.83 3.80 3.73 3.72 3.72 3.71 3.70 3.62 3.61 3.61 3.61 3.60 3.59
a
b
c
c
$F_3C$
O
O
O
O
$CF_3$
a
b
c
* HDO
4.00
4.01
8.08
7.5 7.0 6.5 6.0 5.5 5.0 4.5 4.0 3.5 3.0 2.5 2.0 1.5 1.0 0.5 0.0
Chemical Shift

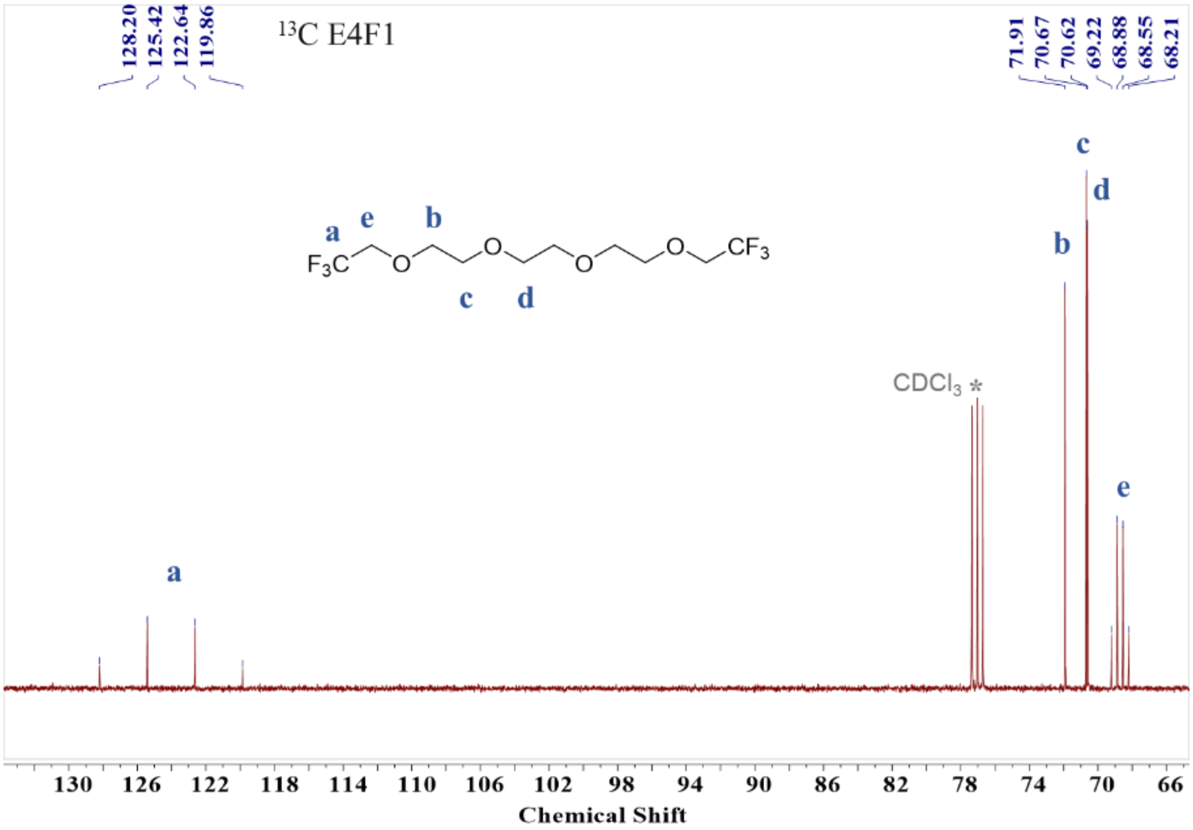
128.20 125.42 122.64 119.86
13C E4F1
71.91 70.67 70.62 69.22 68.88 68.55 68.21
a
e
b
$F_3C$
O
O
O
O
$CF_3$
c
d
c
d
b
$CDCl_3$ *
e
a
130 126 122 118 114 110 106 102 98 94 90 86 82 78 74 70 66
Chemical Shift

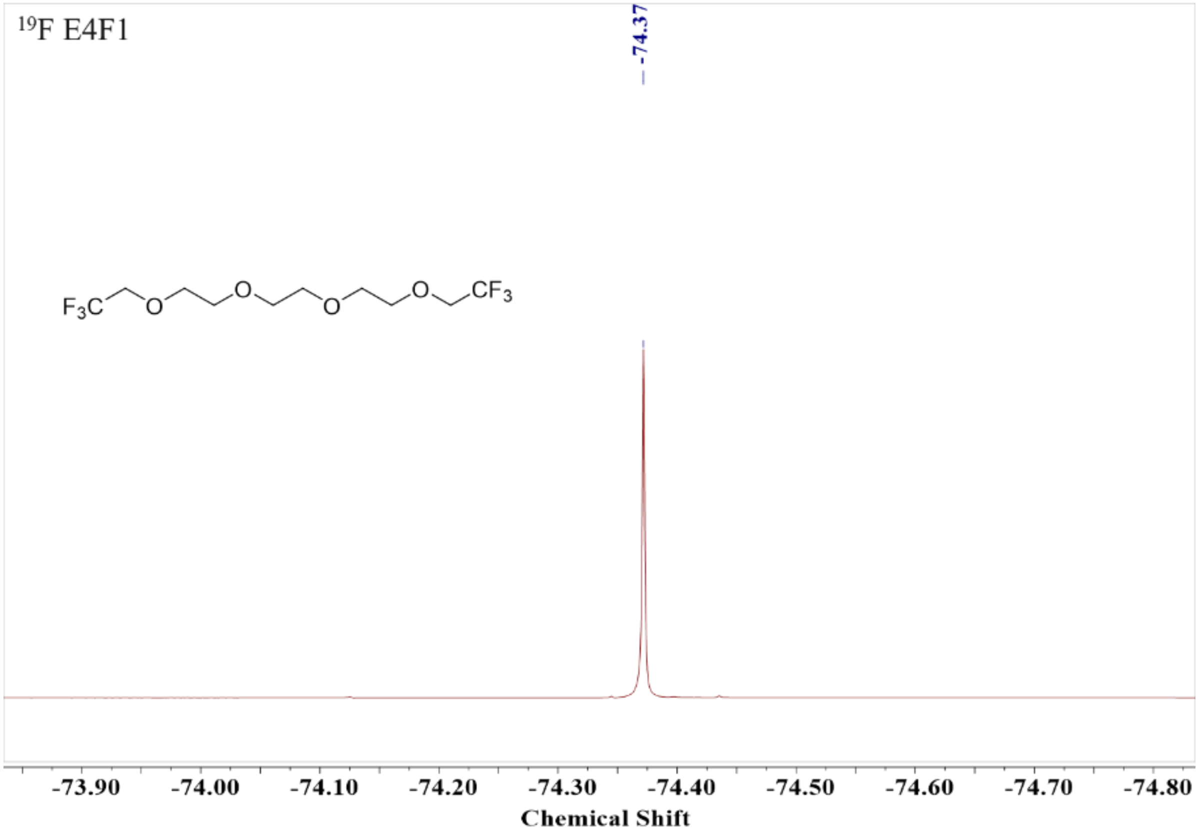

$^{19}$F E4F1
-74.37
$F_3C$ O O O O $CF_3$
-73.90
-74.00
-74.10
-74.20
-74.30
-74.40
-74.50
-74.60
-74.70
-74.80
Chemical Shift

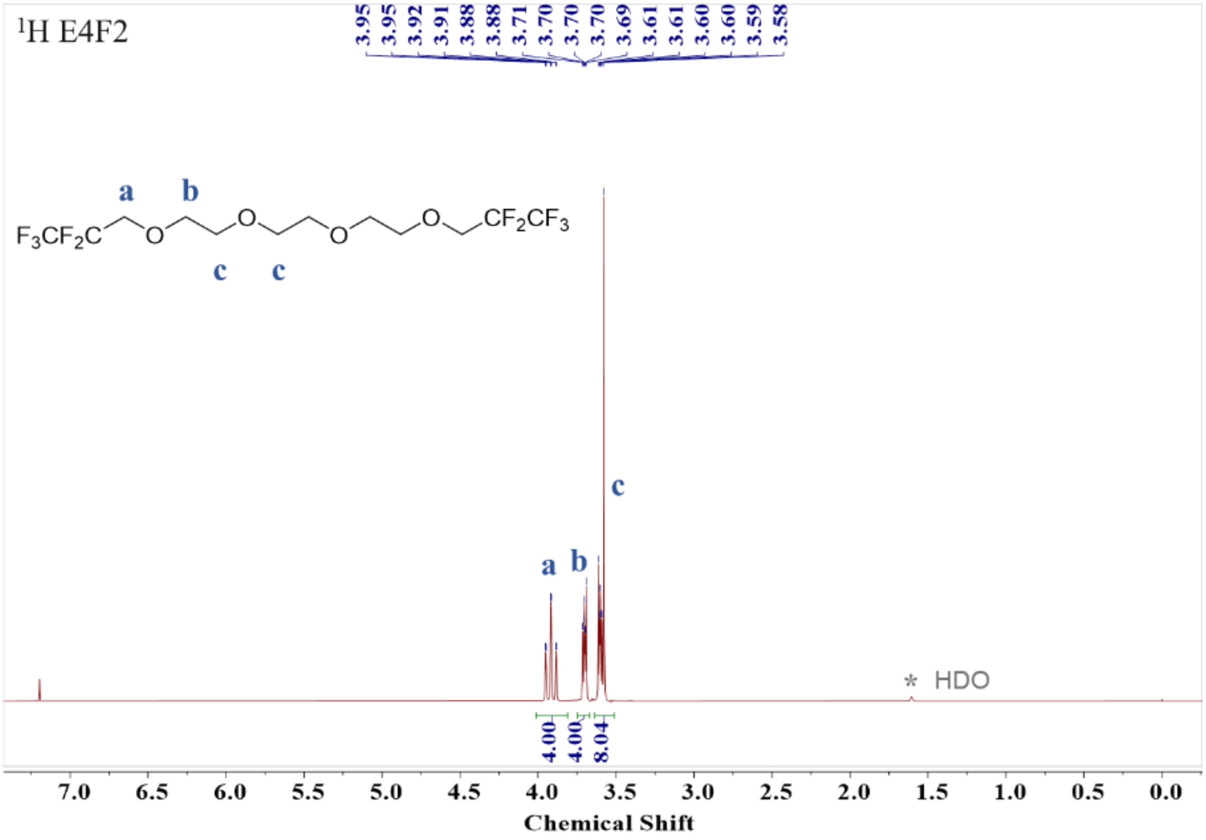

$^1$H E4F2
3.95
3.95
3.92
3.91
3.88
3.88
3.71
3.70
3.70
3.70
3.69
3.61
3.61
3.60
3.60
3.59
3.58
a
b
$F_3CF_2C$ O O O O $CF_2CF_3$
c
c
c
a
b
* HDO
4.00
4.00
8.04
7.0
6.5
6.0
5.5
5.0
4.5
4.0
3.5
3.0
2.5
2.0
1.5
1.0
0.5
0.0
Chemical Shift

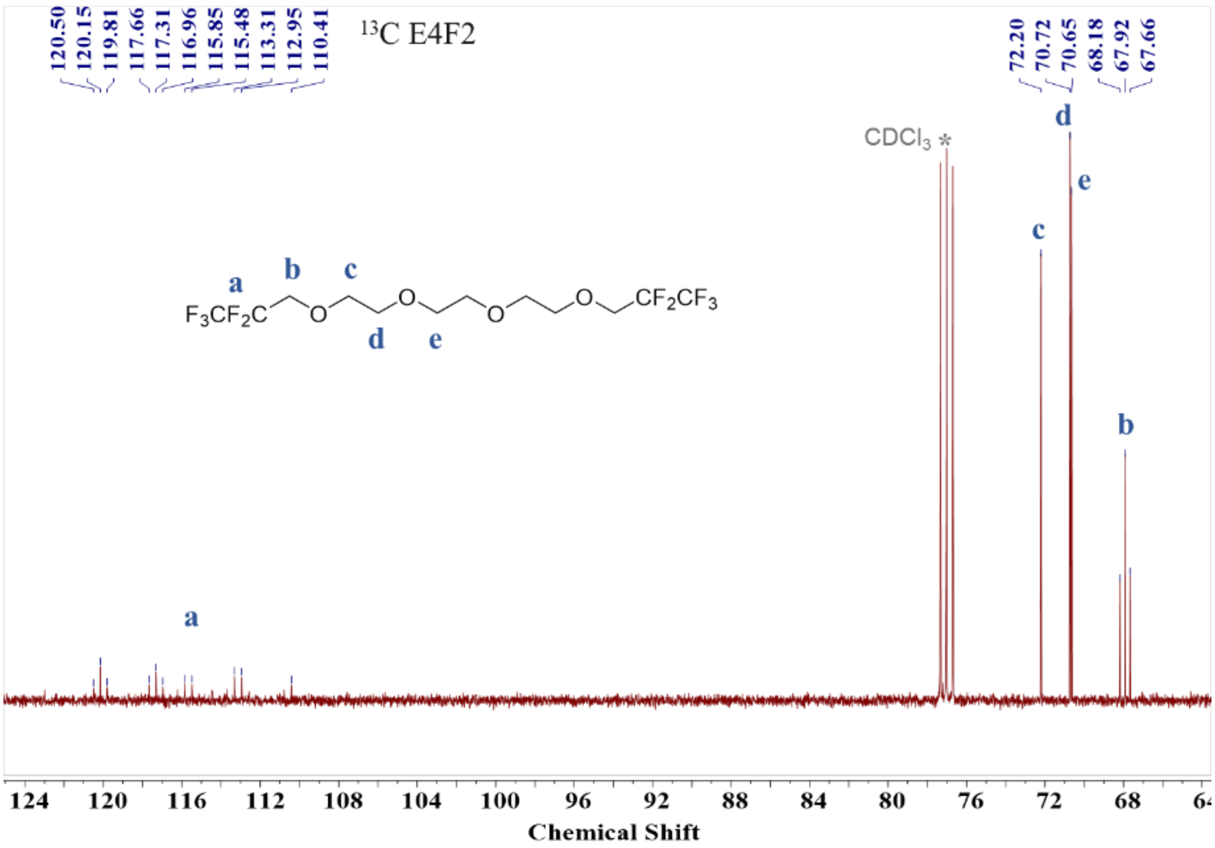
120.50
120.15
119.81
117.66
117.31
116.96
115.85
115.48
113.31
112.95
110.41
13C E4F2
72.20
70.72
70.65
68.18
67.92
67.66
CDCl3 *
d
e
c
b
a
b
c
F3CF2C
O
O
O
O
CF2CF3
d
e
a
124
120
116
112
108
104
100
96
92
88
84
80
76
72
68
Chemical Shift

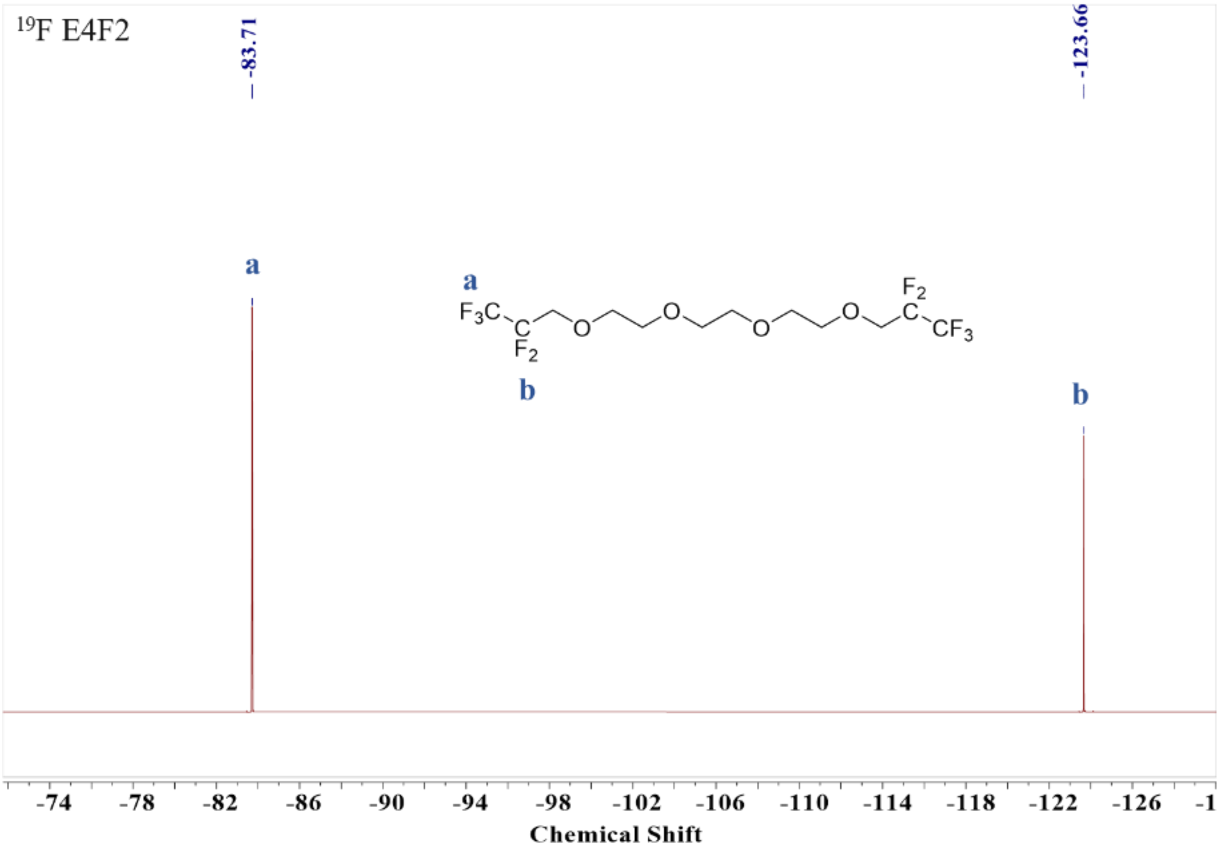
19F E4F2
-83.71
-123.66
a
a
F3C
C
F2
O
O
O
O
F2
C
CF3
b
b
-74
-78
-82
-86
-90
-94
-98
-102
-106
-110
-114
-118
-122
-126
Chemical Shift

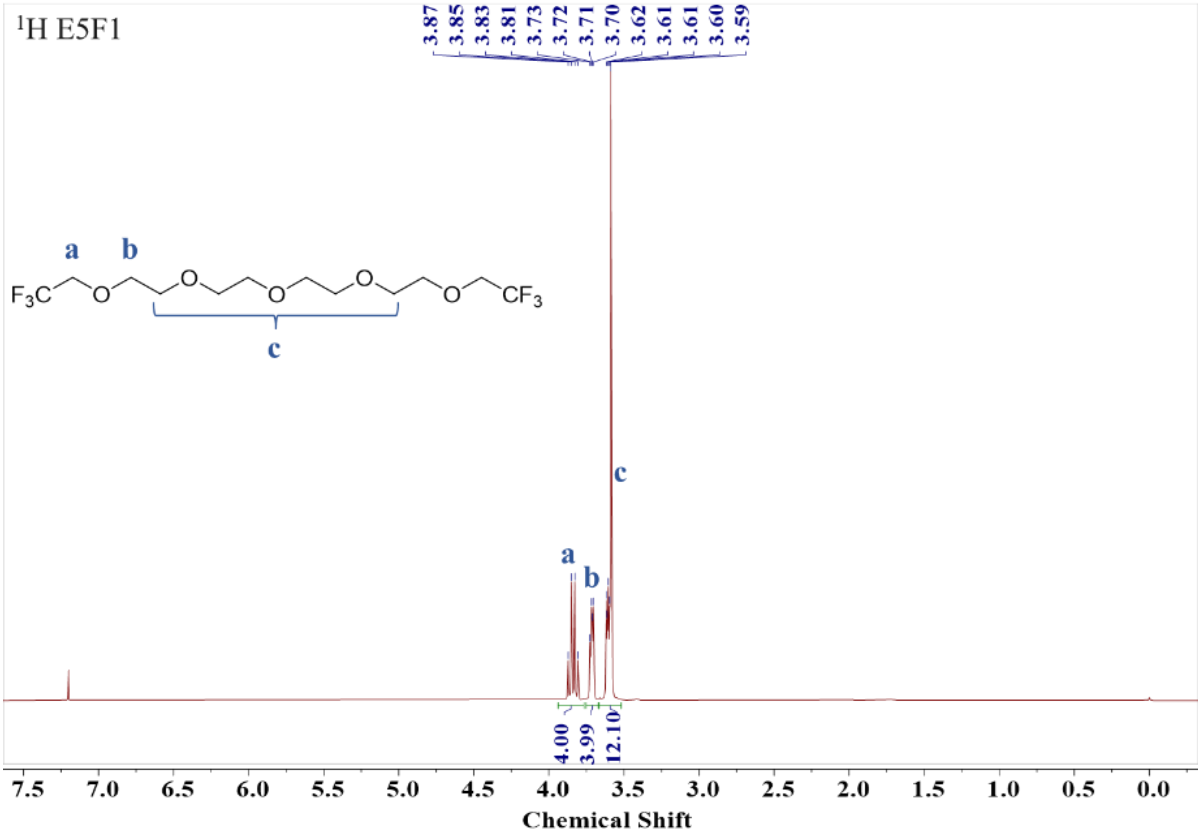

$^1$H E5F1
3.87
3.85
3.83
3.81
3.73
3.72
3.71
3.70
3.62
3.61
3.61
3.60
3.59
a
b
c
$F_3C$
O
$CF_3$
4.00
3.99
12.10
7.5
7.0
6.5
6.0
5.5
5.0
4.5
4.0
3.5
3.0
2.5
2.0
1.5
1.0
0.5
0.0
Chemical Shift

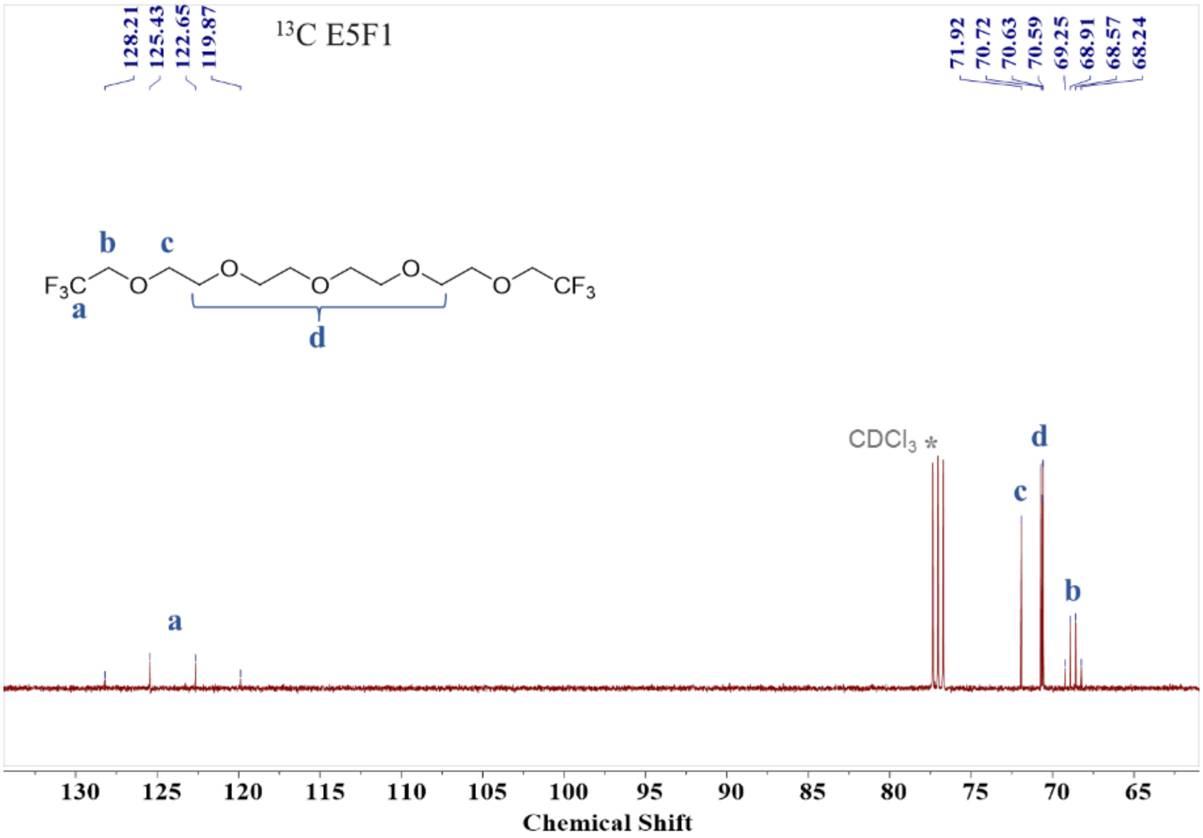

128.21
125.43
122.65
119.87
$^{13}$C E5F1
71.92
70.72
70.63
70.59
69.25
68.91
68.57
68.24
b
c
a
d
$F_3C$
O
$CF_3$
$CDCl_3$ *
130
125
120
115
110
105
100
95
90
85
80
75
70
65
Chemical Shift

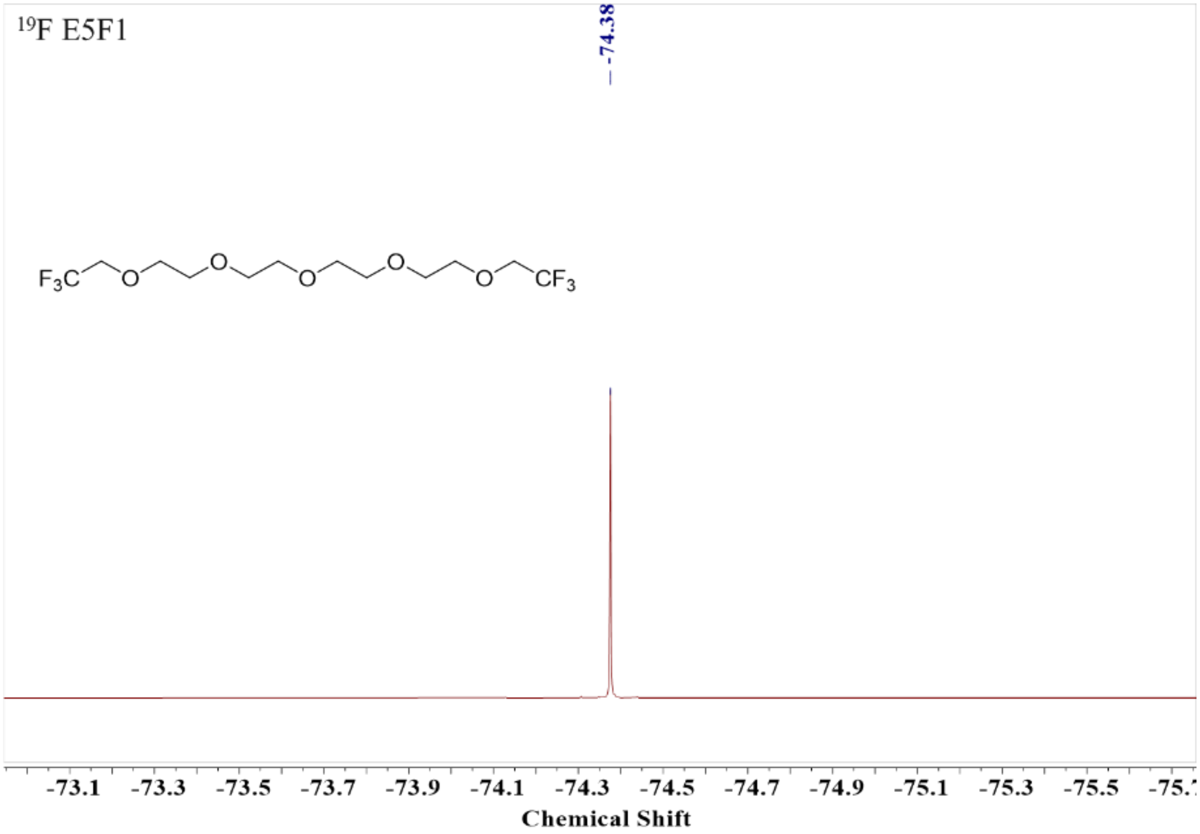
$^{19}$F E5F1
-74.38
$F_3C$
O
O
O
O
O
$CF_3$
-73.1
-73.3
-73.5
-73.7
-73.9
-74.1
-74.3
-74.5
-74.7
-74.9
-75.1
-75.3
-75.5
Chemical Shift

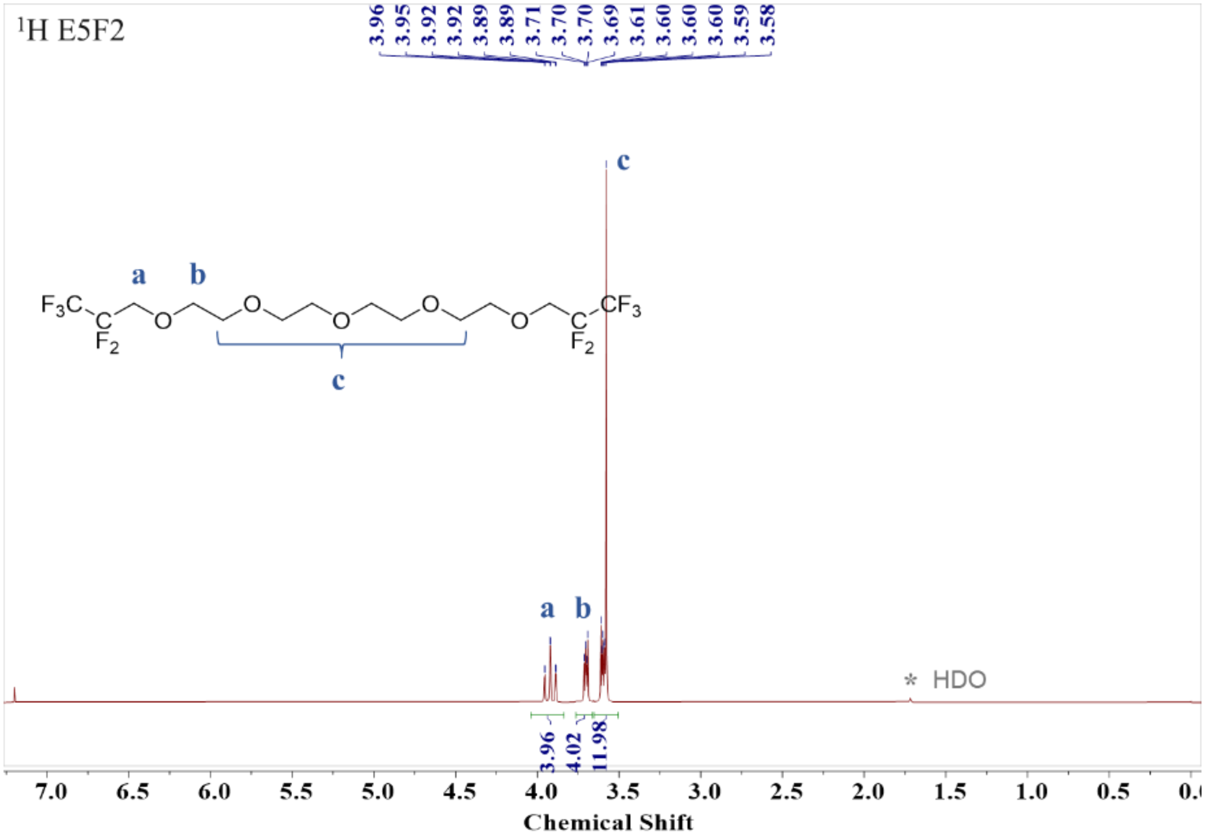
$^{1}$H E5F2
3.96
3.95
3.92
3.92
3.89
3.89
3.71
3.70
3.70
3.69
3.61
3.60
3.60
3.60
3.59
3.58
c
a
b
$F_3C$
C
$F_2$
O
O
O
O
O
C
$F_2$
$CF_3$
c
a
b
* HDO
3.96
4.02
11.98
7.0
6.5
6.0
5.5
5.0
4.5
4.0
3.5
3.0
2.5
2.0
1.5
1.0
0.5
Chemical Shift

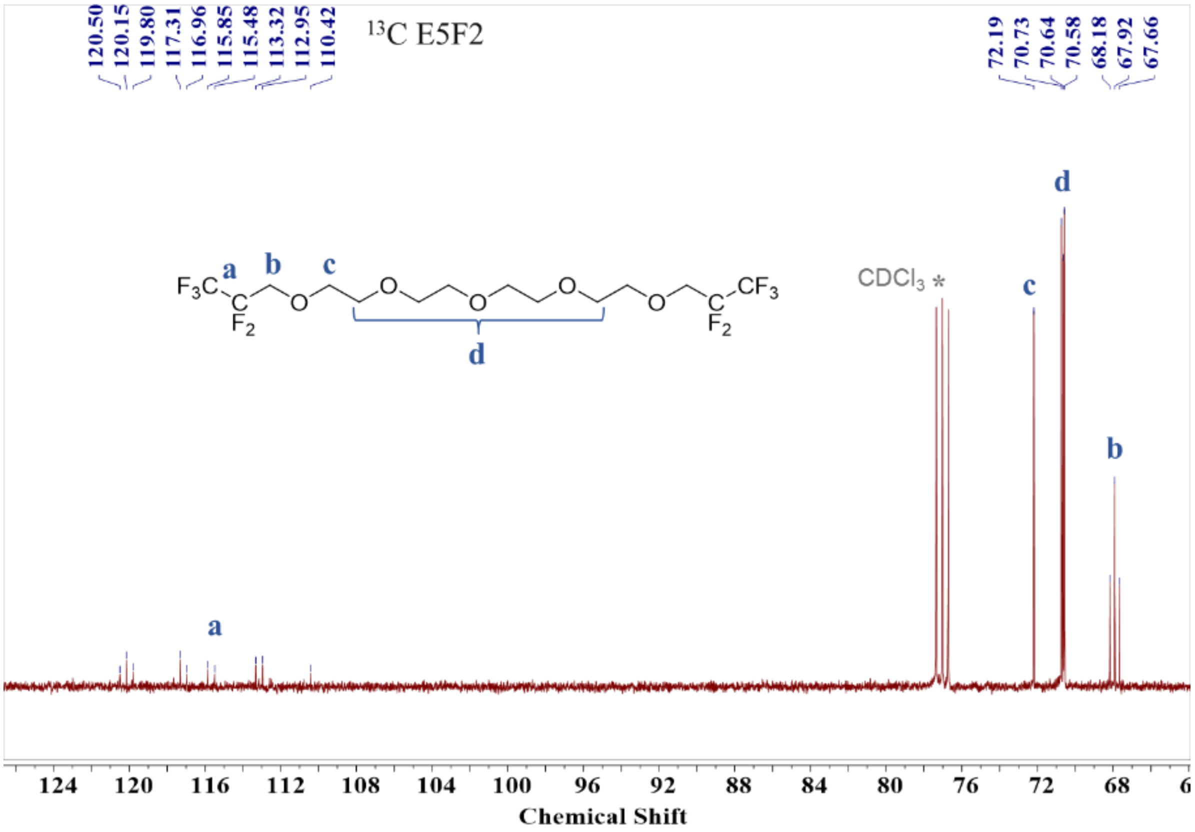
120.50
120.15
119.80
117.31
116.96
115.85
115.48
113.32
112.95
110.42
$^{13}$C E5F2
72.19
70.73
70.64
70.58
68.18
67.92
67.66
$F_3C$
a
b
c
O
$CF_3$
$F_2$
d
CDCl$_3$ *
c
d
b
a
124
120
116
112
108
104
100
96
92
88
84
80
76
72
68
Chemical Shift

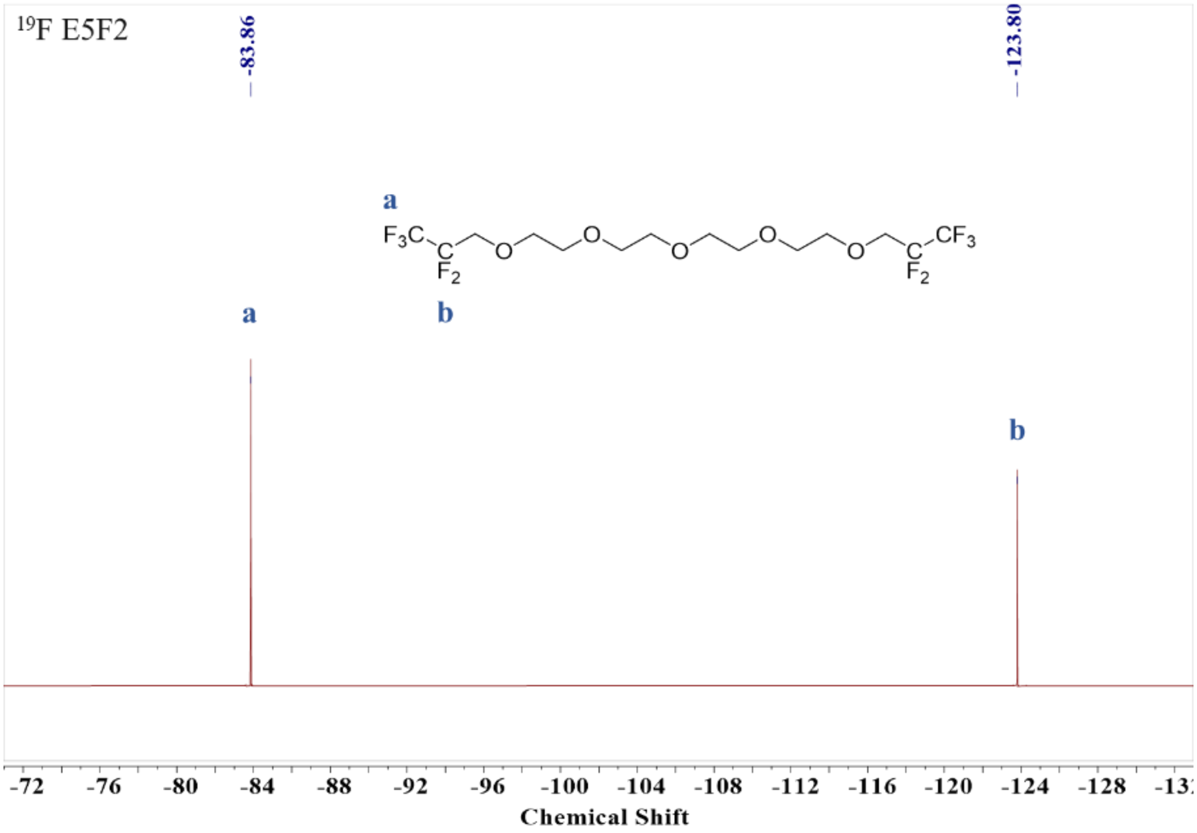
$^{19}$F E5F2
-83.86
-123.80
a
$F_3C$
O
$CF_3$
$F_2$
a
b
b
-72
-76
-80
-84
-88
-92
-96
-100
-104
-108
-112
-116
-120
-124
-128
Chemical Shift

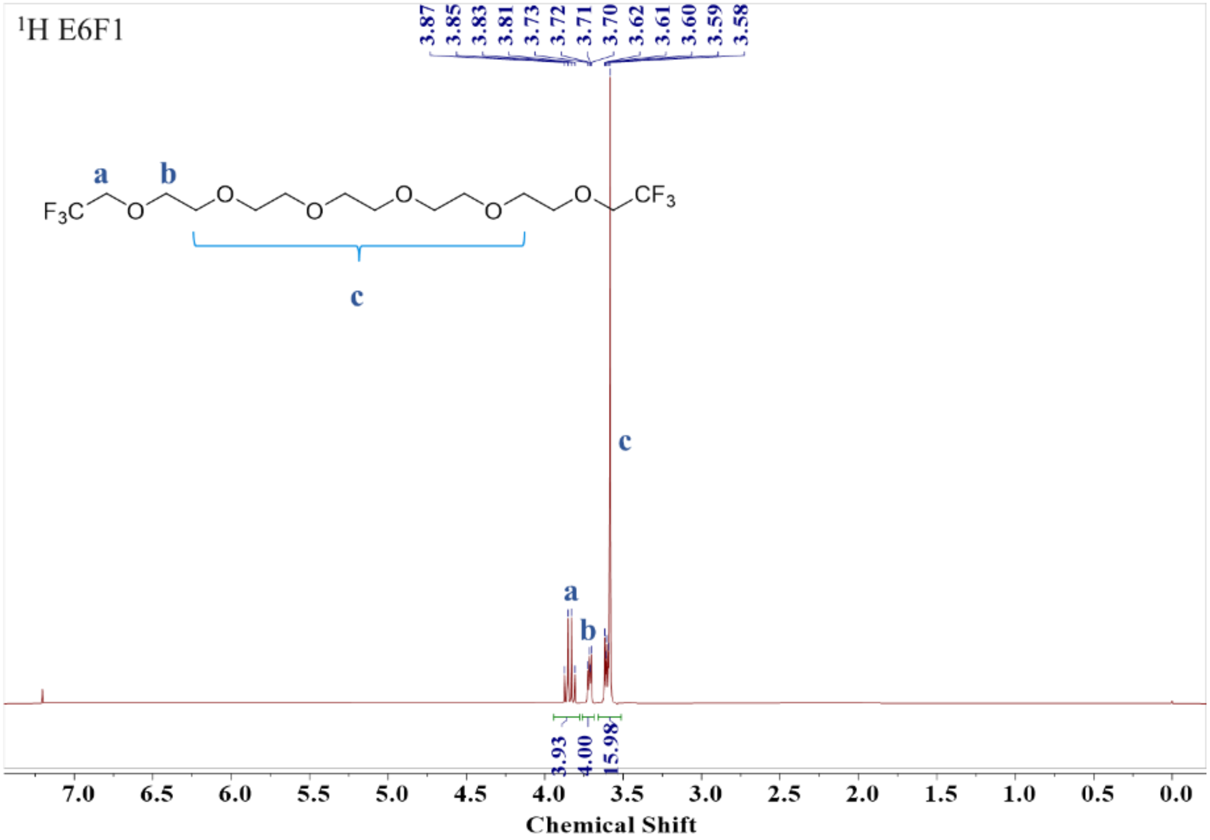

$^1$H E6F1
3.87
3.85
3.83
3.81
3.73
3.72
3.71
3.70
3.62
3.61
3.60
3.59
3.58
a
b
$F_3C$
O
O
O
O
O
$CF_3$
c
c
a
b
3.93
4.00
15.98
7.0
6.5
6.0
5.5
5.0
4.5
4.0
3.5
3.0
2.5
2.0
1.5
1.0
0.5
0.0
Chemical Shift

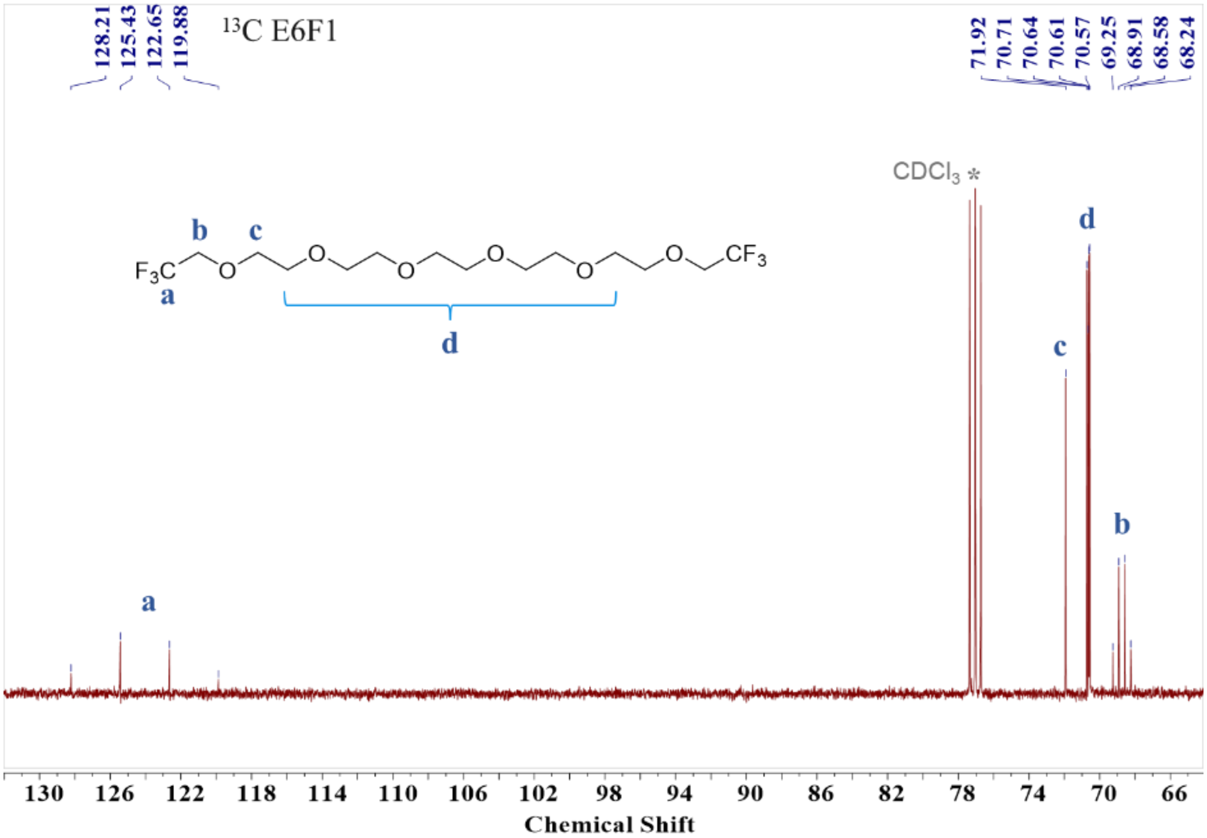

128.21
125.43
122.65
119.88
$^{13}$C E6F1
71.92
70.71
70.64
70.61
70.57
69.25
68.91
68.58
68.24
$CDCl_3$ *
b
c
$F_3C$
a
O
O
O
O
O
O
$CF_3$
d
d
c
b
a
130
126
122
118
114
110
106
102
98
94
90
86
82
78
74
70
66
Chemical Shift

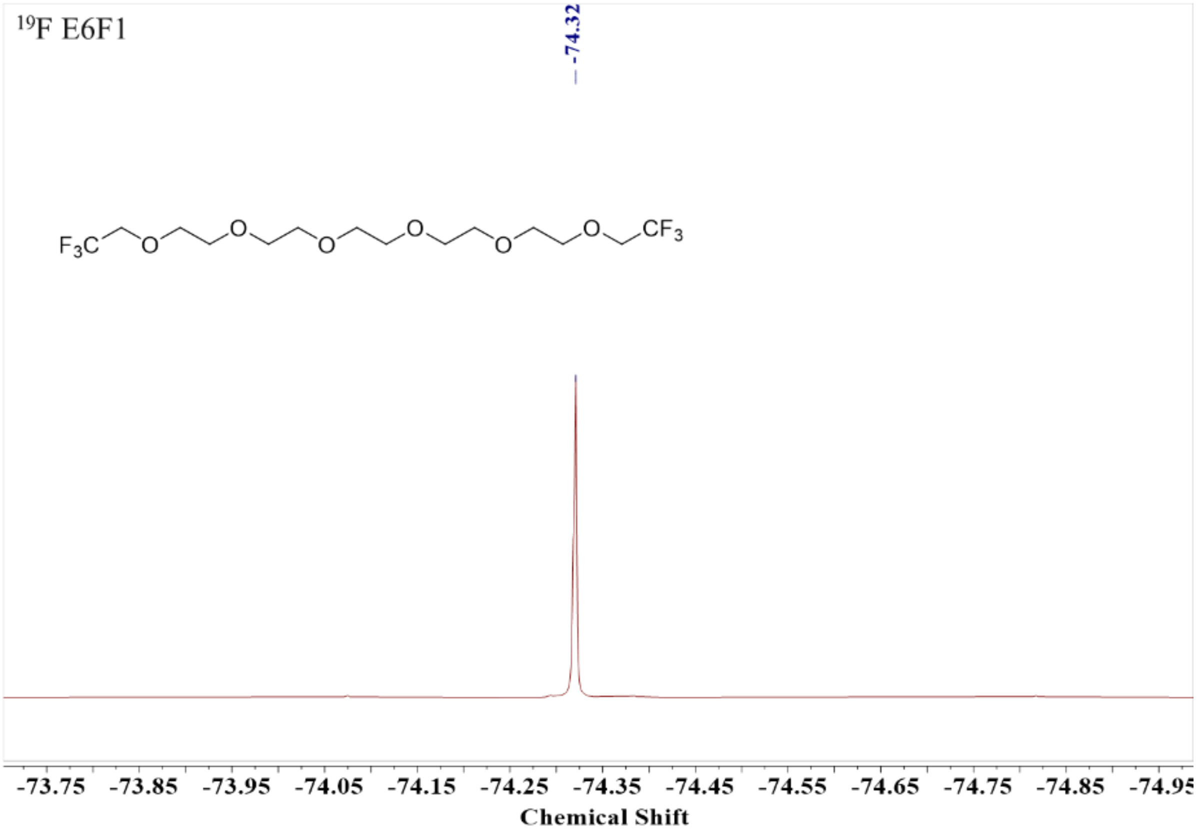
¹⁹F E6F1
-74.32
F₃C O O O O O O CF₃
-73.75 -73.85 -73.95 -74.05 -74.15 -74.25 -74.35 -74.45 -74.55 -74.65 -74.75 -74.85 -74.95
Chemical Shift

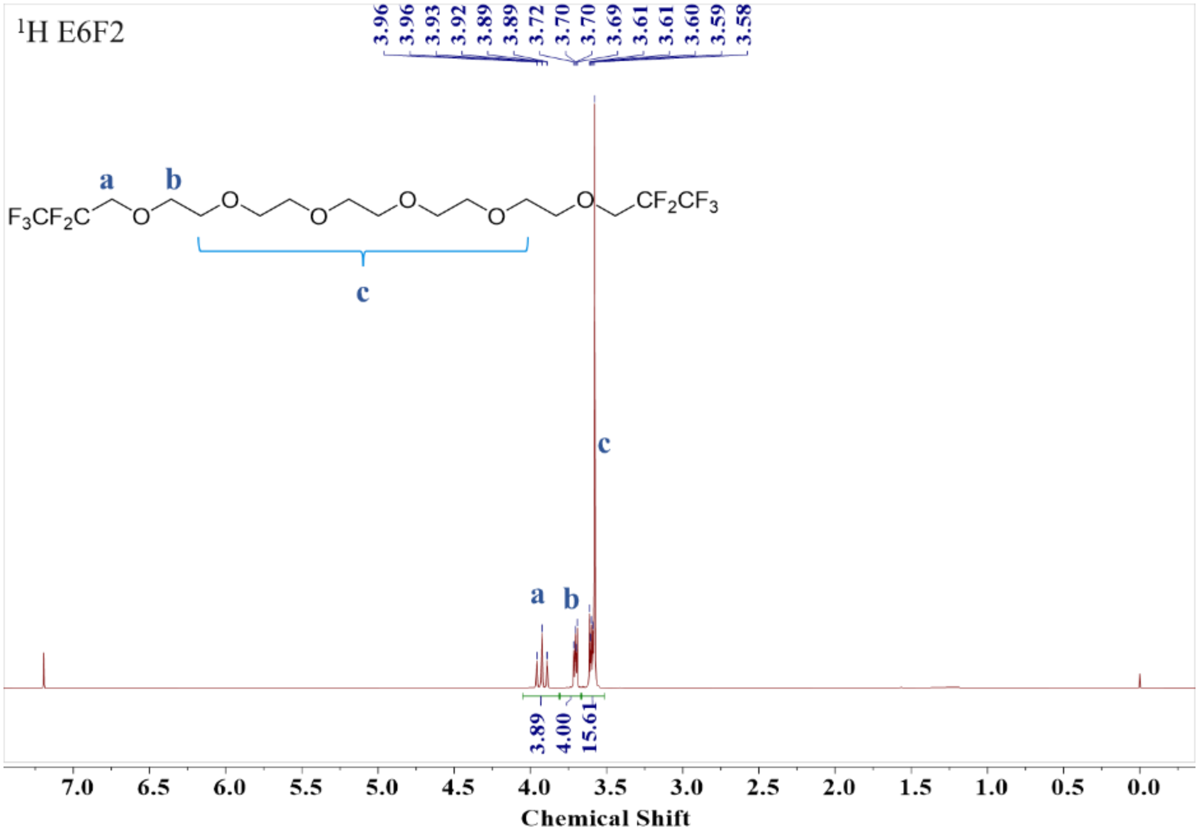
¹H E6F2
3.96 3.96 3.93 3.92 3.89 3.89 3.72 3.70 3.70 3.69 3.61 3.61 3.60 3.59 3.58
a b
F₃CF₂C O O O O O O CF₂CF₃
c
c
a b
3.89 4.00 15.61
7.0 6.5 6.0 5.5 5.0 4.5 4.0 3.5 3.0 2.5 2.0 1.5 1.0 0.5 0.0
Chemical Shift

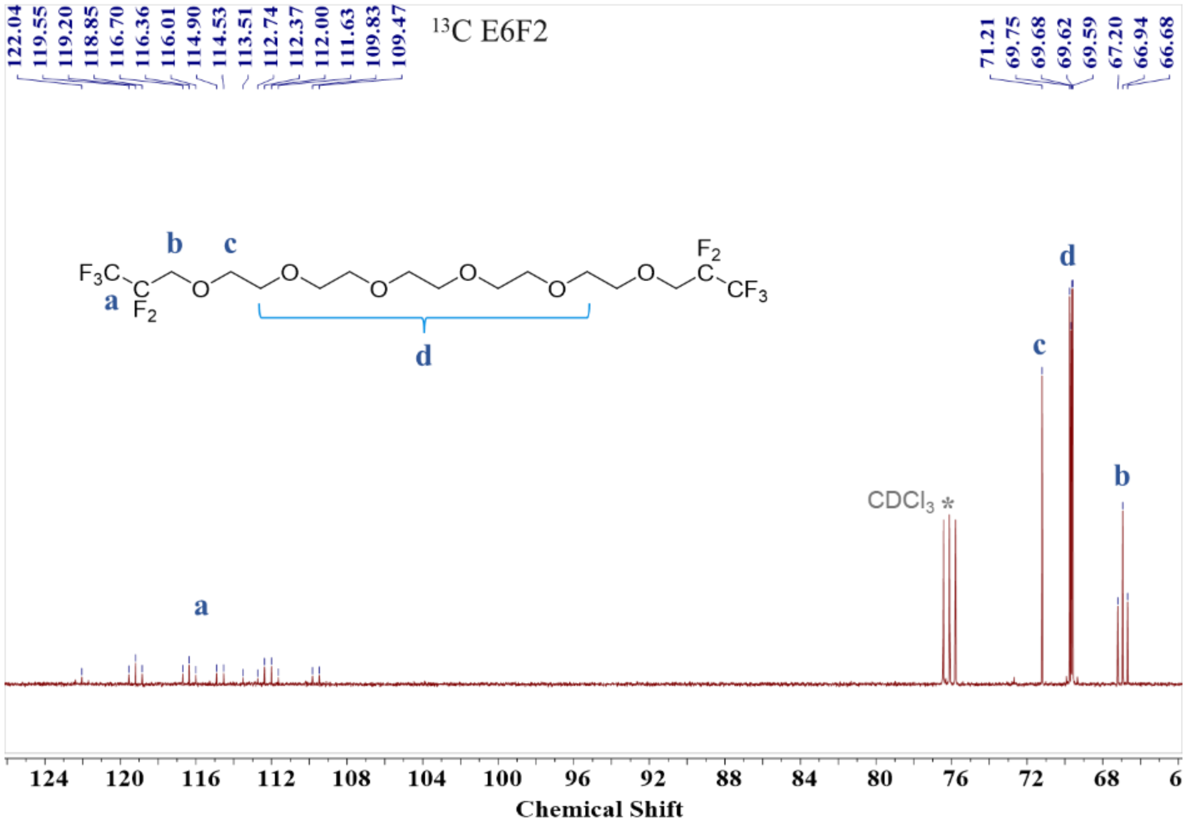
122.04
119.55
119.20
118.85
116.70
116.36
116.01
114.90
114.53
113.51
112.74
112.37
112.00
111.63
109.83
109.47
$^{13}$C E6F2
71.21
69.75
69.68
69.62
69.59
67.20
66.94
66.68
b
c
a
d
d
c
b
CDCl$_3$ *
a
124
120
116
112
108
104
100
96
92
88
84
80
76
72
68
6
Chemical Shift

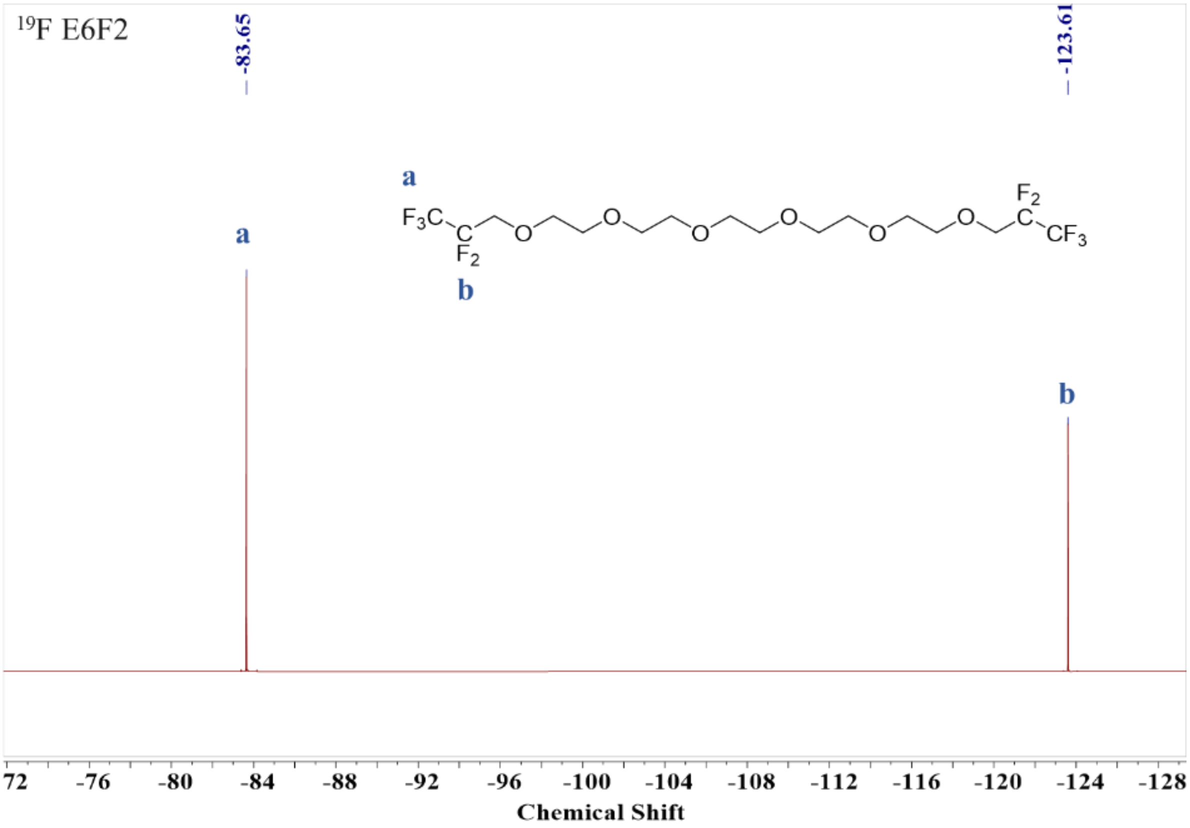
$^{19}$F E6F2
-83.65
-123.61
a
a
b
b
72
-76
-80
-84
-88
-92
-96
-100
-104
-108
-112
-116
-120
-124
-128
Chemical Shift

**Figure S2**. Nuclear magnetic resonance (NMR) spectroscopy of synthesized compounds. $^{1}H$, $^{13}C$, and $^{19}F$ (proton decoupled) NMR spectra were taken on a Bruker Ascend 9.4 T / 400 MHz instrument. NMR sample was prepared by dissolving several milligrams of product into 0.5 mL deuterated chloroform.

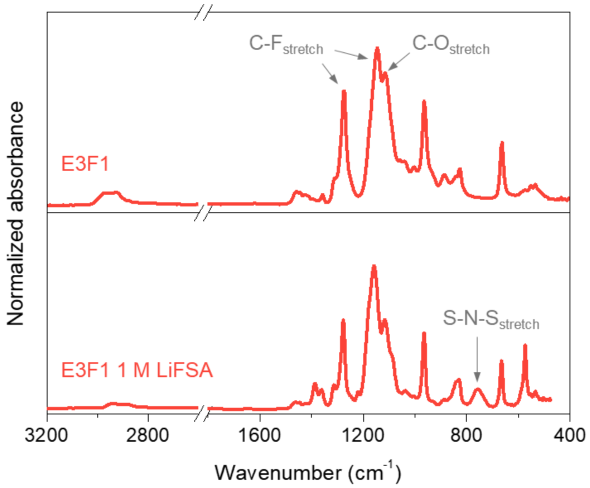
Normalized absorbance
C-F$_{stretch}$
C-O$_{stretch}$
E3F1
S-N-S$_{stretch}$
E3F1 1 M LiFSA
3200
2800
1600
1200
800
400
Wavenumber (cm$^{-1}$)

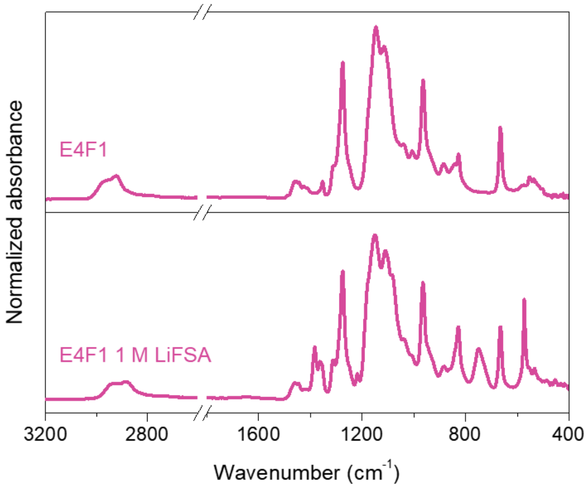
Normalized absorbance
E4F1
E4F1 1 M LiFSA
3200
2800
1600
1200
800
400
Wavenumber (cm$^{-1}$)

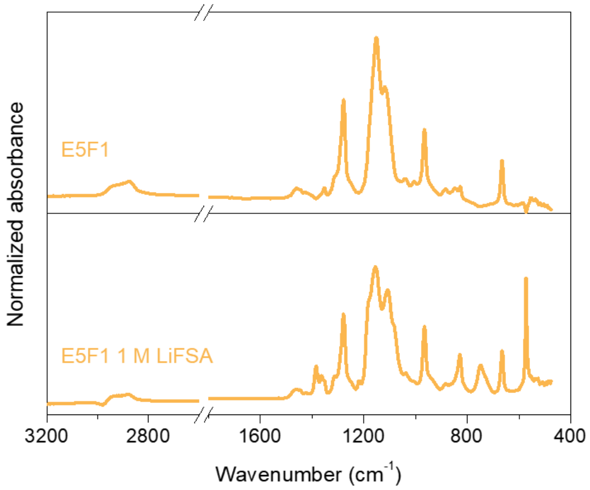
Normalized absorbance
E5F1
E5F1 1 M LiFSA
3200
2800
1600
1200
800
400
Wavenumber (cm$^{-1}$)

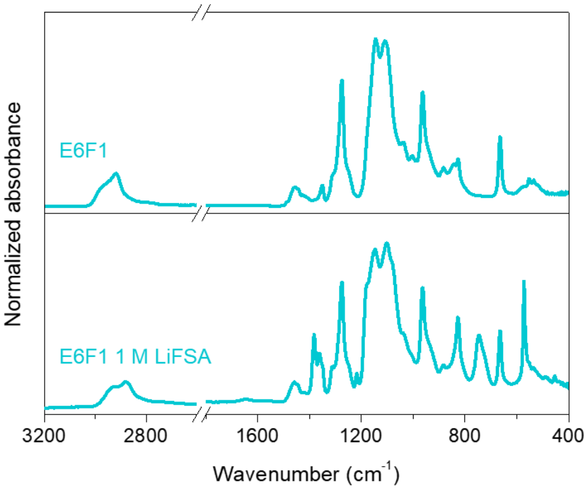
Normalized absorbance
E6F1
E6F1 1 M LiFSA
3200
2800
1600
1200
800
400
Wavenumber (cm$^{-1}$)

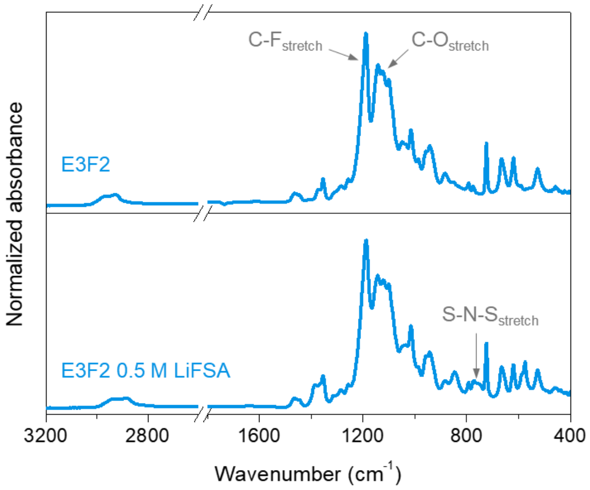
Normalized absorbance
C-F$_{stretch}$
C-O$_{stretch}$
E3F2
S-N-S$_{stretch}$
E3F2 0.5 M LiFSA
3200
2800
1600
1200
800
400
Wavenumber (cm$^{-1}$)

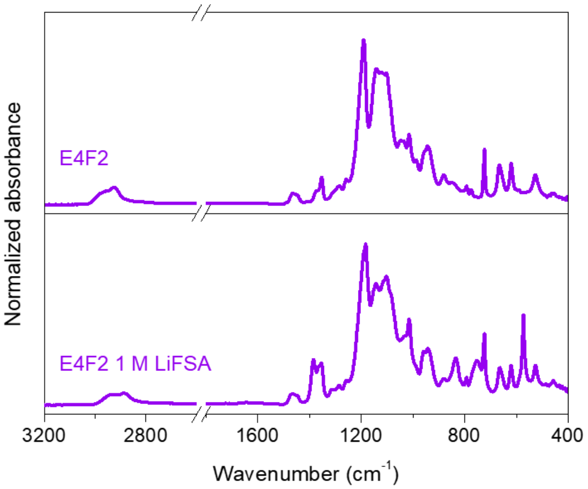
Normalized absorbance
E4F2
E4F2 1 M LiFSA
3200
2800
1600
1200
800
400
Wavenumber (cm$^{-1}$)

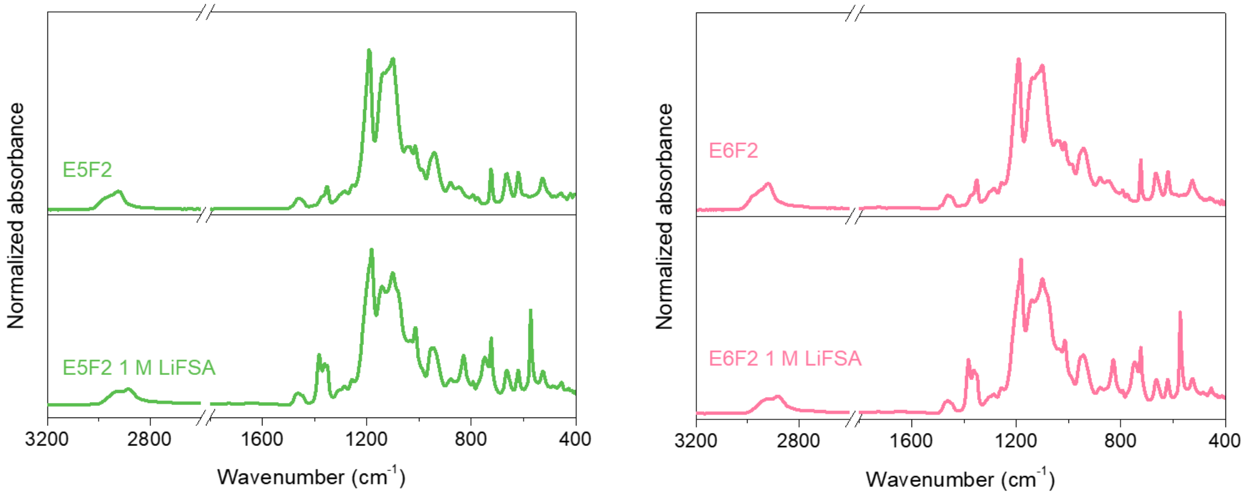

**Figure S3**. FT-IR spectra of the compounds and their LiFSA solutions. The functional groups indicated in E3F1 correspond to the same functional groups in E4F1, E5F1, and E6F1. The functional groups indicated in E3F2 correspond to the same functional groups in E4F2, E5F2, and E6F2.

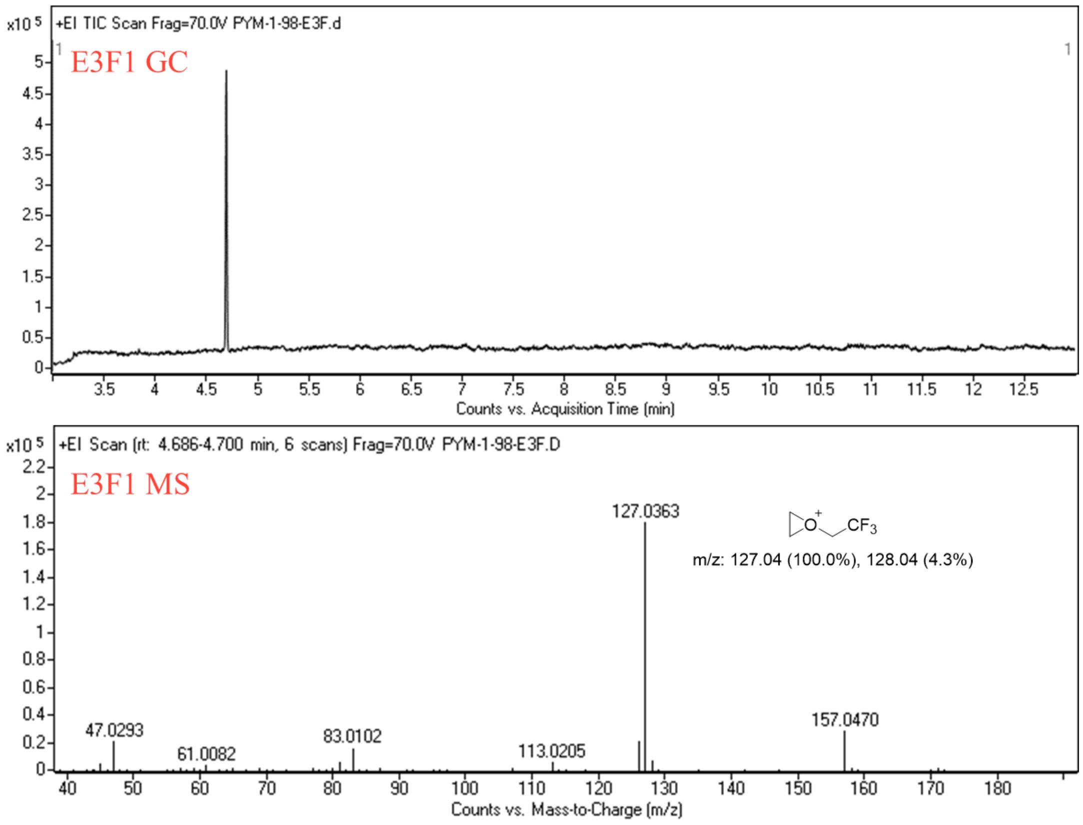

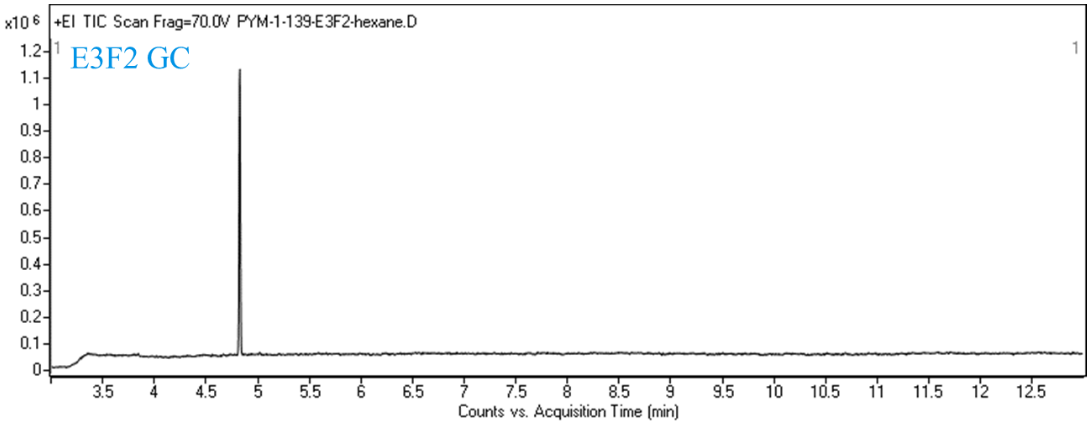
x10 6
+EI TIC Scan Frag=70.0V PYM-1-139-E3F2-hexane.D
E3F2 GC
1
1
1.2
1.1
1
0.9
0.8
0.7
0.6
0.5
0.4
0.3
0.2
0.1
0
3.5
4
4.5
5
5.5
6
6.5
7
7.5
8
8.5
9
9.5
10
10.5
11
11.5
12
12.5
Counts vs. Acquisition Time (min)

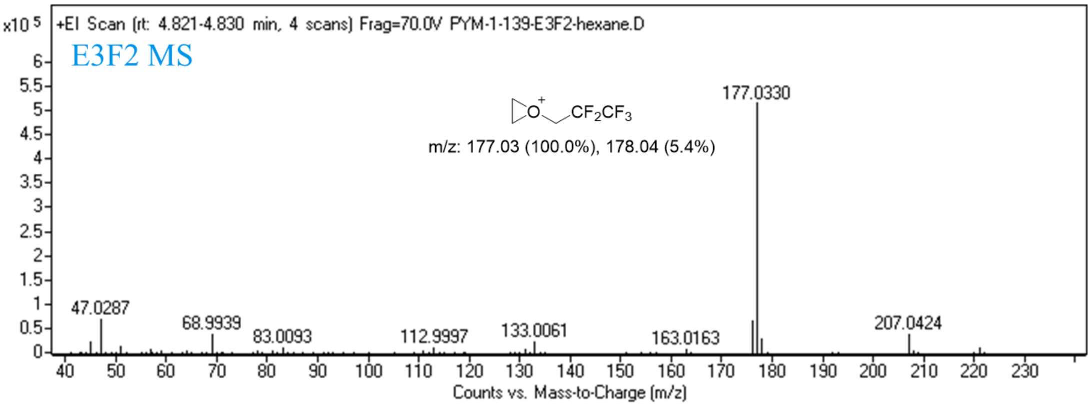
x10 5
+EI Scan (rt: 4.821-4.830 min, 4 scans) Frag=70.0V PYM-1-139-E3F2-hexane.D
E3F2 MS
O+
CF2CF3
m/z: 177.03 (100.0%), 178.04 (5.4%)
177.0330
47.0287
68.9939
83.0093
112.9997
133.0061
163.0163
207.0424
6
5.5
5
4.5
4
3.5
3
2.5
2
1.5
1
0.5
0
40
50
60
70
80
90
100
110
120
130
140
150
160
170
180
190
200
210
220
230
Counts vs. Mass-to-Charge (m/z)

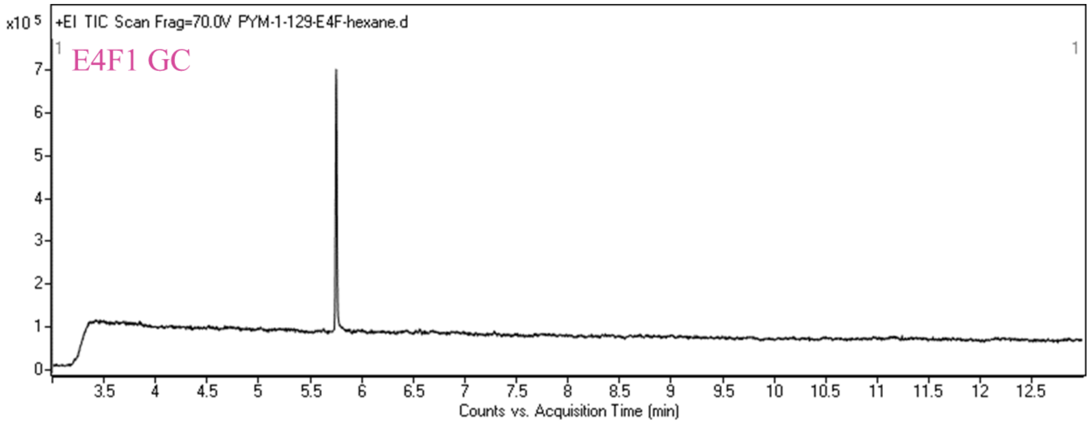
x10 5
+EI TIC Scan Frag=70.0V PYM-1-129-E4F-hexane.d
E4F1 GC
1
1
7
6
5
4
3
2
1
0
3.5
4
4.5
5
5.5
6
6.5
7
7.5
8
8.5
9
9.5
10
10.5
11
11.5
12
12.5
Counts vs. Acquisition Time (min)

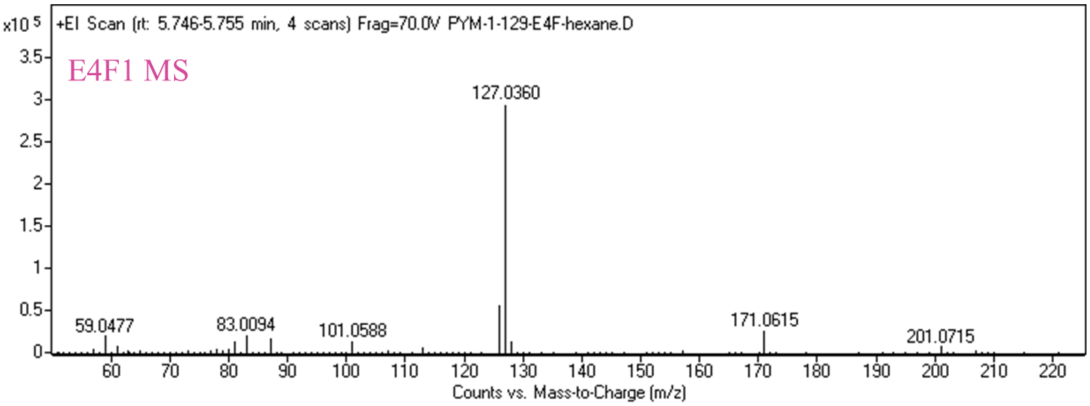
x10 5
+EI Scan (rt: 5.746-5.755 min, 4 scans) Frag=70.0V PYM-1-129-E4F-hexane.D
E4F1 MS
127.0360
59.0477
83.0094
101.0588
171.0615
201.0715
3.5
3
2.5
2
1.5
1
0.5
0
60
70
80
90
100
110
120
130
140
150
160
170
180
190
200
210
220
Counts vs. Mass-to-Charge (m/z)

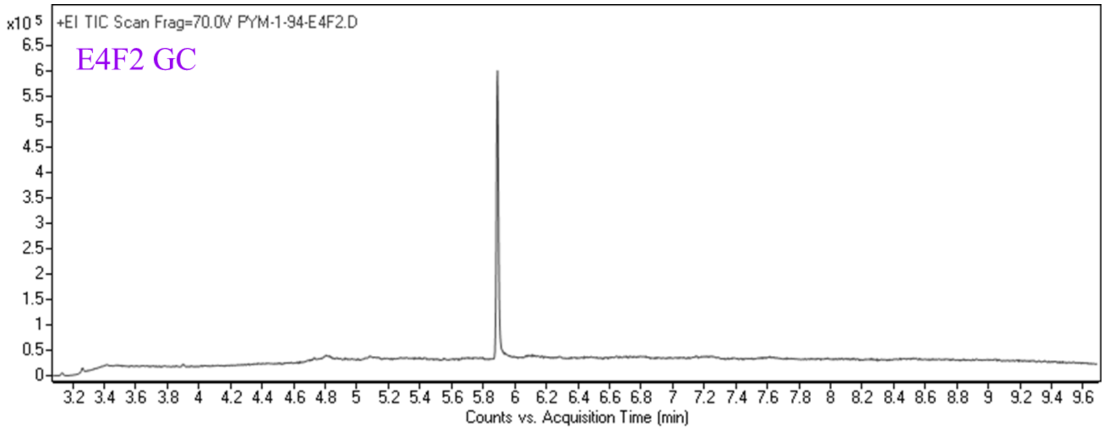
x10 5
+EI TIC Scan Frag=70.0V PYM-1-94-E4F2.D
E4F2 GC
6.5
6
5.5
5
4.5
4
3.5
3
2.5
2
1.5
1
0.5
0
3.2 3.4 3.6 3.8 4 4.2 4.4 4.6 4.8 5 5.2 5.4 5.6 5.8 6 6.2 6.4 6.6 6.8 7 7.2 7.4 7.6 7.8 8 8.2 8.4 8.6 8.8 9 9.2 9.4 9.6
Counts vs. Acquisition Time (min)

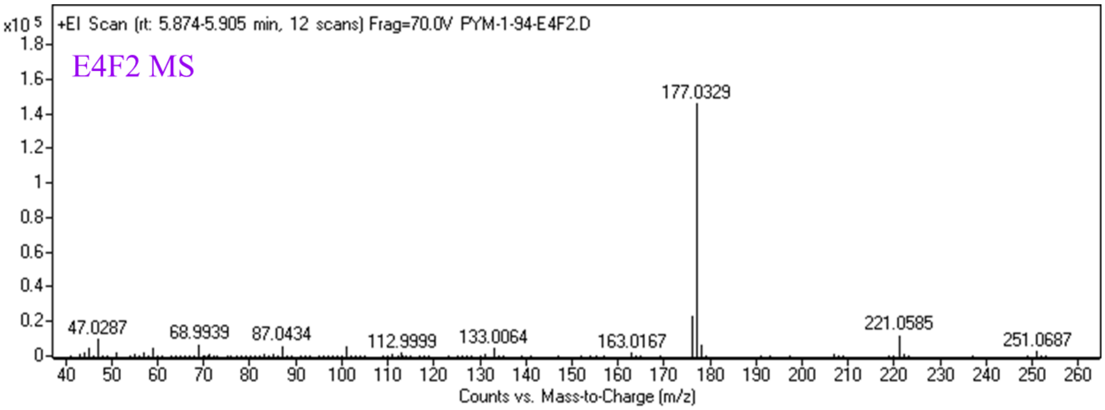
x10 5
+EI Scan (rt: 5.874-5.905 min, 12 scans) Frag=70.0V PYM-1-94-E4F2.D
E4F2 MS
1.8
1.6
1.4
1.2
1
0.8
0.6
0.4
0.2
0
177.0329
47.0287
68.9939
87.0434
112.9999
133.0064
163.0167
221.0585
251.0687
40 50 60 70 80 90 100 110 120 130 140 150 160 170 180 190 200 210 220 230 240 250 260
Counts vs. Mass-to-Charge (m/z)

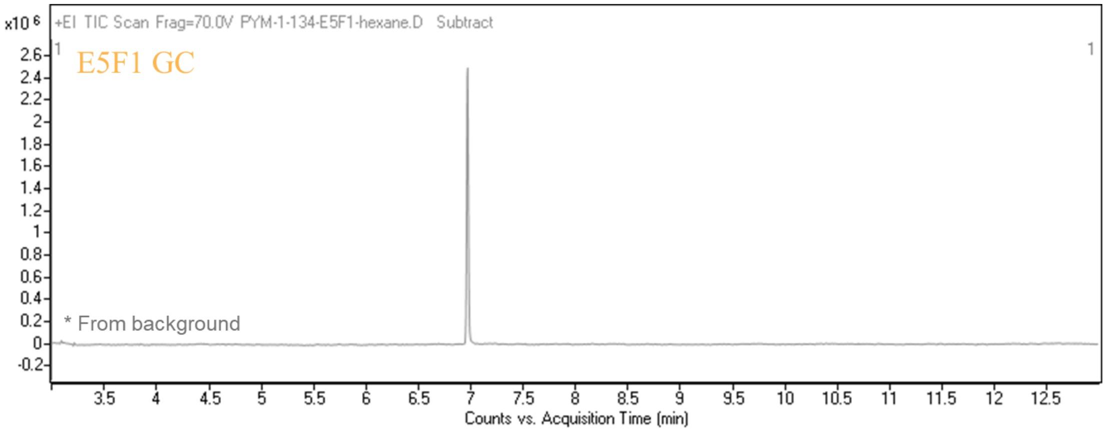
x10 6
+EI TIC Scan Frag=70.0V PYM-1-134-E5F1-hexane.D Subtract
1
1
E5F1 GC
2.6
2.4
2.2
2
1.8
1.6
1.4
1.2
1
0.8
0.6
0.4
0.2
0
-0.2
* From background
3.5 4 4.5 5 5.5 6 6.5 7 7.5 8 8.5 9 9.5 10 10.5 11 11.5 12 12.5
Counts vs. Acquisition Time (min)

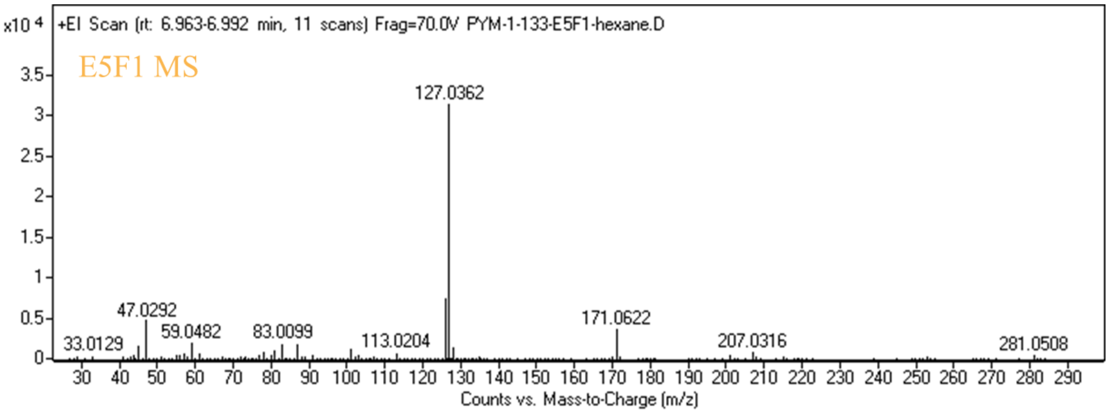
x10 4
+EI Scan (rt: 6.963-6.992 min, 11 scans) Frag=70.0V PYM-1-133-E5F1-hexane.D
E5F1 MS
3.5
3
2.5
2
1.5
1
0.5
0
127.0362
47.0292
33.0129
59.0482
83.0099
113.0204
171.0622
207.0316
281.0508
30 40 50 60 70 80 90 100 110 120 130 140 150 160 170 180 190 200 210 220 230 240 250 260 270 280 290
Counts vs. Mass-to-Charge (m/z)

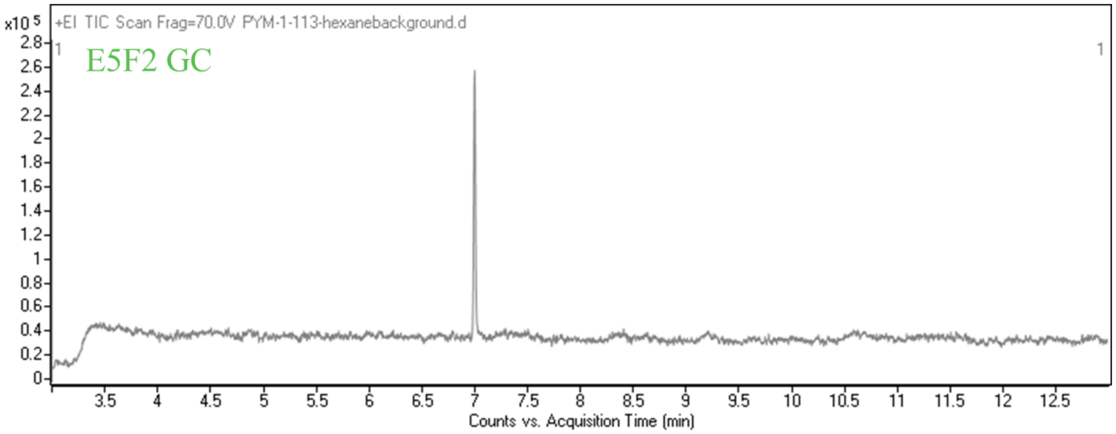
x10 5
+EI TIC Scan Frag=70.0V PYM-1-113-hexanebackground.d
E5F2 GC
1
1
2.8
2.6
2.4
2.2
2
1.8
1.6
1.4
1.2
1
0.8
0.6
0.4
0.2
0
3.5
4
4.5
5
5.5
6
6.5
7
7.5
8
8.5
9
9.5
10
10.5
11
11.5
12
12.5
Counts vs. Acquisition Time (min)

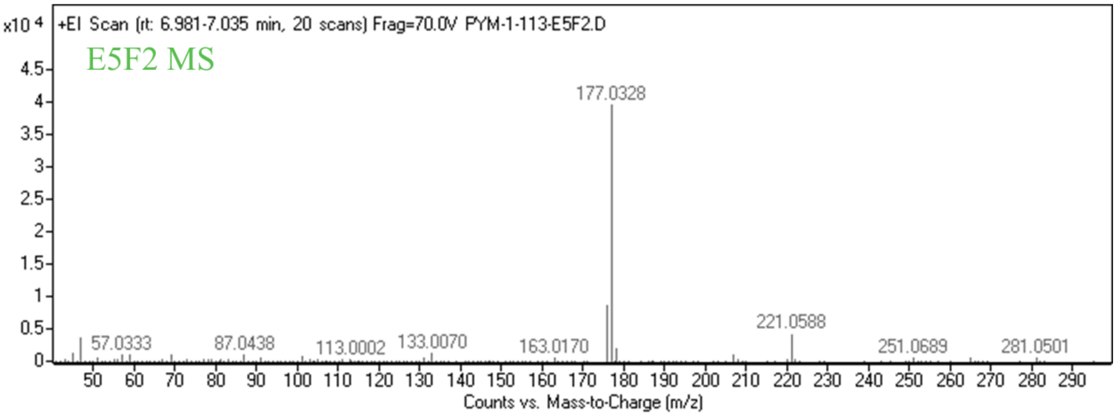
x10 4
+EI Scan (rt: 6.981-7.035 min, 20 scans) Frag=70.0V PYM-1-113-E5F2.D
E5F2 MS
177.0328
221.0588
57.0333
87.0438
113.0002
133.0070
163.0170
251.0689
281.0501
4.5
4
3.5
3
2.5
2
1.5
1
0.5
0
50
60
70
80
90
100
110
120
130
140
150
160
170
180
190
200
210
220
230
240
250
260
270
280
290
Counts vs. Mass-to-Charge (m/z)

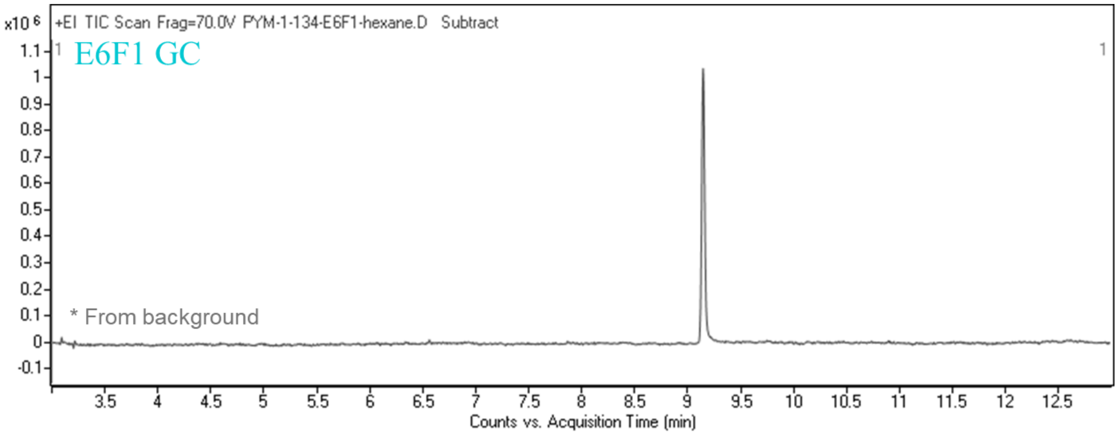
x10 6
+EI TIC Scan Frag=70.0V PYM-1-134-E6F1-hexane.D Subtract
E6F1 GC
1
1
* From background
1.1
1
0.9
0.8
0.7
0.6
0.5
0.4
0.3
0.2
0.1
0
-0.1
3.5
4
4.5
5
5.5
6
6.5
7
7.5
8
8.5
9
9.5
10
10.5
11
11.5
12
12.5
Counts vs. Acquisition Time (min)

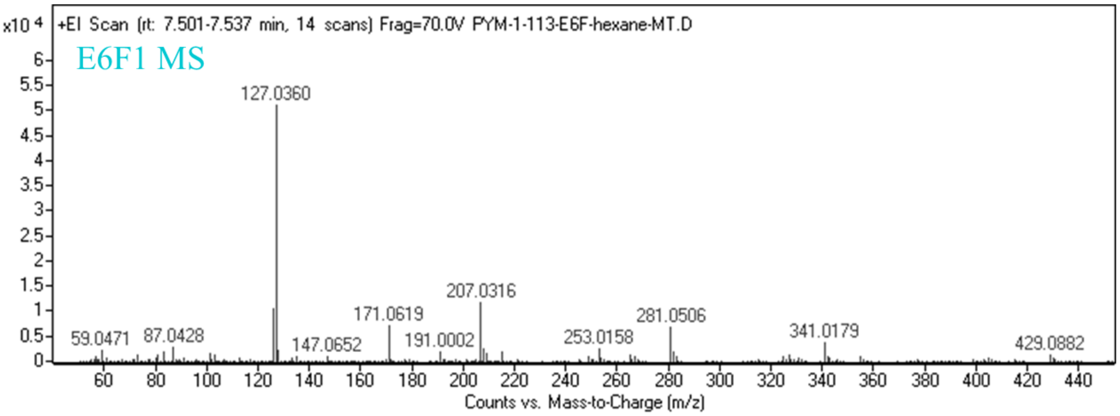
x10 4
+EI Scan (rt: 7.501-7.537 min, 14 scans) Frag=70.0V PYM-1-113-E6F-hexane-MT.D
E6F1 MS
127.0360
207.0316
171.0619
281.0506
341.0179
59.0471
87.0428
147.0652
191.0002
253.0158
429.0882
6
5.5
5
4.5
4
3.5
3
2.5
2
1.5
1
0.5
0
60
80
100
120
140
160
180
200
220
240
260
280
300
320
340
360
380
400
420
440
Counts vs. Mass-to-Charge (m/z)

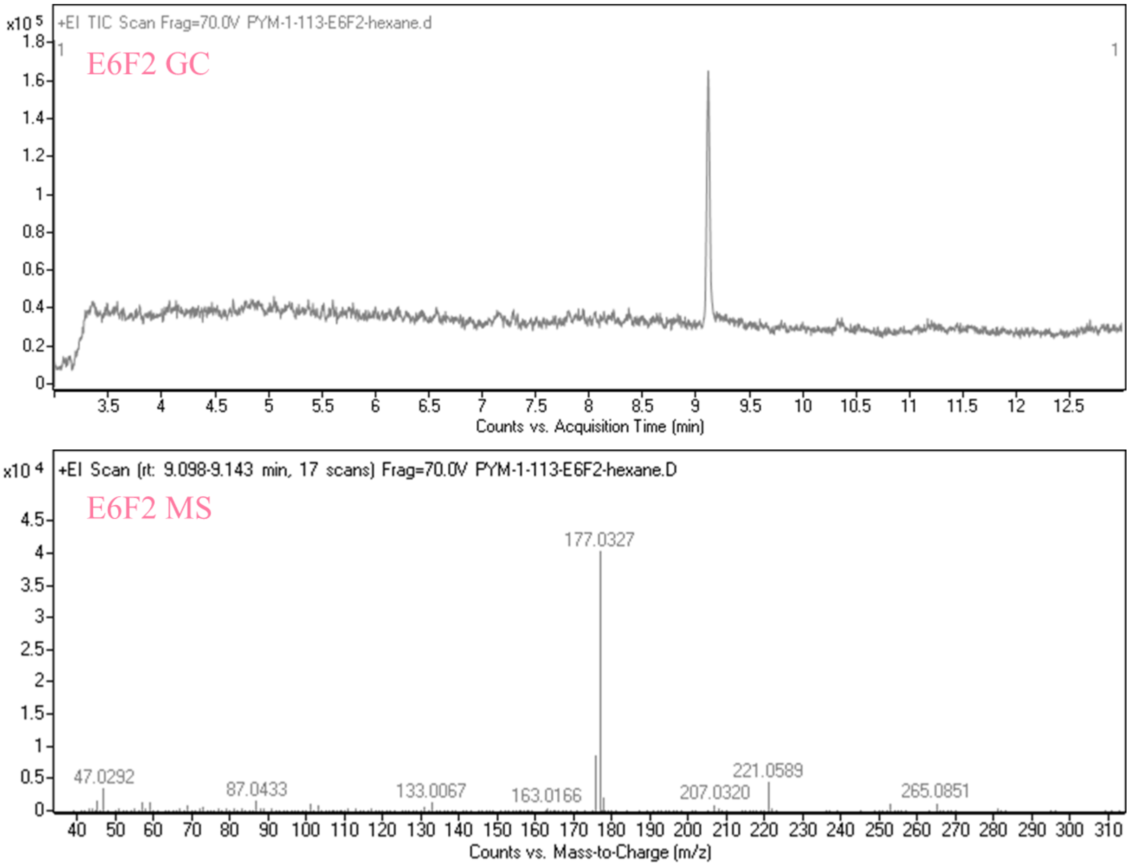

**Figure S4**. Gas chromatograph-mass spectrometry (GC-MS) data of F1 and F2 compounds. High purity is verified by the absence of impurity peak in GC elution curves. In mass spectra, all F1 compounds have a strong peak at 127.04 g/mol while F2 compounds have a strong peak at 177.03 g/mol. The major fragment is assigned as the corresponding oxonium ions as shown in the mass spectra of E3F1 and E3F2.

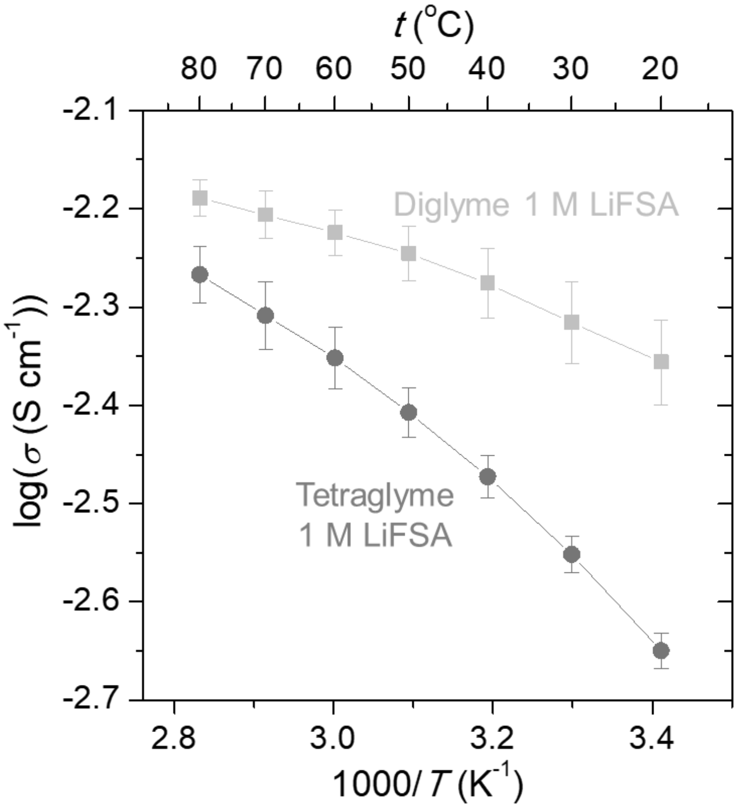

**Figure S5.** Ionic conductivity as a function of temperature of 1 M LiFSA dissolved in diglyme and tetraglyme. The lines are to guide the eyes. Error bars represent standard deviation from the average of at least 3 different cells. The conductivity of 1 M LiFSA in tetraglyme is close to values reported in literatures.[1,2]

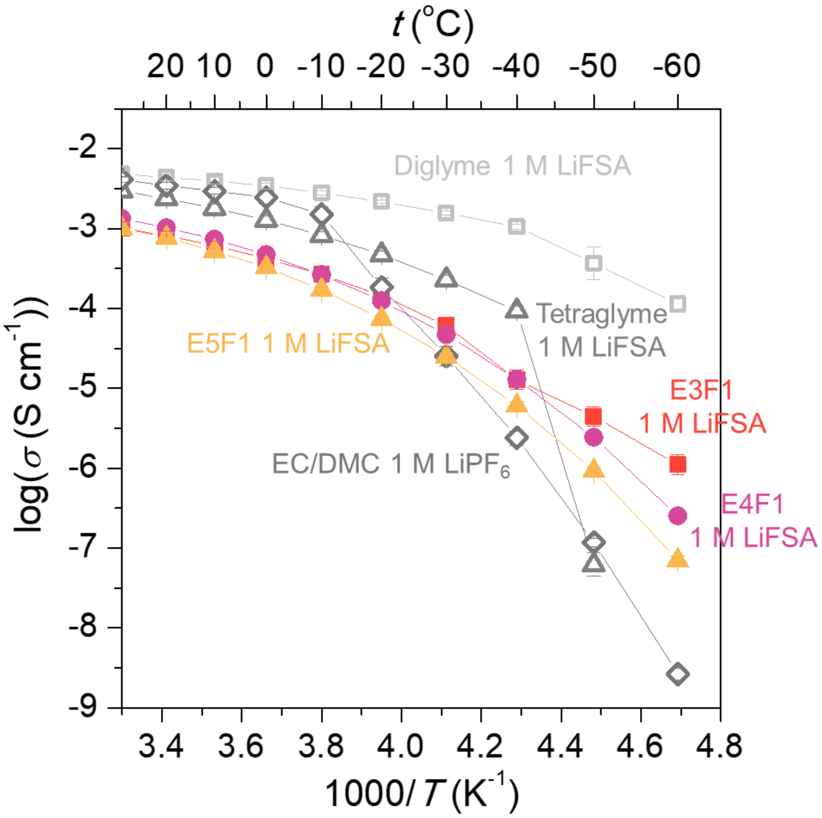

**Figure S6**. Ionic conductivity in low temperature range. The conductivity was measured by electrochemical impedance spectroscopy (EIS) following procedure described in experimental section. For the 1 M LiPF6 in EC/DMC (50:50 v/v) electrolyte, a Whatman separator was used for better wetting. Hence a different cell constant of 1 was used.

Because of crystallization (see DSC data in Figure S12), the conductivity of EC/DMC and tetraglyme electrolytes has sharp turns at –10°C and –40°C, respectively. After this transition, their conductivities drop much faster than the fluoroether electrolytes. At –60°C, E3F1 maintains conductivity above $10^{-3}$ mS cm$^{-1}$, which is two orders of magnitude higher than that of carbonate electrolyte.

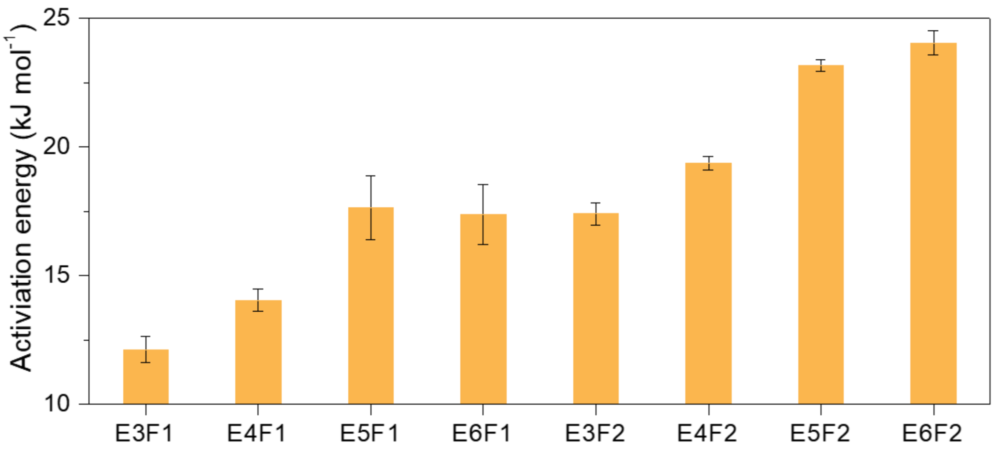

**Figure S7**. Activation energy of 1 M LiFSA electrolytes. The activation energy of ion transport is extracted from linear fitting of conductivity versus temperature plots shown in the main manuscript Figures 2a and 2b.

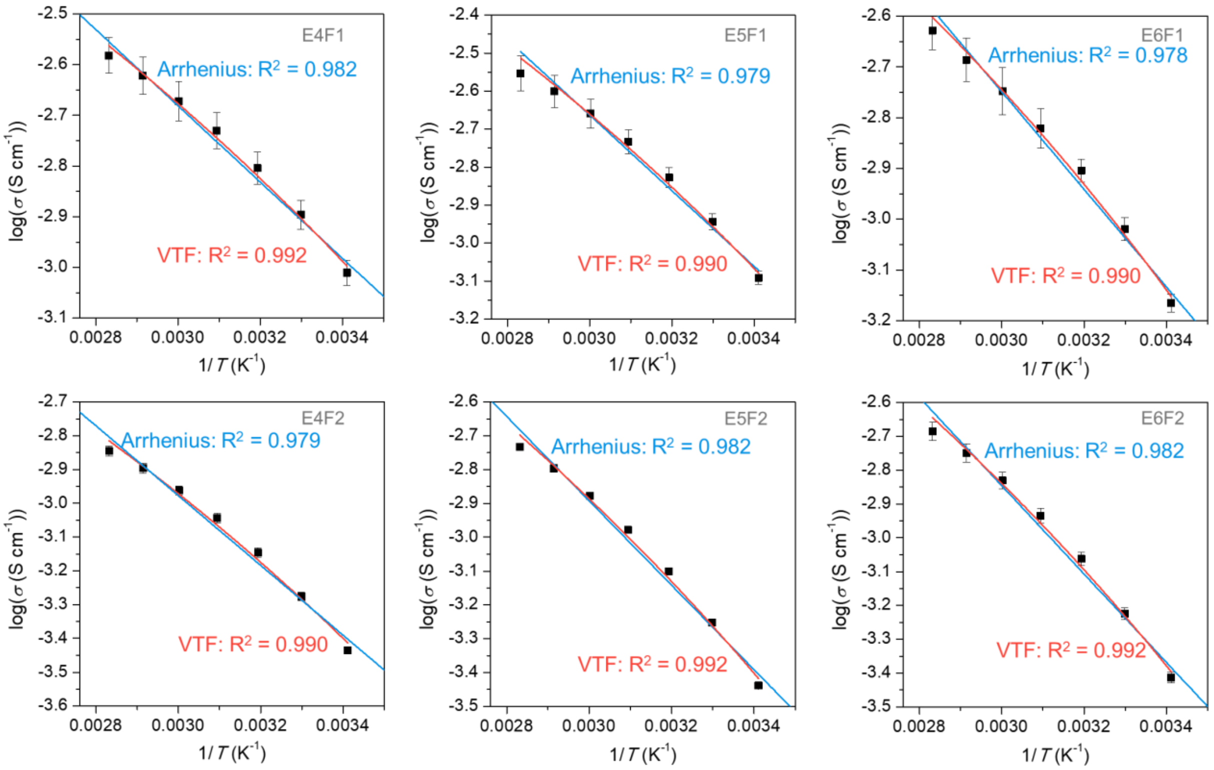

**Figure S8**. Vogel−Tammann−Fulcher (VTF) and Arrhenius fitting of ionic conductivity data. VTF equation can fit slightly better since it accounts the influence of glass transition temperature ($T_g$).

Vogel−Tammann−Fulcher equation: $\sigma = Ae^{\frac{-B}{T-T_o}}$, where $T_o = T_g - 50$.

Arrhenius equation: $\sigma = Ae^{-\frac{E_a}{RT}}$.

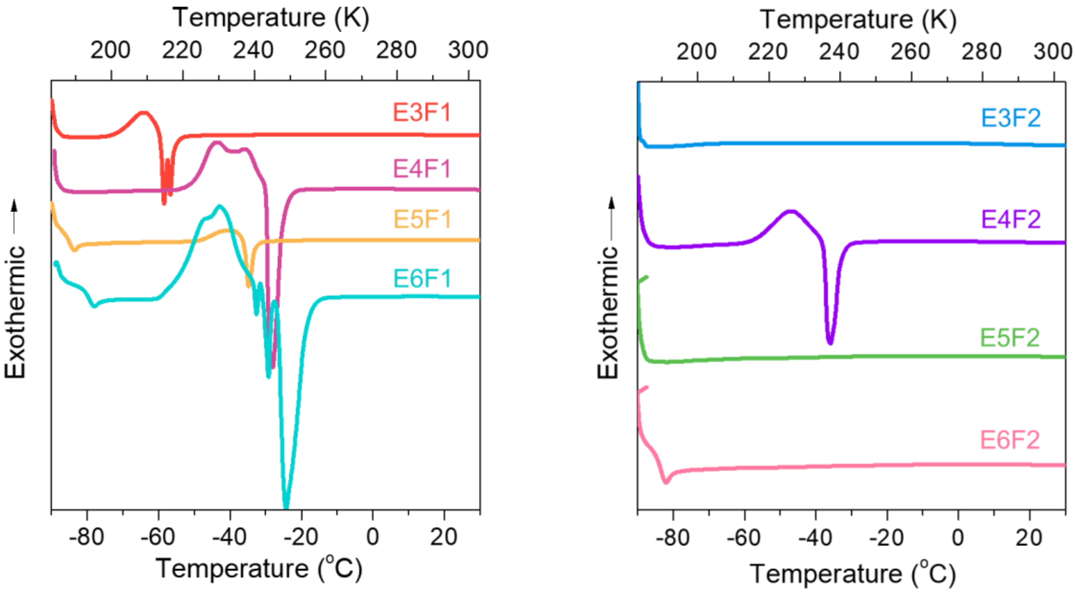

**Figure S9**. Differential scanning calorimetry (DSC) heating traces of pure solvents. All DSC tests were performed at heating or cooling rate of 10°C/min. The sample was first heated up to 80°C, and then looped twice between 80°C and –90°C. The heating traces of second loop are shown here because no transition was observed in cooling of all the F1 and F2 compounds and their LiFSA solutions.

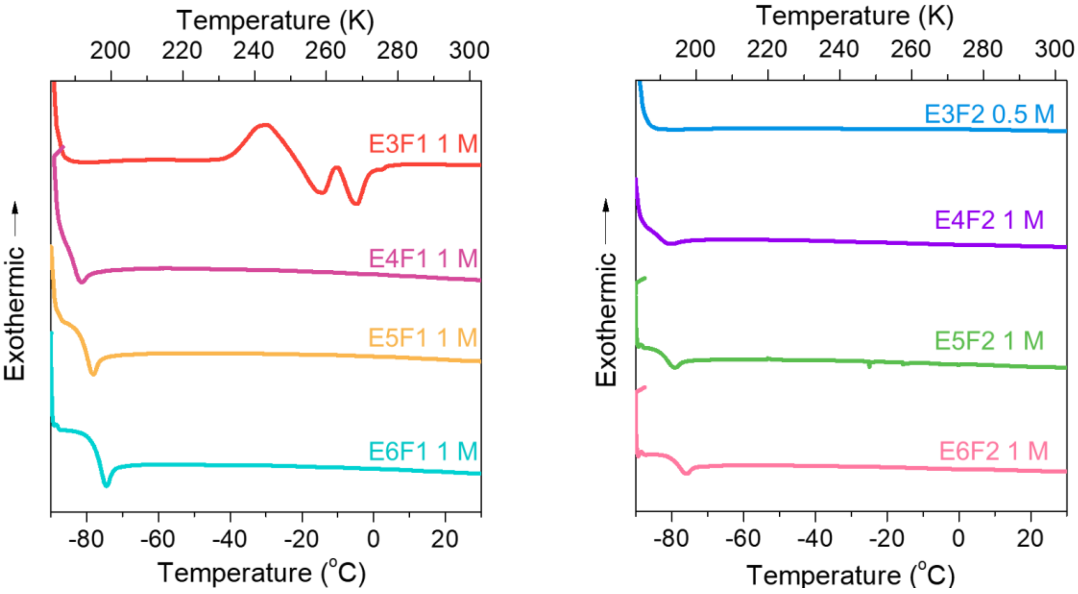

**Figure S10**. DSC heating traces of LiFSA in fluorinated ethers. All DSC tests were performed at heating or cooling rate of 10°C/min. The sample was first heated up to 80°C, and then looped twice between 80°C and –90°C. The heating traces of second loop are shown here because no transition was observed in cooling of all the F1 and F2 compounds and their LiFSA solutions.

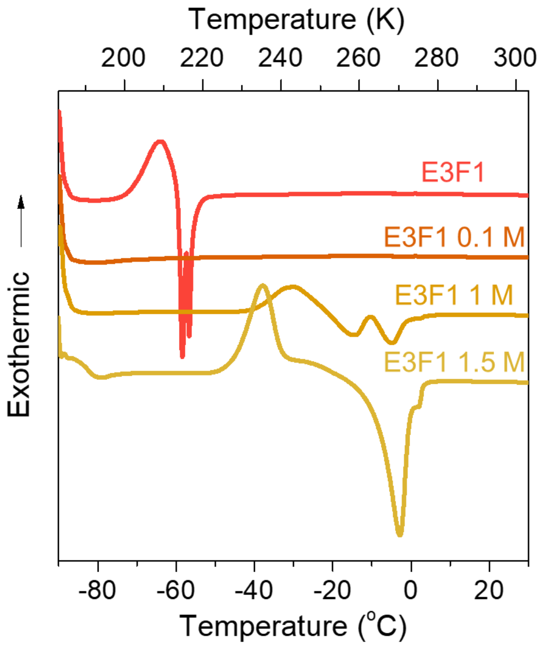

**Figure S11**. DSC of E3F1 and its LiFSA solutions. All DSC tests were performed at heating or cooling rate of 10°C/min. The sample was first heated up to 80°C, and then looped twice between 80°C and –90°C. The heating traces of second loop are shown here.

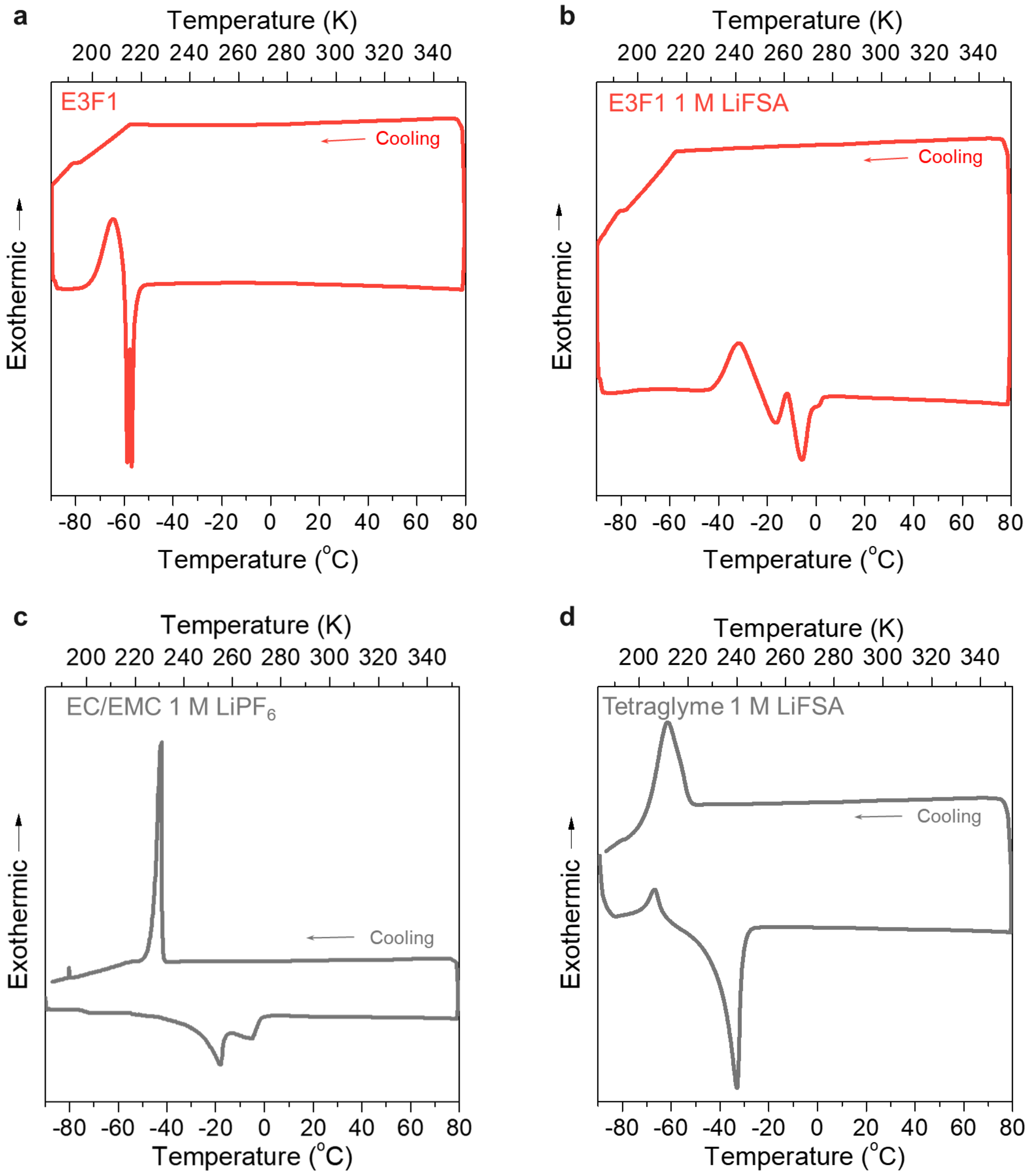

**Figure S12**. The second loop of DSC data for (**a**) E3F1, (**b**) 1 M LiFSA in E3F1, (**c**) commercially used carbonate electrolyte and (**d**) 1 M LiFSA in tetraglyme. In the second loop starting at 80°C, no transition was observed in cooling of all the pure F1 and F2 compounds and their LiFSA solutions under investigation. Here only E3F1 and its 1 M LiFSA solution are shown as examples. In contrast, the commercial carbonate electrolyte and 1 M LiFSA in tetraglyme electrolyte has strong crystallization peaks in the cooling trace, indicating their tendency to crystalize at low temperature. The differences in DSC shown here correlates to the low temperature conductivity data shown in Figure S6.

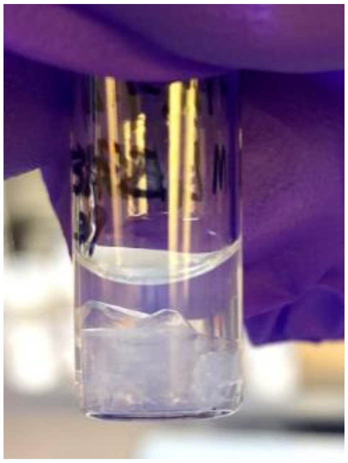

**Figure S13**. Digital photo of the 1 M LiFSA in E3F2 solution that crystallized at room temperature. Photo was taken using an Apple iPhone SE smartphone.

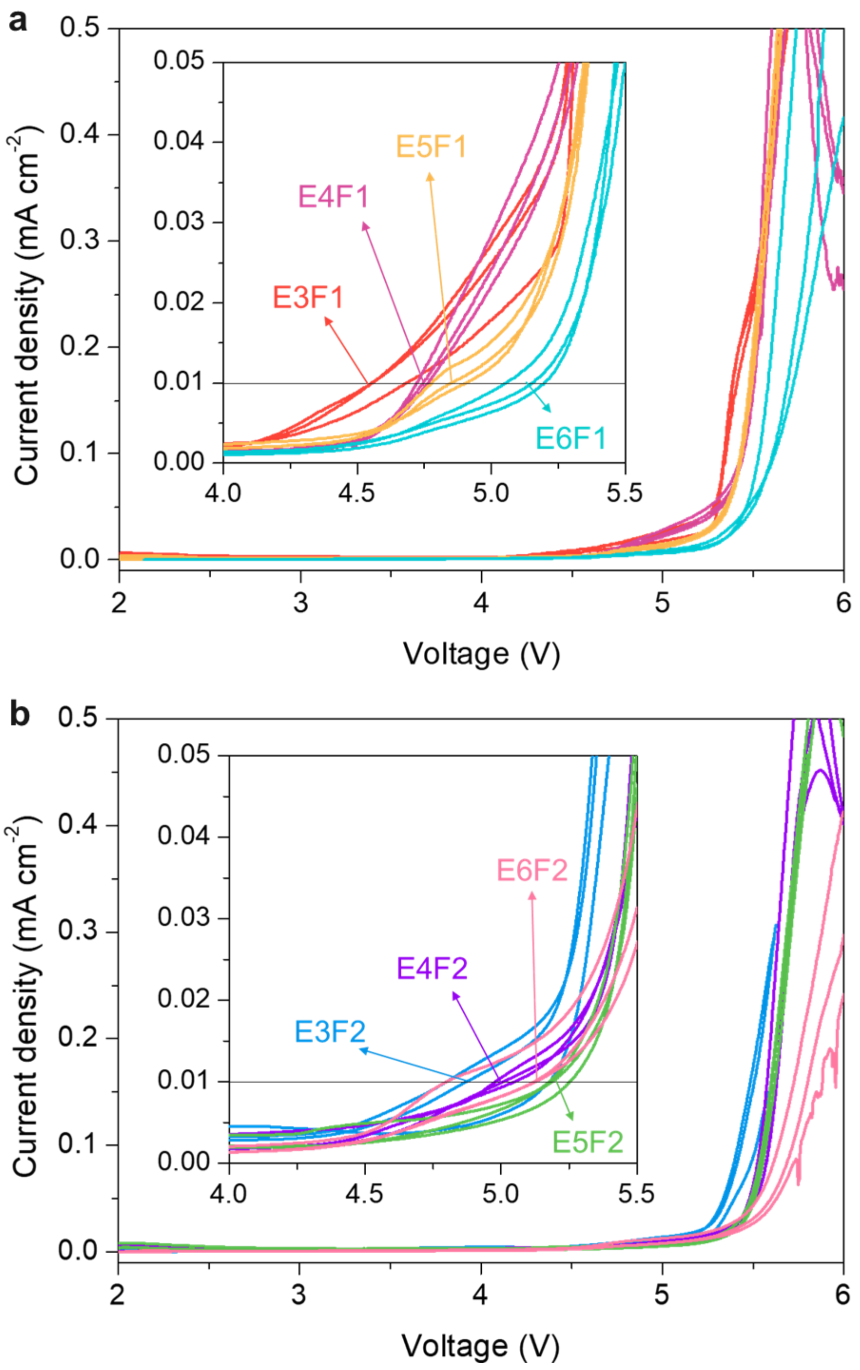

**Figure S14**. Linear sweep voltammetry (LSV) of 1 M LiFSA in (**a**) F1 and (**b**) F2 compounds using stainless steel as working electrode and lithium metal as the counter and reference. Three parallel experiments of each electrolyte are shown here for reproducibility. Each line represents a different coin cell.

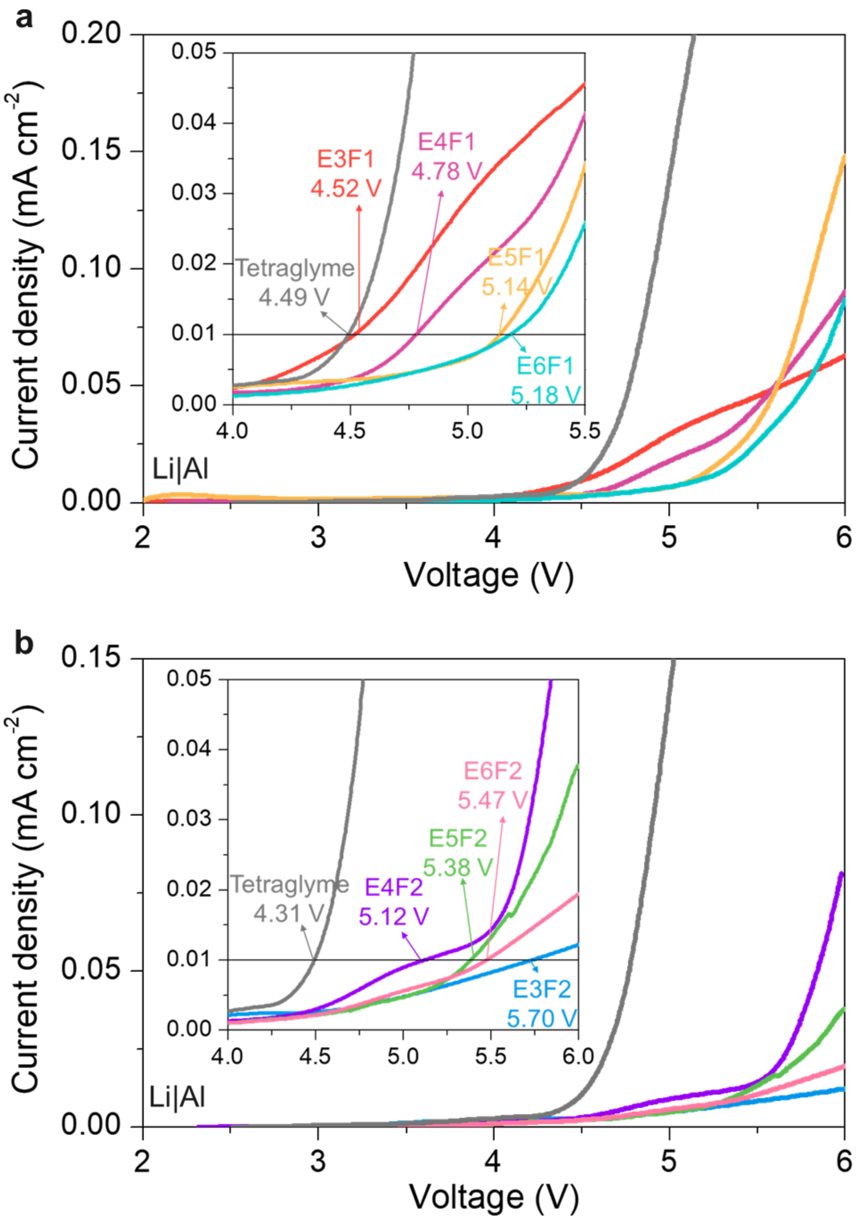

**Figure S15**. Linear sweep voltammetry (LSV) of 1 M LiFSA in F1 and F2 compounds with tetraglyme as control using aluminum as working electrode. The oxidative stability with Al working electrode follows the same trend as with SS electrode except for E3F2. The unexpected low current density of 1 M LiFSA in E3F2 is very likely due to crystallization (as shown in the digital photo in Figure S13).

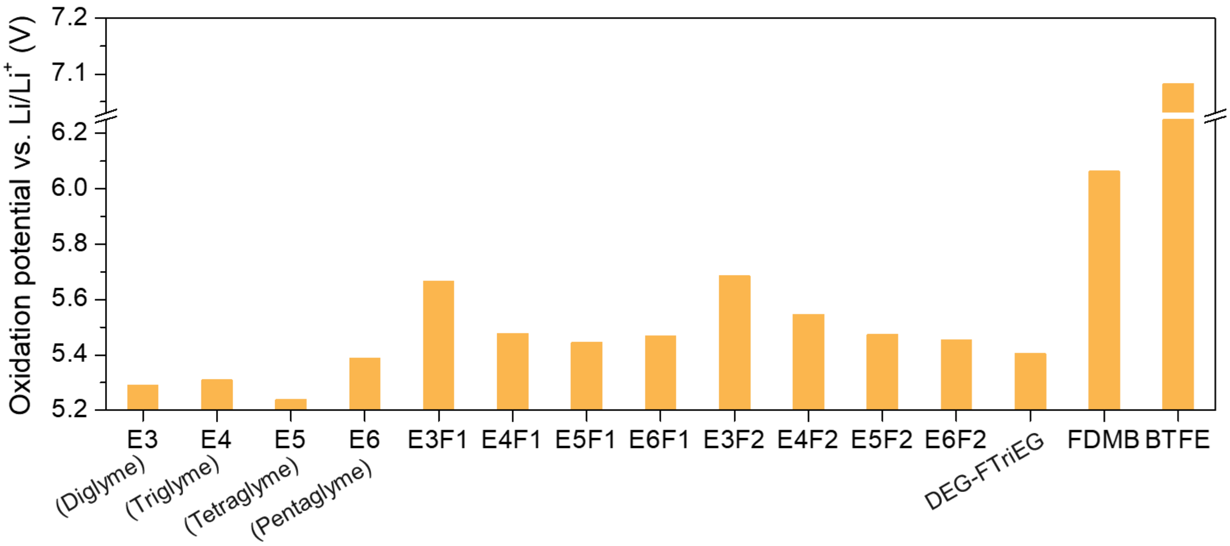

**Figure S16**. Adiabatic oxidation potential calculated by DFT. As a measure of oxidative stability, the oxidation potential data shows that fluoroether compounds have overall improved oxidative stability compared to traditional ethers (E3 to E6). In addition, oxidation potential decreases with increasing ether length in the F1 and F2 compounds, which agrees with intuition but contradicts the experimental oxidative stability trend as described in the main manuscript. DEG-FTriEG molecular structure can be found in Amanchukwu et al.[2] FDMB refers to fluorinated 1,4-dimethoxylbutane from Yu et al.[3] BTFE refers to Bis(2,2,2-trifluoroethyl) ether.

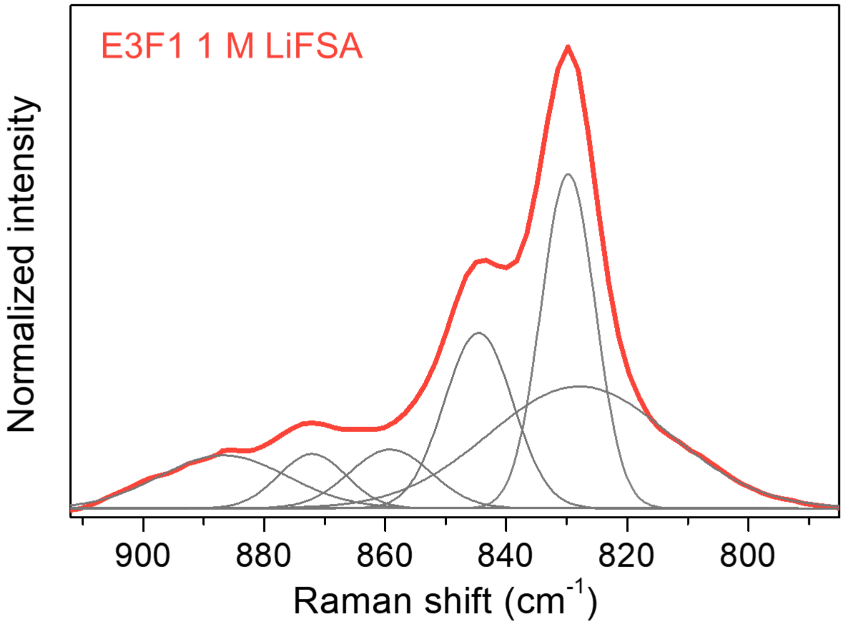

**Figure S17**. Raman spectra of 1 M LiFSA in E3F1. Six components were used to fit the range between 770 and 930 cm$^{-1}$. Fitting was done with Origin Pro 8.5 software.

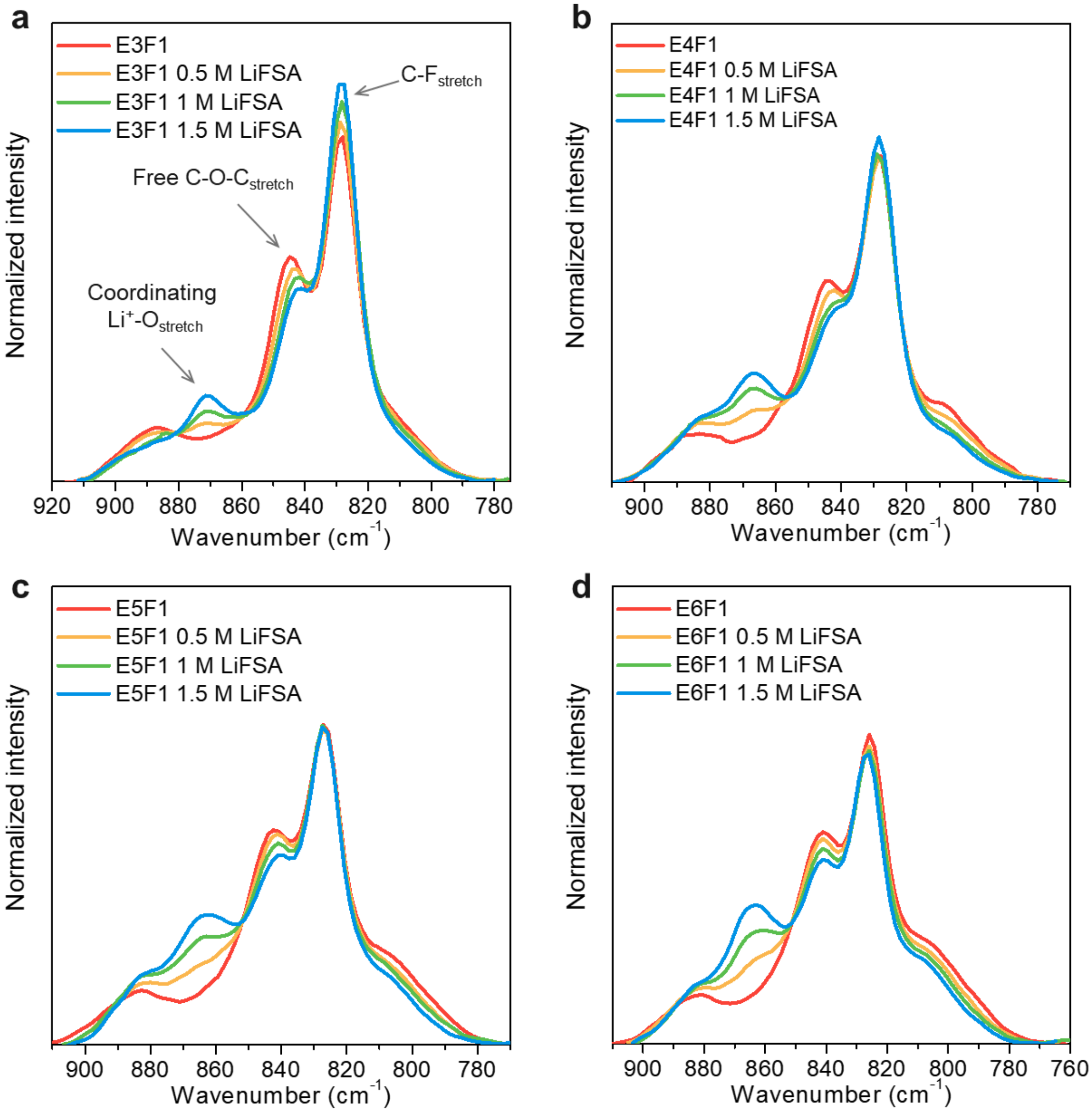

**Figure S18**. The variation of Raman spectra with LiFSA concentration in (**a**) E3F1, (**b**) E4F1, (**c**) E5F1 and (**d**) E6F1. The Raman spectra were normalized by their total area and aligned according to the C–F stretching peak (~ 828 cm$^{-1}$). As the LiFSA salt concentration increases from 0 to 1.5 M, the free C–O–C stretching peak around 843 cm$^{-1}$ shrink significantly while the Li$^+$–O breathing peak around 867 cm$^{-1}$ increases. The vibration modes indicated in E3F1 correspond to the same functional groups in E4F1, E5F1, and E6F1.

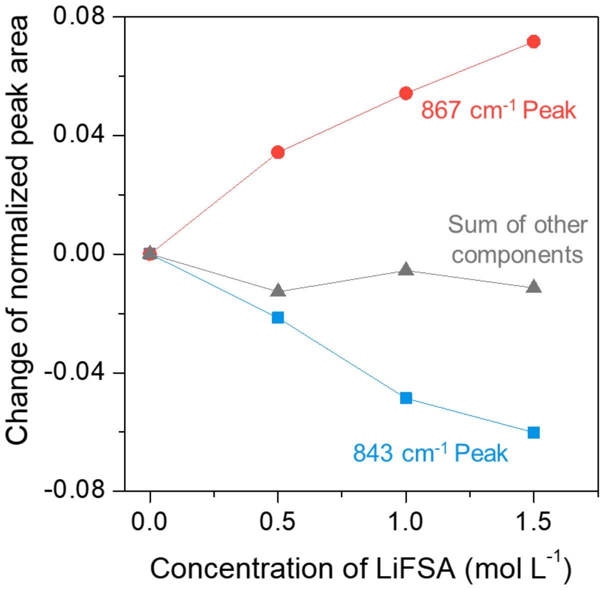

**Figure S19**. The evolution of Raman peak area with LiFSA concentration in E3F1. The peak area of every component shown in Figure S17 was first normalized to the total area and then subtracted by the normalized area value of pure E3F1 to calculate the change in normalized peak area. As shown here, the normalized peak area of 867 cm$^{-1}$ and 843 cm$^{-1}$ component varies significantly with salt concentration while the sum of others is almost constant.

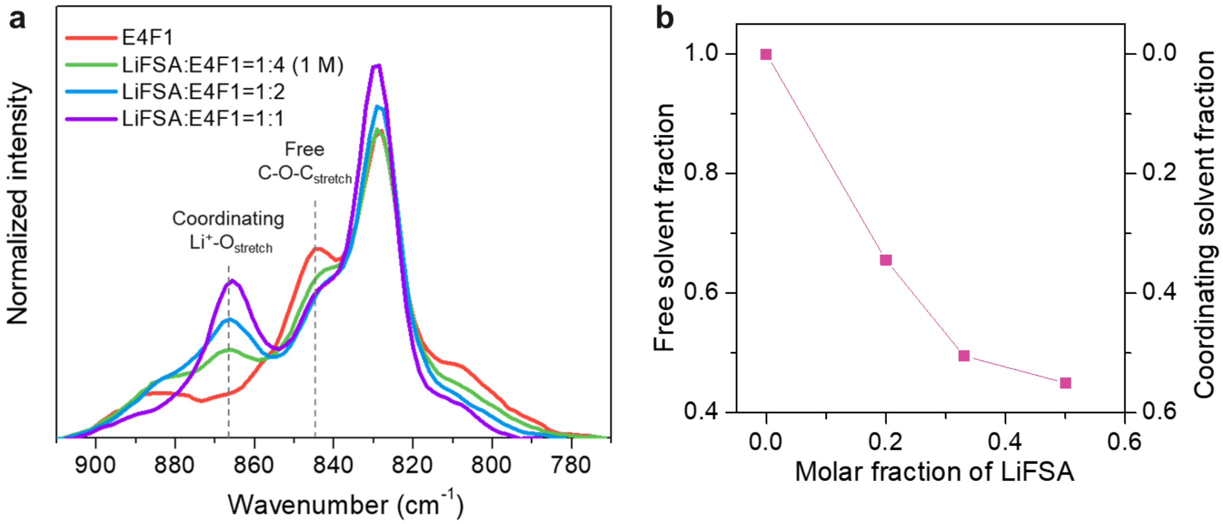

**Figure S20**. (**a**) The variation of Raman spectra with E4F1/LiFSA molar ratio. (**b**) The fraction of free and coordinating solvent as a function of LiFSA molar fraction. When the molar fraction of salt increase from 0 to 0.5 (pure E4F1 to LiFSA:E4F1 = 1:1), more solvent molecules participate in coordination, giving rise to lower free solvent fraction.

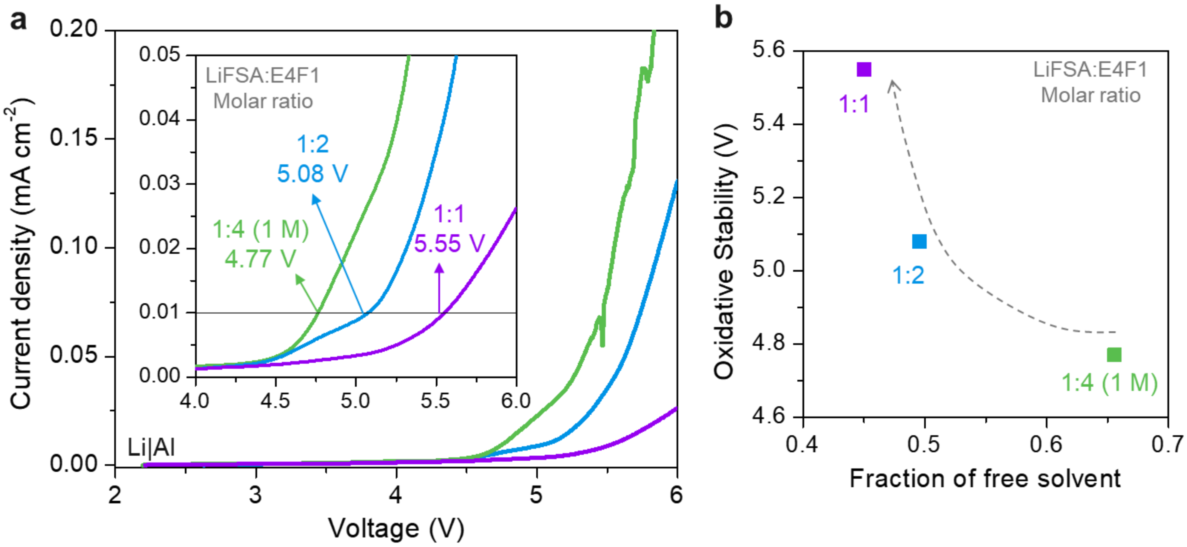

**Figure S21**. (**a**) The linear sweep voltammetry (LSV) of LiFSA/E4F1 solution in different molar ratios. (**b**) Oxidative stability of LiFSA/E4F1 electrolytes as a function of free solvent fraction. When the molar ratio LiFSA:E4F1 increases from 1:4 to 1:1, more solvent molecules participate in ion solvation and oxidative stability is enhanced by reduced free solvent fraction.

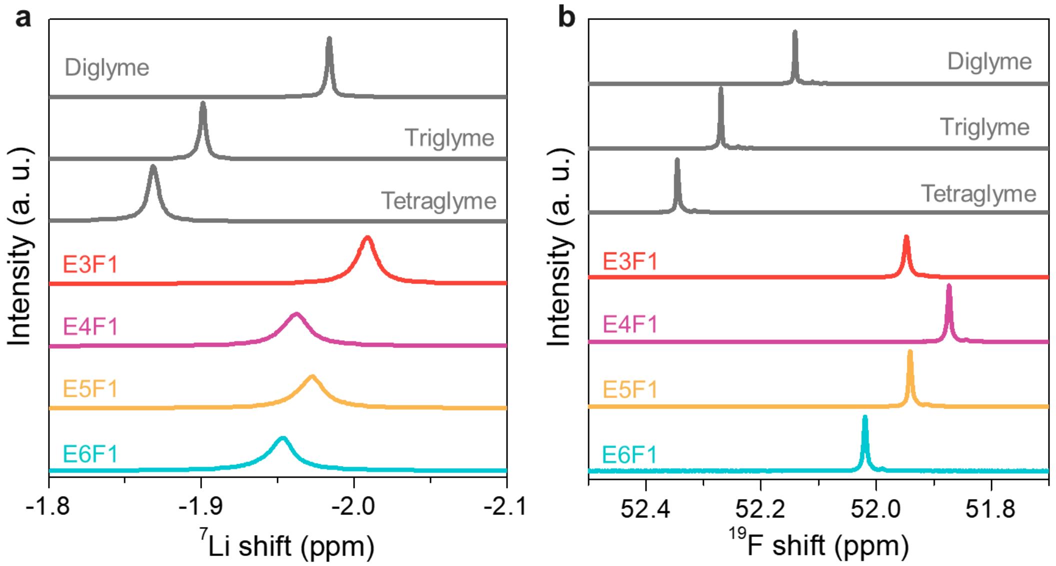

**Figure S22**. (**a**) $^7$Li and (**b**) $^{19}$F NMR shifts of 1 M LiFSA in F1 compounds and glymes as controls. $^7$Li shift was referenced to 0.1 M $LiClO_4$ in $CD_3CN$ (–2.80 ppm)[4] while $^{19}$F shift was referenced to trifluorotoluene (-62.5 ppm)[5]. The peaks of $Li^+$ and $FSA^-$ both overall shift to higher field with decreasing molecular size from tetraglyme to diglyme or from E6F1 to E4F1 except for E3F1. In $^7$Li NMR, E3F1 has an additional upfield shift of around 0.05 ppm from the other F1 electrolytes. In $^{19}$F NMR, E3F1 shifts to lower field from E4F1 as opposite to the trend. The distinct behavior of E3F1 can be explained by intensive ion pairing.

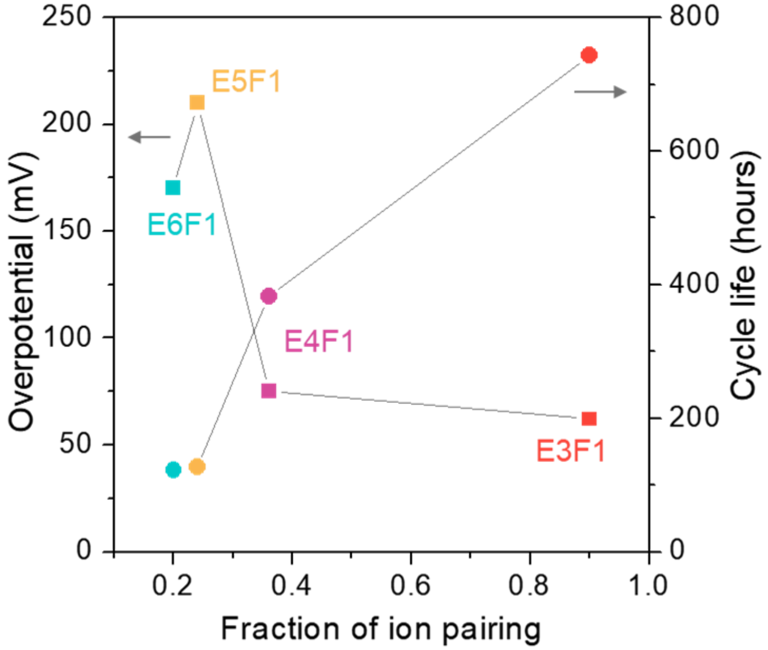

**Figure S23**. Summary of the Li/Li symmetric cells cycling results using 1 M LiFSA in F1 compounds as electrolytes. As the length of the fluorinated ether decreases from E6F1 to E3F1, weaker ion solvation (indicated by higher fraction of ion pairing) leads to lower overpotential and longer cycle life. The fraction of ion pairing was quantified from the fitting of FSA peak shown in Figure 4a: Fraction of ion pairing = (Area of AGG + Area of CIP)/Total area.

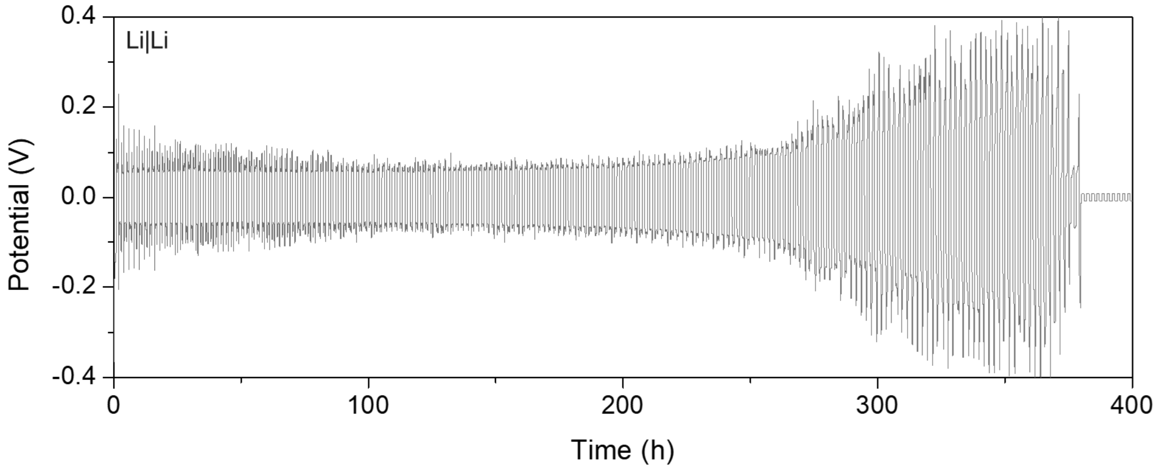

**Figure S24**. The voltage versus time plot of Li/Li symmetric cells using 1 M $LiPF_6$ in EC/DMC=50/50 (v/v). Celgard 3501 separator was used to replace Celgard 2325 for better wetting. The cells were cycled at a current density of 1 mA $cm^{-2}$ to 1 mA h $cm^{-2}$ after five formation cycles at 0.02 mA $cm^{-2}$ to 0.1 mA h $cm^{-2}$.

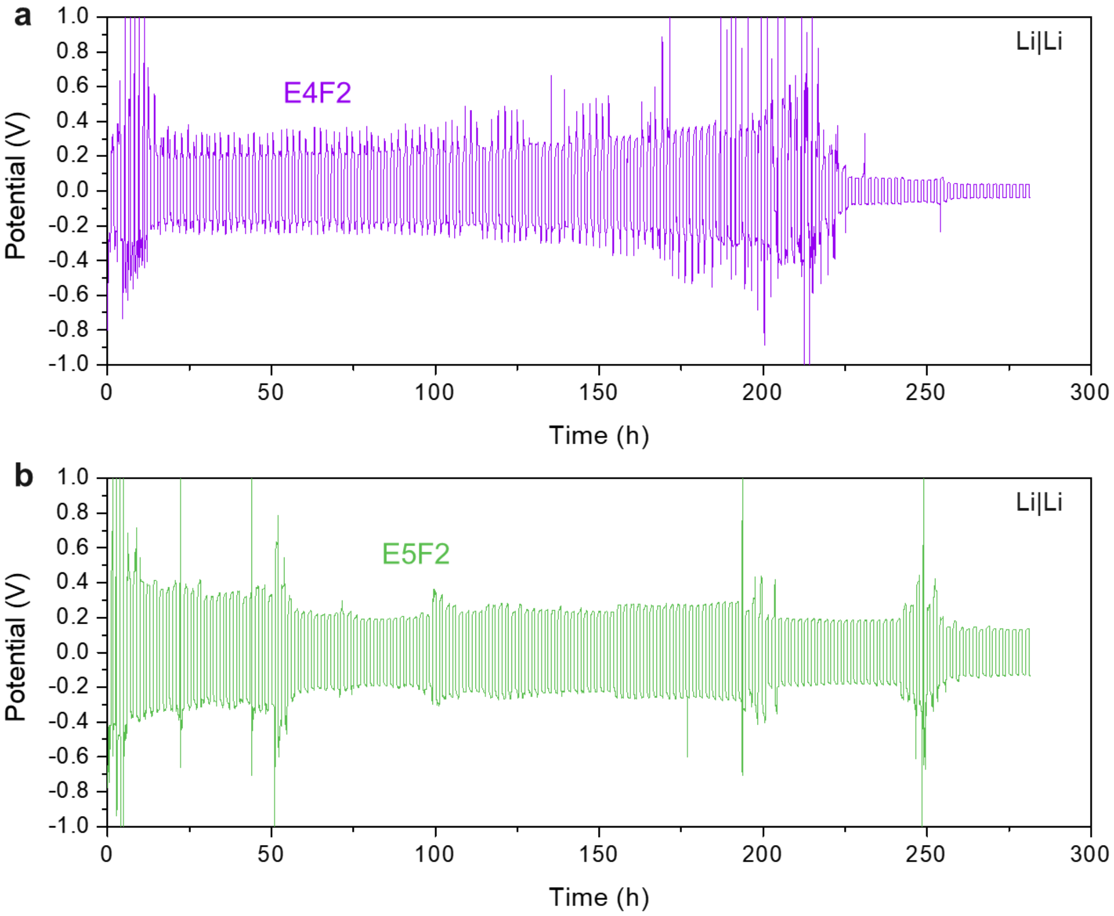

**Figure S25**. Voltage versus time plot of Li/Li symmetric cells using 1 M LiFSA in (**a**) E4F2 and (**b**) E5F2 as electrolytes. Cells were cycled at a current density of 1 mA cm$^{-2}$ to 1 mA h cm$^{-2}$ after five formation cycles at 0.02 mA cm$^{-2}$ to 0.1 mA h cm$^{-2}$. The poor performance of E4F2 and E5F2 could be attributed to their inferior ionic conductivities.

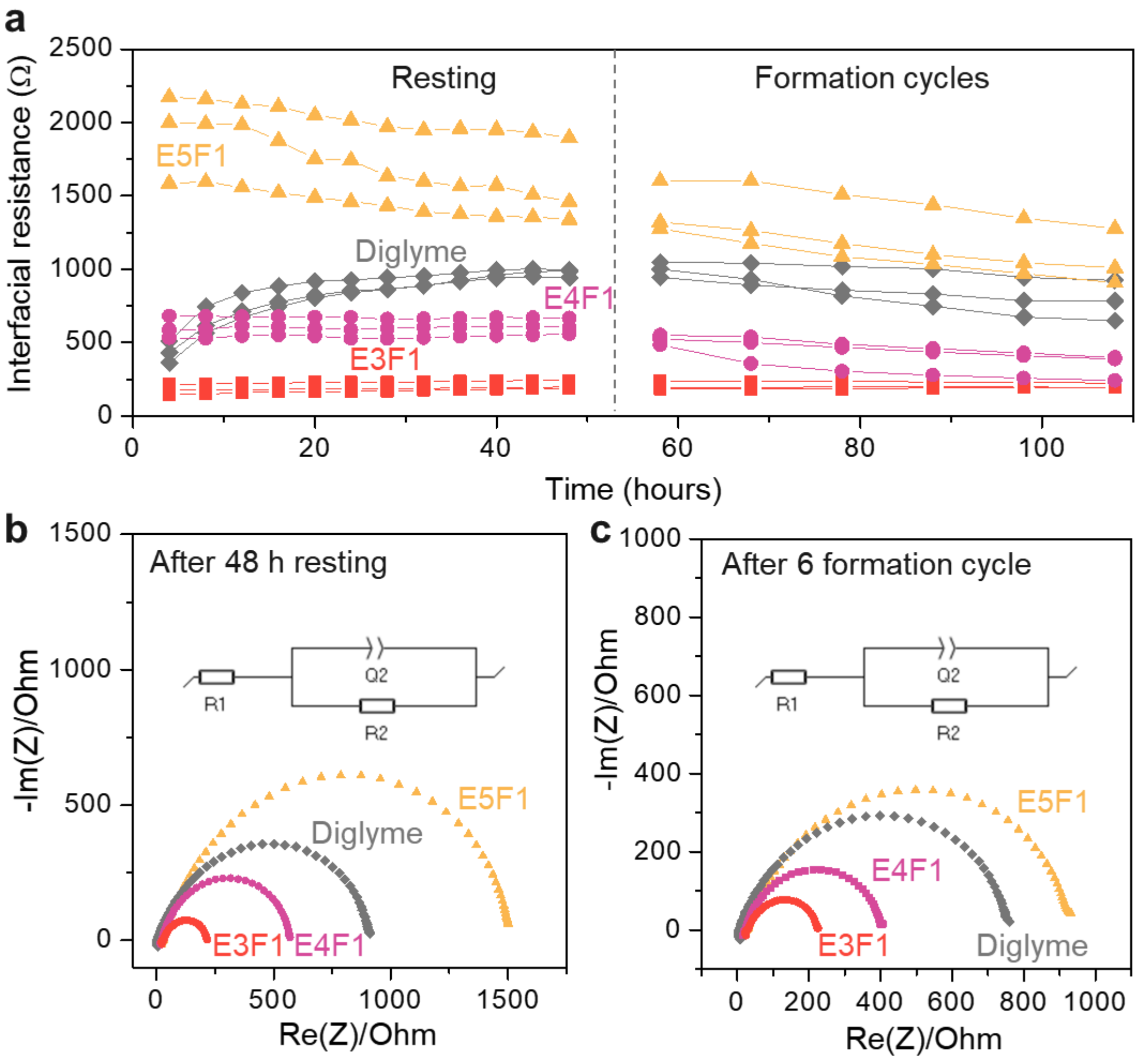

**Figure S26**. (**a**) The interfacial resistance of Li/Li symmetric cells using 1 M LiFSA in F1 compounds and diglyme as electrolytes obtained using EIS. Each line represents a different Li/Li cell. The Nyquist plot of electrochemical impedance spectra (**b**) after 48 hours resting and (**c**) after 6 formation cycles. Insets in (b) and (c): Equivalent circuit used for fitting. The value of R2 was taken as interfacial resistance. Fitting parameters of the E3F1 cell are shown below as an example.

| | **R1 (Ω)** | **R2 (Ω)** | **Q2 ($\mathrm{F \cdot s^{(a-1)}}$)** | **a2** |
|---|---|---|---|---|
| E3F1 after 48 h resting | 31.49 | 196.5 | 7.939e-6 | 0.8269 |
| E3F1 after 6 formation cycle | 30.54 | 192.7 | 8.004e-6 | 0.823 |

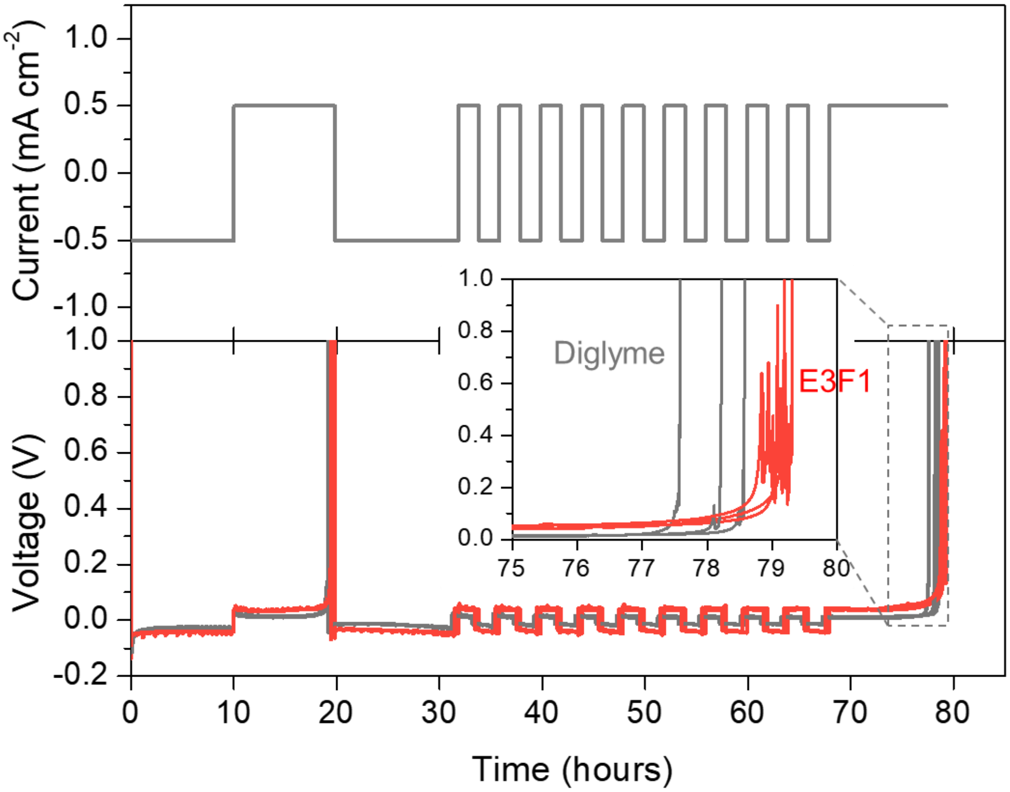

**Figure S27**. Coulombic efficiency (CE) measurements in Li/Cu cells using Aurbach protocol[6] at a current density of 0.5 mA/cm$^2$. Inset: zoom-in view of the last stripping. 1 M LiFSA in E3F1 electrolyte has higher average CE than diglyme (98.9% vs 95.7%). CE data of each individual cell are shown below.

| | **Cell 1 (%)** | **Cell 2 (%)** | **Cell 3 (%)** | **Average CE (%)** |
|---|---|---|---|---|
| **E3F1** | 98.1 | 98.9 | 99.6 | 98.9 |
| **Diglyme** | 94.5 | 96.3 | 96.3 | 95.7 |

In this protocol, cells were first precycled by depositing lithium on copper electrode for 10 hours and then stripping to 1 V (the initial ~20 hours of the traces). Then, a ten-hour deposition was made (at 0.5 mA/cm$^2$). Then, 10 deposition and stripping cycles at 0.5 mA/cm$^2$ to 1 mA h/cm$^2$ was performed. Finally, lithium was stripped from copper electrode until voltage reaches 1 V. CE was calculated following the equation below:

$$CE = \frac{Total\ stripping\ capacity}{Total\ depositing\ capacity} = \frac{Capcity\ of\ the\ final\ stripping + 10\ mA\ h/cm^2(10\ cycles)}{5\ mA\ h/cm^2(intial\ deposition) + 10\ mA\ h/cm^2(10\ cycles)}$$

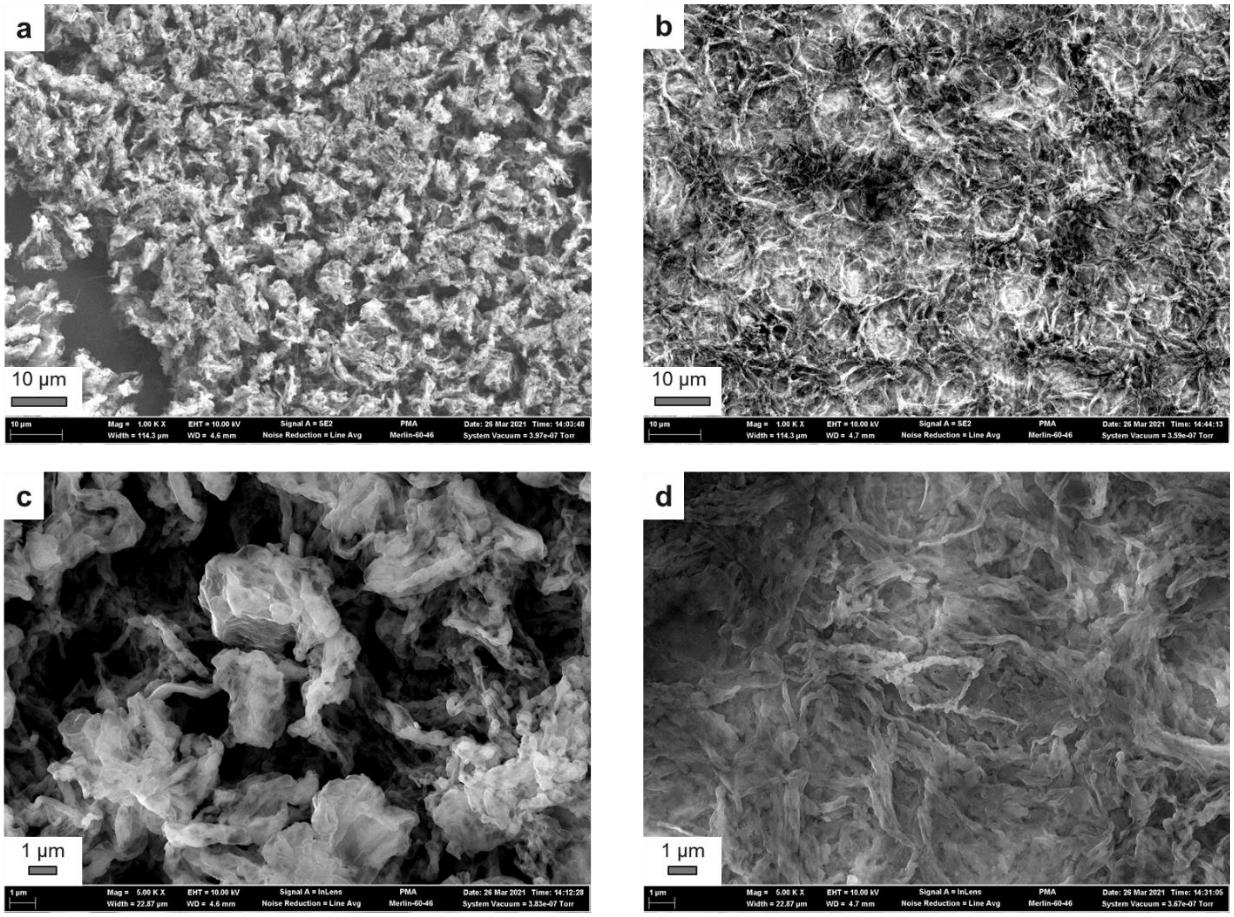

**Figure S28**. Scanning electron microscopy (SEM) images of residual lithium on copper electrode after one lithium deposition/stripping cycle using 1 M LiFSA in (**a**, **c**) diglyme and (**b**, **d**) E3F1. A smooth layer of dead lithium is observed in E3F1 while the morphology in diglyme is marked by strong contrast in height. The smoother morphology in E3F1 indicates less dead lithium formation, which agrees with the higher Coulombic efficiency observed on E3F1. To prepare the lithium sample, lithium was first deposited on copper electrode at a current rate of 1 mA/cm$^2$ to 1 mA h/cm$^2$ capacity and then stripped to a cut off voltage of 1 V.

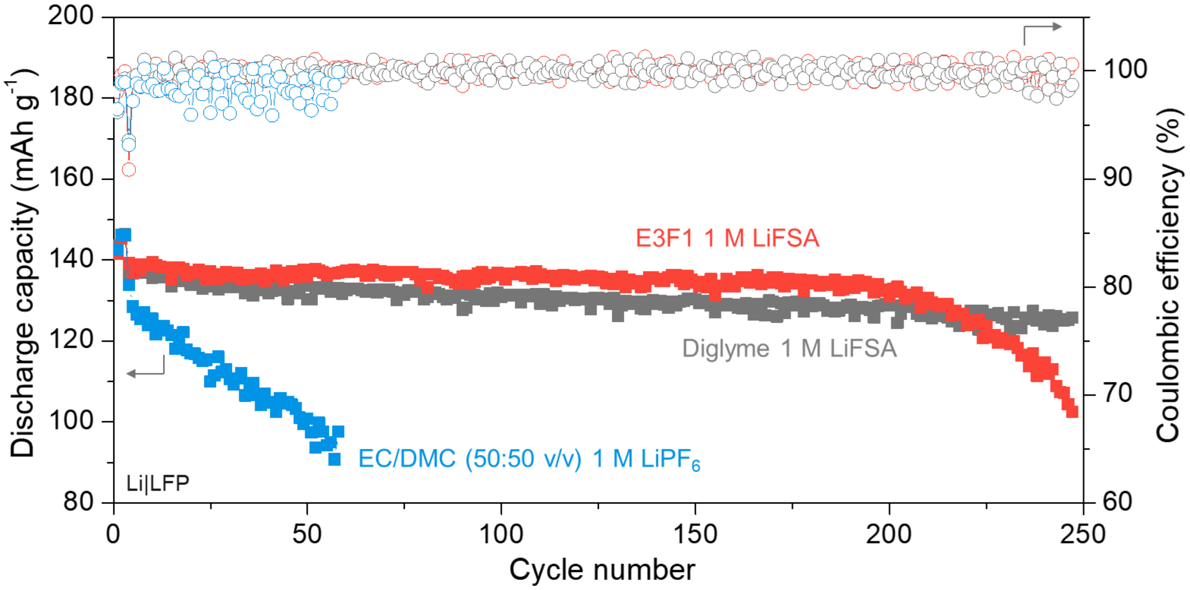

**Figure S29**. Galvanostatic cycling of Li/LFP cells at a current rate of C/3. Both diglyme and E3F1 maintain almost 100% Coulombic efficiency and stable discharge capacity for more than 200 cycles while the capacity of commercial carbonate electrolyte decays constantly. The cells were cycled between 2.9 V and 3.8 V at C/3 current density after three formation cycles at C/20.

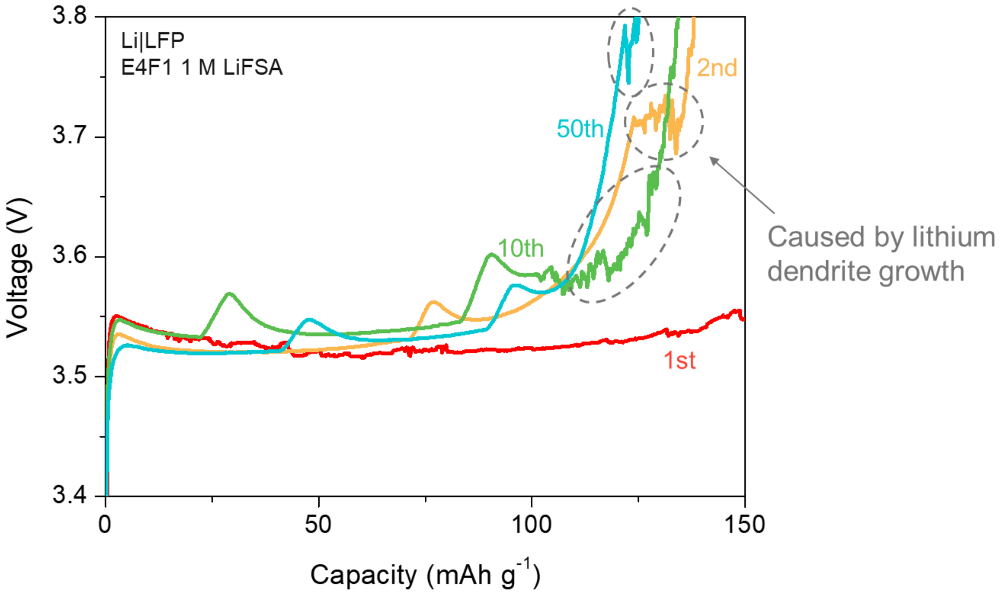

**Figure S30**. Charging profile of Li/LFP cell using 1 M LiFSA in E4F1 as electrolytes. The cell was cycled between 2.9 V and 3.8 V at C/3 current density after three formation cycles at C/20. The representative cycles shown here all have noisy voltage response, which has been reported as caused by lithium dendrite growth.[7]

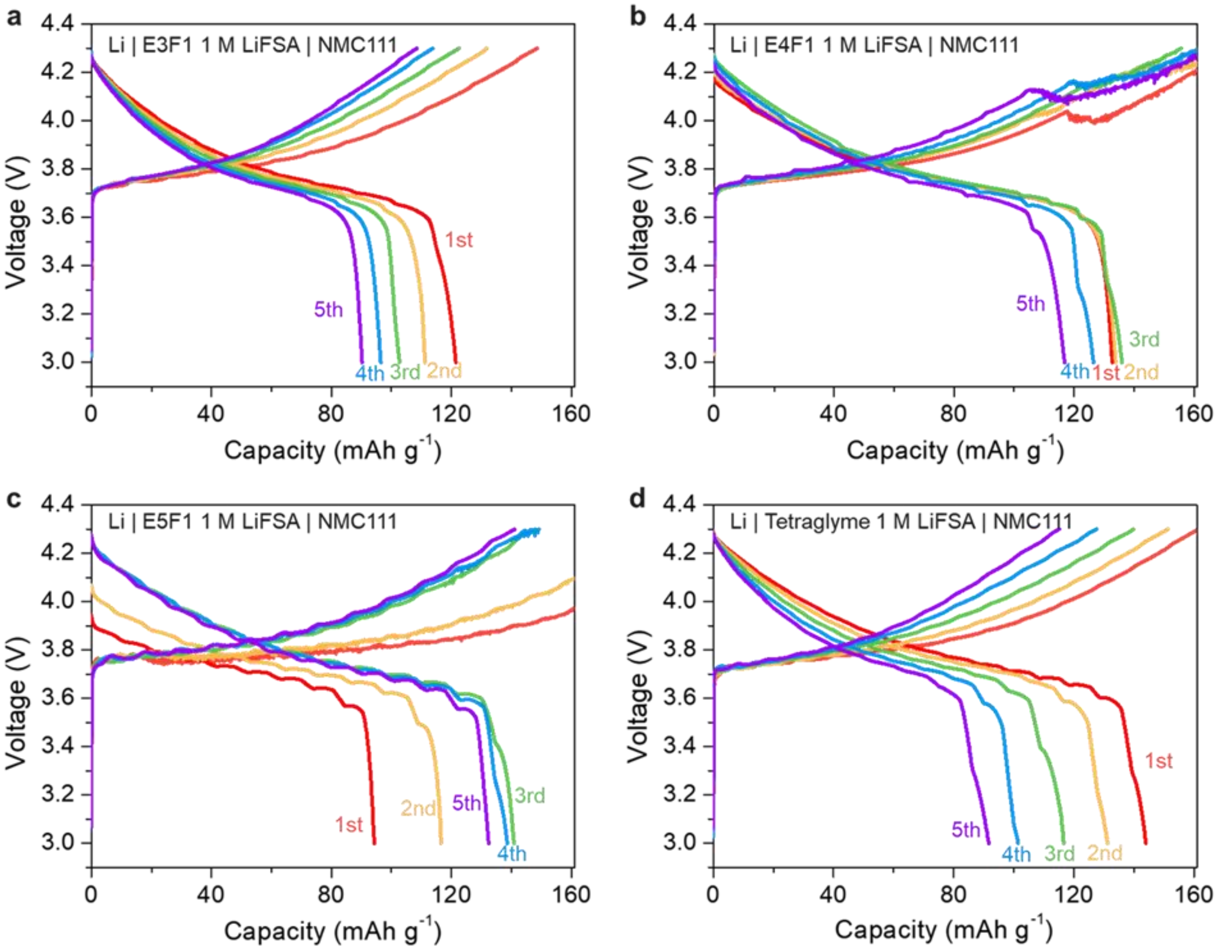

**Figure S31**. Galvanostatic cycling of Li/NMC111 cells at current rate of C/10 using 1 M LiFSA in (**a**) E3F1, (**b**) E4F1, (**c**) E5F1 and (**d**) tetraglyme as electrolytes. E4F1 and E5F1 cells are able to retain around 120 mA h/g discharge capacity in five cycles whereas the capacity of E3F1 and tetraglyme decay to 90 mA h/g at the fifth cycle. The better performance of E4F1 and E5F1 with 4.3 V class NMC 111 electrode reflects their higher oxidative stability compared to E3F1 and tetraglyme. However, noisy voltage response observed in E4F1 and E5F1 indicates lithium dendrites may still grow[7], which leads to unsatisfactory Coulombic efficiency. Li/NMC 111 cells were cycled between 3−4.3 V. Three formation cycles at C/30 were performed prior to the test.

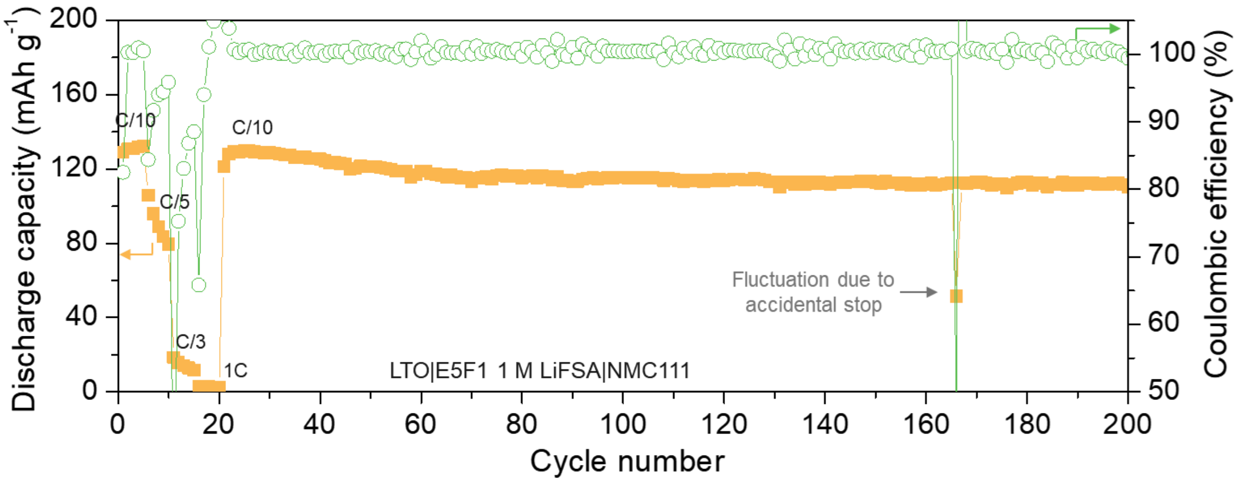

**Figure S32**. Galvanostatic cycling of LTO/NMC111 cells at current rates between C/10 and 1C using 1 M LiFSA in E5F1 electrolyte. At a slow rate of C/10, E5F1 electrolyte can be cycled repeatedly for more than 200 times with ~ 86% capacity retention. The fluctuation marked around 166th cycle was due to an accidental stop of the test.

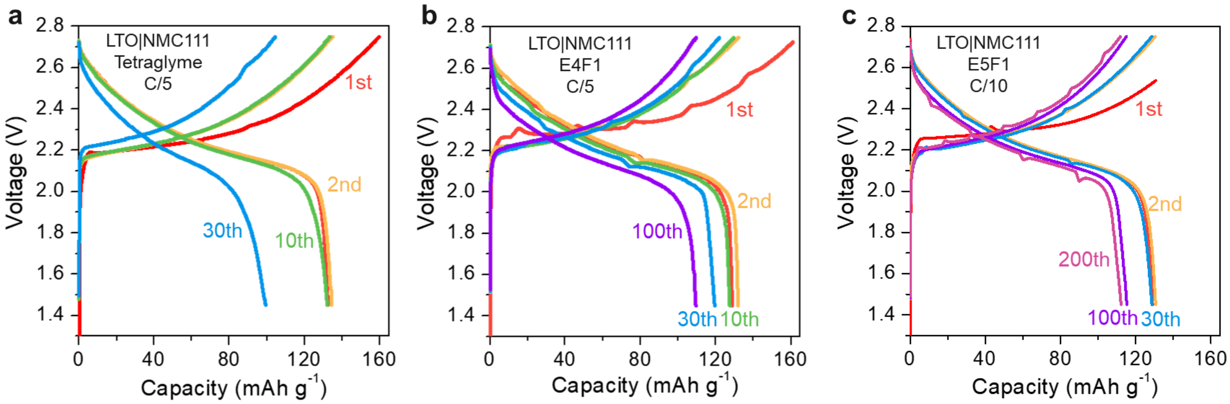

**Figure S33**. Galvanostatic cycling of LTO/NMC111 cells using (**a**) 1 M LiFSA in tetraglyme electrolyte, (**b**) 1 M LiFSA in E4F1 electrolyte, and (**c**) 1 M LiFSA in E5F1 electrolyte. Tetraglyme and E4F1 cells were cycled at a constant current rate of C/5 while the E5F1 cell was cycled mostly at C/10 (cycling program shown in Figure S32). In the initial two cycles, they all have discharge capacity around 130 mA h g$^{-1}$. Afterward, E4F1 cell and E5F1 cell maintain discharge capacity of ~110 mA h g$^{-1}$ (> 80%) at 100th cycle and 200th cycle, respectively. In contrast, the capacity of tetraglyme cell drops below 90 mA h g$^{-1}$ at the 30th cycle. The better performance of E4F1 and E5F1 with 4.3 V class NMC 111 cathode reflects the improvement in oxidative stability. The fact that E4F1 and E5F1 electrolytes produce smooth voltage profiles in LTO/NMC 111 cells verified the effects of lithium dendrite growth on Li/NMC 111 cells.

**Table S1**. Summary of yield and physical properties

| Compound name | Yield (%) | Boiling point at 2 kPa (℃) | Density (g cm$^{-3}$) |
|---|---|---|---|
| E3F1 | 75 | 55 | 1.28 |
| E4F1 | 60 | 90 | 1.25 |
| E5F1 | 63 | 95 | 1.24 |
| E6F1 | 66 | - | 1.21 |
| E3F2 | 80 | 70 | 1.37 |
| E4F2 | 72 | - | 1.34 |
| E5F2 | 59 | - | 1.31 |
| E6F2 | 65 | - | 1.29 |

**Table S2**. Summary of DSC data.

| Sample | $T_g$ (°C) | $T_c$ (°C) | $T_m$ (°C) | $\Delta H_c$ (J g$^{-1}$) | $\Delta H_m$ (J g$^{-1}$) |
|---|---|---|---|---|---|
| E3F1 | - | -64.4 | -56.7 (-58.4) | 10.8 | 9.3 |
| E4F1 | - | -44.0 (-35.3) | -28.1 | 38.7 | 32.7 |
| E5F1 | -85.5 | -40.0 | -34.8 | 5.3 | 5.1 |
| E6F1 | -79.9 | -43.0 (-47.7) | -24.4 (-29.3) | 72.1 | 66.7 |
| E3F2 | - | - | - | - | - |
| E4F2 | - | -47.0 | -36.0 | 10.9 | 9.7 |
| E5F2 | - | - | - | - | - |
| E6F2 | -83.8 | - | - | - | - |
| E3F1 1 M LiFSA | - | -30.3 | -4.7 (-14.6) | 7.0 | 7.8 |
| E4F1 1 M LiFSA | -84.4 | - | - | - | - |
| E5F1 1 M LiFSA | -81.0 | - | - | - | - |
| E6F1 1 M LiFSA | -77.5 | - | - | - | - |
| E4F2 1 M LiFSA | -83.3 | - | - | - | - |
| E5F2 1 M LiFSA | -82.1 | - | - | - | - |
| E6F2 1 M LiFSA | -78.9 | - | - | - | - |
| Diglyme | - | - | - | - | - |
| Triglyme | - | -59.6* | -41.5 | 115.4 | 127.7 |
| Tetraglyme | - | -34.9* | -25.9 | 97.5 | 105.1 |
| Diglyme 1 M LiFSA | - | - | - | - | - |
| Triglyme 1 M LiFSA | - | -72.8 (-63.7) | -48.1 | 70.0 | 69.8 |
| Tetraglyme 1 M LiFSA | - | -61.8* (-66.9) | -33.2 | 41.5 | 45.5 |
| EC/DMC 1 M $LiPF_6$ | - | -42.5* | -18.2 (-5.9) | 1.29 | 1.77 |

The transition points marked with "*" were observed in the cooling trace. For those samples having multiple crystallization/melting peaks, the temperature of second strongest peak was shown in bracket. The crystallization/melting enthalpy was calculated from the total area of corresponding peaks.

**Table S3**. Adiabatic redox energy data reproduced from reference paper

| **Compound name** | **Adiabatic oxidation energy (eV)** | | **Adiabatic reduction energy (eV)** | |
|---|---|---|---|---|
| | **Reproduced** | **Reference**[8] | **Reproduced** | **Reference**[8] |
| DMC | -8.23 | -8.51 | -1.42 | -1.42 |
| PC | -8.38 | -8.38 | -1.54 | -1.54 |
| THF | -6.93 | -6.94 | -0.17 | -0.17 |
| DMSO | -6.46 | -6.46 | -1.93 | -1.92 |
| Pyridine | -6.96 | -6.94 | -1.74 | -1.74 |

The data shown in this table were calculated rigorously following the procedure of the stated reference paper.[8] Most of the reproduced redox energy values matched well with reference. However, a significant difference was observed in the adiabatic oxidation energy of DMC, which may be due to different initial structure selection.

## References

(1) Saito, M.; Yamada, S.; Ishikawa, T.; Otsuka, H.; Ito, K.; Kubo, Y. Factors Influencing Fast Ion Transport in Glyme-Based Electrolytes for Rechargeable Lithium–Air Batteries. *RSC Adv.* **2017**, *7* (77), 49031–49040. https://doi.org/10.1039/C7RA07501D.

(2) Amanchukwu, C. V; Yu, Z.; Kong, X.; Qin, J.; Cui, Y.; Bao, Z. A New Class of Ionically Conducting Fluorinated Ether Electrolytes with High Electrochemical Stability. *J. Am. Chem. Soc.* **2020**, *142* (16), 7393–7403. https://doi.org/10.1021/jacs.9b11056.

(3) Yu, Z.; Wang, H.; Kong, X.; Huang, W.; Tsao, Y.; Mackanic, D. G.; Wang, K.; Wang, X.; Huang, W.; Choudhury, S.; Zheng, Y.; Amanchukwu, C. V; Hung, S. T.; Ma, Y.; Lomeli, E. G.; Qin, J.; Cui, Y.; Bao, Z. Molecular Design for Electrolyte Solvents Enabling Energy-Dense and Long-Cycling Lithium Metal Batteries. *Nat. Energy* **2020**, *5*, 526–533. https://doi.org/10.1038/s41560-020-0634-5.

(4) Günther, H. Lithium NMR. In *eMagRes*; 2007. https://doi.org/https://doi.org/10.1002/9780470034590.emrstm0273.

(5) Li, C.; Suzuki, K.; Yamaguchi, K.; Mizuno, N. Phosphovanadomolybdic Acid Catalyzed Direct C–H Trifluoromethylation of (Hetero)Arenes Using NaSO2CF3 as the CF3 Source and O2 as the Terminal Oxidant. *New J. Chem.* **2017**, *41* (4), 1417–1420. https://doi.org/10.1039/C6NJ03654F.

(6) Adams, B. D.; Zheng, J.; Ren, X.; Xu, W.; Zhang, J.-G. Accurate Determination of Coulombic Efficiency for Lithium Metal Anodes and Lithium Metal Batteries. *Adv. Energy Mater.* **2018**, *8* (7), 1702097. https://doi.org/https://doi.org/10.1002/aenm.201702097.

(7) Homann, G.; Stolz, L.; Nair, J.; Laskovic, I. C.; Winter, M.; Kasnatscheew, J. Poly(Ethylene Oxide)-Based Electrolyte for Solid-State-Lithium-Batteries with High Voltage Positive Electrodes: Evaluating the Role of Electrolyte Oxidation in Rapid Cell Failure. *Sci. Rep.* **2020**, *10* (1), 4390. https://doi.org/10.1038/s41598-020-61373-9.

(8) Feng, S.; Chen, M.; Giordano, L.; Huang, M.; Zhang, W.; Amanchukwu, C. V; Anandakathir, R.; Shao-Horn, Y.; Johnson, J. A. Mapping a Stable Solvent Structure Landscape for Aprotic Li–Air Battery Organic Electrolytes. *J. Mater. Chem. A* **2017**, *5* (45), 23987–23998. https://doi.org/10.1039/C7TA08321A.